

MATHEMATICAL MODELING AND SIMULATION OF  
MICROFLUIDIC FLOW IN GAS SENSORS

A THESIS SUBMITTED TO  
THE GRADUATE SCHOOL OF NATURAL AND APPLIED SCIENCES  
OF  
MIDDLE EAST TECHNICAL UNIVERSITY

BY

HALE YURTTUTAN

IN PARTIAL FULFILLMENT OF THE REQUIREMENTS  
FOR  
THE DEGREE OF MASTER OF SCIENCE  
IN  
CHEMICAL ENGINEERING

JULY 2023



Approval of the thesis:

**MATHEMATICAL MODELING AND SIMULATION OF  
MICROFLUIDIC FLOW IN GAS SENSORS**

submitted by **HALE YURTTUTAN** in partial fulfillment of the requirements for  
the degree of **Master of Science in Chemical Engineering, Middle East Technical  
University** by,

Prof. Dr. Halil Kalıpçılar  
Dean, Graduate School of **Natural and Applied Sciences** \_\_\_\_\_

Prof. Dr. Pınar Çalık  
Head of Department, **Chemical Engineering, METU** \_\_\_\_\_

Prof. Dr. Yusuf Uludağ  
Supervisor, **Chemical Engineering, METU** \_\_\_\_\_

Prof. Dr. Gürkan Karakaş  
Co-Supervisor, **Chemical Engineering, METU** \_\_\_\_\_

**Examining Committee Members:**

Prof. Dr. Naime Aslı Sezgi  
Chemical Engineering, METU \_\_\_\_\_

Prof. Dr. Yusuf Uludağ  
Chemical Engineering, METU \_\_\_\_\_

Prof. Dr. Gürkan Karakaş  
Chemical Engineering, METU \_\_\_\_\_

Prof. Dr. Niyazi Alper Tapan  
Chemical Engineering, Gazi Uni. \_\_\_\_\_

Asst. Prof. Dr. Gökhan Çelik  
Chemical Engineering, METU \_\_\_\_\_

Date: 05.07.2023

**I hereby declare that all information in this document has been obtained and presented in accordance with academic rules and ethical conduct. I also declare that, as required by these rules and conduct, I have fully cited and referenced all material and results that are not original to this work.**

Name Last name : Hale Yurttutan

Signature :

## ABSTRACT

### MATHEMATICAL MODELING AND SIMULATION OF MICROFLUIDIC FLOW IN GAS SENSORS

Yurttutan, Hale  
Master of Science, Chemical Engineering  
Supervisor : Prof. Dr. Yusuf Uludağ  
Co-Supervisor: Prof. Dr. Gürkan Karakaş

July 2023, 106 pages

Semiconductor metal oxide gas sensors are found extensive use in both industrial settings and household settings that enable the detection and quantification of various gases serving different purposes such as safety and process control. Carbon monoxide (CO) detection is vital because of its potential toxic effects on human health. This study provides a comprehensive investigation into the sensing behavior of a SnO<sub>2</sub>-based porous metal oxide gas sensor in response to CO by utilizing COMSOL Multiphysics.

In this study, CO gas in an excess oxygen environment is introduced with an inlet velocity to a measurement chamber, and the time-dependent response of the sensor is investigated. The model encompasses convective and diffusive mass transfer, reaction kinetics, conductance, and electrical current models. The dynamic ionized oxygen density is established as a connection between the gas concentration and the conductance of the sensor. The sensor's response is investigated for varying carbon monoxide concentrations, inlet velocities, temperatures, thicknesses, and porosities.

The findings indicate that the competing effect of reaction and diffusion mainly determines the overall distribution inside the sensing film. Additionally, the

longitudinal distribution of CO concentration highlighting the impact of CO molecules carried along the air flow was supported by the investigation of the local Sherwood number. The effect of CO inlet concentration on the sensor's conductance and sensitivity demonstrated that an increase in CO inlet concentration leads to higher conductance and a progressive increase in sensitivity. However, the sensitivity eventually reaches a plateau due to the saturation of reactive sites. In addition, the effect of inlet velocity, and horizontal/vertical flow configurations on the conductance profile were investigated. The effect of temperature on conductance and sensitivity was examined based on the competing effect of consumption and recovery of the ionized oxygen density. Furthermore, the study reveals an inverse relationship between sensitivity and the thickness of the sensing film while demonstrating a direct proportionality between sensitivity and porosity.

Keywords: Semiconductor Metal Oxide, Microfluidic Flow, CO Detection, Gas Sensor Modeling, Computational Modeling

## ÖZ

### GAZ SENSÖRLERİNDE MİKROAKIŞIN MATEMATİKSEL MODELLENMESİ VE SİMÜLASYONU

Yurttutan, Hale  
Yüksek Lisans, Kimya Mühendisliği  
Tez Yöneticisi: Prof. Dr. Yusuf Uludağ  
Ortak Tez Yöneticisi: Prof. Dr. Gürkan Karakaş

Temmuz 2023, 106 sayfa

Yarı iletken metaloksit gaz sensörleri, çeşitli gazların tespiti ve nicelendirilmesini sağlayarak hem endüstriyel ortamlarda hem de ev içi uygulamalarda geniş bir kullanım bulmuştur. Karbonmonoksit (CO) tespiti, insan sağlığı üzerindeki potansiyel toksik etkileri nedeniyle hayati önem taşır. Bu çalışma, COMSOL Multiphysics kullanarak CO'ya karşı SnO<sub>2</sub> tabanlı gözenekli bir metal oksit gaz sensörünün algılama davranışına kapsamlı bir inceleme sunmaktadır.

Bu çalışmada, aşırı oksijen ortamındaki CO gazı, bir ölçüm odasına giriş hızı ile sunulmuştur ve sensörün zamana bağlı yanıtı incelenmiştir. Model, taşınım ve difüzyonel kütle transferini, reaksiyon kinetiğini, iletkenliği ve elektrik akımı modellerini kapsar. Dinamik iyonize oksijen yoğunluğu, gaz konsantrasyonu ve sensörün iletkenliği arasındaki bağlantı olarak kurulmuştur. Sensörün yanıtı, değişken karbonmonoksit konsantrasyonları, giriş hızları, sıcaklıklar, sensör kalınlıkları ve gözeneklilikleri için incelenmiştir.

Bulgular, reaksiyon ve difüzyonun rekabet eden etkisinin, sensör filminin içindeki genel dağılımı büyük ölçüde belirlediğini göstermektedir. Ayrıca, hava akışı boyunca taşınan CO moleküllerinin etkisini vurgulayan CO konsantrasyonunun uzunlamasına dağılımı, yerel Sherwood sayısının incelenmesi ile desteklenmiştir. CO giriş konsantrasyonunun sensörün iletkenliği ve hassasiyeti üzerindeki etkisi, CO giriş konsantrasyonundaki bir artışın daha yüksek iletkenliğe ve hassasiyette kademeli bir artışa yol açtığını göstermiştir. Ancak, hassasiyet nihayetinde reaktif sitelerin doygunluğu nedeniyle bir platoya ulaşır. Ek olarak, giriş hızının ve yatay/dikey akış konfigürasyonlarının iletkenlik profil üzerindeki etkisi incelenmiştir. Sıcaklığın iletkenlik ve hassasiyet üzerindeki etkisi, tüketim ve iyonize oksijen yoğunluğunun geri kazanımı arasındaki rekabet etkisi temelinde incelenmiştir. Ayrıca, çalışma hassasiyet ile sensör filmi kalınlığı arasındaki ters ilişkiyi ve hassasiyet ile gözeneklilik arasındaki doğrudan orantıyı gösterir.

Anahtar Kelimeler: Yarı İletken Metal Oksit, Mikroakışkan akışı, CO Tespiti, Gaz Sensörü Modellemesi, Hesaplamalı Modelleme

To my beloved family

## ACKNOWLEDGMENTS

Foremost, I am deeply grateful to my advisor Prof. Dr. Yusuf Uludağ for his endless contributions, guidance, suggestions, and support throughout this study. He always encouraged and helped me with his expertise.

I would also like to express my sincere gratitude to my co-advisor Prof. Dr. Gürkan Karakaş for his valuable guidance and support. His valuable perspective and insight into my research were precious.

I also want to thank my family for their endless love and encouragement.

Special thanks to my husband, Uygur Ateş Ceylan, for his patience and love. His encouragement has been my source of strength.

Finally, I am grateful to all those who have directly or indirectly contributed to the successful completion of this thesis.

## TABLE OF CONTENTS

ABSTRACT.....	v
ÖZ .....	vii
ACKNOWLEDGMENTS .....	x
TABLE OF CONTENTS.....	xi
LIST OF TABLES .....	xiii
LIST OF FIGURES .....	xiv
LIST OF ABBREVIATIONS .....	xvii
LIST OF SYMBOLS .....	xviii
CHAPTERS	
1 INTRODUCTION .....	1
2 LITERATURE REVIEW .....	9
3 MODEL DESCRIPTION .....	23
3.1 The Transport of the Target Gas and Reaction Kinetics.....	26
3.1.1 Laminar Flow Interface.....	26
3.1.2 Porous Media Transfer.....	28
3.1.3 Reaction Kinetics .....	31
3.2 Conductance and Electrical Current Model .....	34
3.3 COMSOL Multiphysics .....	38
3.3.1 Time Discretization.....	39
3.3.2 Model Parameters .....	40
3.3.3 Mesh Independency .....	42
4 RESULTS AND DISCUSSION .....	45
4.1 Transient Analysis of CO Detection .....	46

4.1.1	CO Concentration Spatial Distribution Timewise Comparison .....	46
4.1.2	Ionized Oxygen Spatial Distribution Timewise Comparison.....	50
4.1.3	Surface Averaged Conductance Timewise Profile.....	52
4.2	Effect of Inlet Concentration .....	53
4.3	Effect of Inlet Velocity .....	57
4.3.1	Comparison of Horizontal and Vertical Flow Configurations .....	66
4.4	Effect of Temperature .....	70
4.5	Effect of Thickness .....	82
4.6	Effect of Porosity .....	87
5	CONCLUSION .....	91
	REFERENCES .....	95
	APPENDICES .....	105
A.	Initial Ionized Oxygen Density Calculation .....	105
B.	Temperature Change Calculation .....	105
C.	Initial Surface Potential Barrier Calculation.....	106

## LIST OF TABLES

### TABLES

Table 1-1. Comparison of types of gas sensors based on sensor parameters <sup>2</sup> .....	1
Table 1-2. Different metal oxides and corresponding gases for detection <sup>13</sup> .....	4
Table 3-1. Initial and boundary conditions of the model.....	30
Table 3-2. Model parameters and units.....	41
Table 4-1. The gas mixture velocity and corresponding Reynolds number .....	58
Table 4-2. Fluid velocities condition and corresponding Peclet number.....	61
Table 4-3. Fluid inlet velocities and corresponding response/recovery time .....	64
Table 4-4. Initial values of ionized oxygen density and initial conductance .....	71
Table 4-5. Different operating temperatures and corresponding initial, steady-state, and normalized conductance values.....	77
Table 4-6. Different temperatures and corresponding response/recovery times ....	81
Table 4-7. Porosity of the sensing film and corresponding sensor sensitivity.....	90

## LIST OF FIGURES

### FIGURES

Figure 1-1. Semiconductor metal oxide gas sensor structure <sup>17</sup> .....	6
Figure 1-2. Schematic of a typical experimental setup of metal oxide gas sensors <sup>21</sup> 7	
Figure 2-1. Stability of oxygen ions on metal oxide surface at different temperature ranges <sup>24</sup> .....	10
Figure 2-2. Band bending between the grains for n-type metal oxide a) O <sup>a-</sup> adsorbs on the grain surface results in depletion region and band bending b) CO oxidation reaction decreases band bending and thinning of the surface carrier space <sup>33</sup> .....	11
Figure 2-3. a)Langmuir–Hinshelwood mechanism, b)Eley–Rideal mechanism, c)Mars-Van Krevelen mechanism <sup>37</sup> .....	13
Figure 2-4. Schematic of sputtering deposition technique <sup>58</sup> .....	18
Figure 2-5. Schematic of drop coating deposition technique <sup>61</sup> .....	19
Figure 2-6. Target gas mass transfer along a microfluidic channel <sup>21</sup> .....	21
Figure 3-1. Geometry of the measurement chamber and the sensor for the model.	24
Figure 3-2. Band energy and depletion layer between the grains <sup>84</sup> .....	35
Figure 3-3. Electrical current inside the sensing film.....	37
Figure 3-4. Relationship between steady-state conductance and the number of elements in different meshes .....	42
Figure 3-5. Conductance spatial distribution for varying meshes .....	43
Figure 3-6. Extra fine mesh structure .....	43
Figure 4-1. CO concentration profile at the vertical line placed in the center of the 100 μm sensing film at 600 K exposed to 200 ppm of CO, with an inlet velocity of 0.01 m/s .....	47
Figure 4-2. CO concentration profile at the horizontal line placed in the center of the 100 μm sensing film at 600 K exposed to 200 ppm of CO, with an inlet velocity of 0.01 m/s .....	48
Figure 4-3. Local Sherwood number along the sensor surface at t=0.2sec .....	49

Figure 4-4. Ionized oxygen density profile at the vertical line placed in the center of the 100 $\mu\text{m}$ sensing film at 600 K exposed to 200 ppm of CO, with an inlet velocity of 0.01 m/s.....	50
Figure 4-5. Electrical current flux profile at the vertical line placed in the center of the 100 $\mu\text{m}$ sensing film at 600 K exposed to 200 ppm of CO, with an inlet velocity of 0.01 m/s.....	51
Figure 4-6. Surface averaged conductance timewise profile of the 100 $\mu\text{m}$ sensing film at 600 K exposed to 200 ppm of CO, with an inlet velocity of 0.01 m/s.....	52
Figure 4-7. Surface averaged conductance change over time in response to different CO inlet concentrations at 600 K, with an inlet velocity of 0.01 m/s.....	55
Figure 4-8. Steady-state surface potential barrier in response to different CO inlet concentrations at 600 K, with an inlet velocity of 0.01 m/s .....	56
Figure 4-9. Sensor sensitivity in response to different CO inlet concentrations at 600 K, with an inlet velocity of 0.01 m/s.....	57
Figure 4-10. Flow velocity change along the center longitudinal axis of the measurement chamber.....	59
Figure 4-11. Surface averaged conductance profile in response to different inlet flow velocities for 100 $\mu\text{m}$ thickness sensing film at 600K a)whole profile b)zoomed profile to early time points .....	60
Figure 4-12. Response/recovery timewise profile for varying inlet velocities in response to 200 ppm of CO at 600 K a) 0.005 m/s b) 0.01 m/s c) 0.03 m/s d) 0.05 m/s e) 0.1 m/s.....	63
Figure 4-13. Two different flow configurations to the measurement chamber a, b, c) Horizontal flow from the left d, e, f) Vertical flow from the top.....	67
Figure 4-14. Surface averaged conductance timewise profile for horizontal and vertical flow configurations in response to 200 ppm of CO at 600 K, with an inlet velocity of 0.01 m/s.....	68
Figure 4-15. Steady-state CO concentration spatial profile for varying operating temperatures in response to 200 ppm of CO, with an inlet velocity of 0.01 m/s....	72

Figure 4-16. Absolute surface averaged conductance profile for varying temperatures in response to 200 ppm of CO, with an inlet velocity of 0.01 m/s a)whole profile b)zoomed profile to early time points .....	74
Figure 4-17. Sensor sensitivity for different operating temperatures in response to 200 ppm of CO, with an inlet velocity of 0.01 m/s .....	76
Figure 4-18. Difference between reaction rate and recovery rate of ionized oxygen density for different operating temperatures .....	78
Figure 4-19. Response/recovery profiles for different operating temperatures in response to 200 ppm of CO, with an inlet velocity of 0.01 m/s .....	80
Figure 4-20. Surface averaged CO and ionized oxygen density response/recovery profiles in response to 200 ppm of CO at 500 K, with an inlet velocity of 0.01 m/s .....	81
Figure 4-21. Steady-state CO concentration spatial profiles for varying thicknesses in response to 200 ppm of CO at 600 K, an inlet velocity of 0.01 m/s a)50 $\mu\text{m}$ b)75 $\mu\text{m}$ c)100 $\mu\text{m}$ d)125 $\mu\text{m}$ e)150 $\mu\text{m}$ .....	83
Figure 4-22. Steady-state surface potential barrier spatial distribution for varying thicknesses in response to 200 ppm of CO at 600 K, with an inlet velocity of 0.01 m/s .....	84
Figure 4-23. Surface averaged conductance timewise profile for varying thicknesses in response to 200 ppm of CO at 600 K, with an inlet velocity of 0.01 m/s .....	85
Figure 4-24. Sensor sensitivity with varying thicknesses in response to 200 ppm of CO at 600 K, with an inlet velocity of 0.01 m/s.....	86
Figure 4-25. Steady-state ionized oxygen density spatial distribution for different porosities of the sensing film in response to 200 ppm of CO at 600 K, with an inlet velocity of 0.01 m/s .....	88
Figure 4-26. Surface averaged conductance change over time for different porosities of the sensing film in response to 200 ppm of CO at 600 K, with an inlet velocity of 0.01 m/s .....	89

## LIST OF ABBREVIATIONS

### ABBREVIATIONS

DAE	Differential algebraic system of equations
ODE	Ordinary differential equation
PDE	Partial differential equation
ppm	Parts per million

## LIST OF SYMBOLS

### SYMBOLS

$E_1$	Activation energy of chemisorption reaction
$E_2$	Activation energy of ionization reaction
$E_3$	Activation energy of oxidation reaction
$E_{-1}$	Activation energy of reverse chemisorption reaction
$E_{-2}$	Activation energy of reverse ionization reaction
$A\nu$	Avogadro number
$k_B$	Boltzmann constant
$L$	Characteristic length
$c$	Concentration
$G_c$	Conductance constant
$Co$	Courant number
$A$	Cross-sectional area
$\rho$	Density
$Q$	Dissipated heat
$N_d$	Donor density
$\mu$	Dynamic viscosity
$D_{k,eff}$	Effective Knudsen diffusion coefficient
$q$	Electric charge
$\vec{j}$	Electrical current flux
$\vec{E}$	Electrical field vector
$n_s$	Electron concentration
$C_\infty$	Free stream concentration
$D_h$	Hydraulic diameter
$R$	Ideal gas constant
$N_S$	Ionized oxygen density

$\nu$	Kinematic viscosity
$Sh_x$	Local Sherwood number
$\mu_s$	Mobility of electrons
$M$	Molecular weight
$d_p$	Particle diameter
$Pe$	Peclet number
$K$	Permeability
$\epsilon_0$	Permittivity in vacuum
$\epsilon$	Porosity
$G_0$	Pre-exponential conductance
$p$	Pressure
$k_{-1,0}$	Reaction rate constant of chemisorption reaction
$k_{2,0}$	Reaction rate constant of ionization reaction
$k_{3,0}$	Reaction rate constant of oxidation reaction
$k_{-1,0}$	Reaction rate constant of reverse chemisorption reaction
$k_{-2,0}$	Reaction rate constant of reverse ionization reaction
$R_{rxn}$	Reaction term in transport equation
$\epsilon_r$	Relative permittivity
$Sc$	Schmidt number
$\Delta x$	Spatial grid size
$a$	Specific surface area
$N_O^0$	Steady-state adsorbed neutral oxygen density
$\Delta t$	Time step size
$\tau$	Tortuosity
$\phi$	Total mass flux
$u$	Velocity
$V$	Voltage
$w$	Width of the sensor



# CHAPTER 1

## INTRODUCTION

Gas sensors have a wide range of applications in industry and household settings. There are various types of gas sensors based on different detection principles, such as metal oxide gas sensors, thermal conductive gas sensors, optical gas sensors, catalytic gas sensors, and electrochemical gas sensors, as seen in Table 1-1.

Semiconductor gas sensors, also known as chemo resistive gas sensors, have considerable attention and widespread use because of their superior parameters such as sensitivity, response time, and low fabrication costs compared to other gas sensors<sup>1</sup>.

Table 1-1. Comparison of types of gas sensors based on sensor parameters<sup>2</sup>

Parameters	Types of Gas Sensors				
	MOS	Optical Absorption	Catalytic	Thermo conductive	Electrochemical
Response/Sensitivity	E	E	G	P	G
Stability	G	E	F	G	P
Selectivity	F	E	P	P	G
Response time	E	G	G	G	F
Accuracy	G	E	G	G	G
Durability	G	E	G	G	P
Maintenance	E	F	E	G	G
Cost	E	F	E	G	G

E-excellent, G-Good, F-Fair, P-Poor

While semiconductor metal oxide gas sensors offer detection of a wide range of target gas and can stay in operation for long times, other gas sensors have some inferior parameters. Optical absorption gas sensors are commonly used in industry; however, having a high cost of production makes them impractical for extensive usage. On the other side, catalytic gas sensors have poor selectivity and safety issues such as explosion and poisoning because of catalysts. Thermoconductive gas sensors have poor selectivity and sensitivity problems. These sensors measure the target gas concentration based on differences in the thermal conductivities of different gases. However, some gases have similar thermal conductivities, such as methane and carbon monoxide (CO), which may lead to selectivity problems when both gases are present in the same environment. On the other side, electrochemical gas sensors have short operation life, which increases the cost. In addition, these sensors are not stable because of the significant impact of temperature and humidity changes in the environment<sup>3,4</sup>.

Semiconductors first started to use as gas sensors almost 70 years ago when an electron-depletion layer was found at the surface of the semiconducting materials<sup>5</sup>. The first demonstration showed that the resistance of semiconductor materials changed based on the environment where they came into contact with the target gas<sup>1</sup>. In the early years of the 1970s, the first semiconductor metal oxide gas sensor based on SnO<sub>2</sub> was produced because of its stable thermal structure, simplicity, small size, and high sensitivity. Semiconductor metal oxide gas sensor commercial production was mainly made by Figaro Inc. These sensors are used to detect the presence of dangerous levels of explosive gases and prevent accidents or fires in household settings. After observations of the better response of the detection systems of chemo resistive devices compared to other detectors, research for performance parameters of semiconductor metal oxide sensors has been intensified, and their applications increased in various fields such as environmental monitoring, automotive, agricultural, biomedical, etc<sup>1</sup>. Some notable applications are filter controls and gasoline vapor detection in the automotive industry, fire detection and leak detection of toxic or flammable gases in household settings, breath analysis, and disease

detection in biomedical, weather forecast and pollution monitoring in environmental control, and mainly process control in industrial applications<sup>6</sup>. Semiconductor metal oxide gas sensors are sensitive because of their porous structure resulting in a high surface area for interaction of the target gas with the sensor surface<sup>7</sup>. In order to increase the reaction surface area, porous structure is synthesized chemically using different techniques. In this way, target gas diffusion is enhanced, resulting in higher sensitivity and response/recovery times<sup>8</sup>. Furthermore, their operation principle based on fast surface reactions leads to lower response times. However, semiconductor metal oxide sensors can be unreliable at high humidity and varying temperatures<sup>9</sup>.

The sensing mechanism of semiconductor metal oxide gas sensors is based on detecting the change in the electrical conductivity of the sensor. In the presence of ambient oxygen that is adsorbed on the sensor surface, an electron-depleted layer is formed in the sensor. This ionized oxygen creates an acceptor level which bends the energy band upward. When the reducing target gas is reached to the n-type semiconductor sensor surface, which is the case in this study, the target gas responds to the highly sensitive metal oxide surface. It reacts with the ionized oxygen molecule, and captured electrons are released to the sensing material. The released electrons lower the resistance by decreasing the depletion region barrier height at the interface, and band bending is released<sup>10</sup>. Under an applied bias voltage across the sensing film, an electrical current is driven with the decrease of the resistance. Consequently, the conductivity of the material has increased, and electrons can easily move through the sensing film, resulting in a higher current.

This study particularly focuses on carbon monoxide detection, which is critically important for several reasons. Carbon monoxide is produced in several ways, such as incomplete combustion of hydrocarbons in various settings such as car exhaust and heating systems, industrial processes, garbage disposal, and tobacco smoke<sup>11</sup>. Carbon monoxide is a highly toxic gas for humans and animals because it interferes with the delivery of oxygen molecules to the cells by binding hemoglobin more easily than oxygen molecules. This higher affinity of CO for hemoglobin causes

saturation with CO and reduces oxygen-carrying capacity in the blood cells<sup>12</sup>. CO detection is crucial to ensure safety in various settings because even low concentrations result in serious health problems. However, CO is a colorless and odorless gas that needs to be detected by specialized gas sensors.

Table 1-2. Different metal oxides and corresponding gases for detection <sup>13</sup>

Metal oxide Material	Gases Optimal for Detection
SnO <sub>2</sub>	H <sub>2</sub> , CO, CH <sub>4</sub> , O <sub>2</sub> , NH <sub>3</sub> , NO, NO <sub>2</sub> , C <sub>2</sub> H <sub>6</sub> O, C <sub>n</sub> H <sub>2n</sub>
ZnO	H <sub>2</sub> , CO, O <sub>2</sub> , NH <sub>3</sub> , NO, NO <sub>2</sub> , C <sub>2</sub> H <sub>6</sub> O, C <sub>n</sub> H <sub>2n</sub>
Fe <sub>2</sub> O <sub>3</sub>	H <sub>2</sub> , CO, CH <sub>4</sub> , NO <sub>2</sub> , C <sub>2</sub> H <sub>6</sub> O, C <sub>n</sub> H <sub>2n</sub>
TiO <sub>2</sub>	H <sub>2</sub> , CO, CO <sub>2</sub> , NH <sub>3</sub> , O <sub>2</sub> , SO <sub>2</sub>
CrO <sub>3</sub>	NO, NO <sub>2</sub> , CO
CuO	H <sub>2</sub> , CO, O <sub>2</sub> , C <sub>2</sub> H <sub>6</sub> O
V <sub>2</sub> O <sub>5</sub> and Nb <sub>2</sub> O <sub>5</sub>	CO, CO <sub>2</sub> , NO, NO <sub>2</sub> ,

Semiconductor gas sensors are mainly based on metal oxides, including both the n-type such as SnO<sub>2</sub>, ZnO, TiO<sub>2</sub>, Fe<sub>2</sub>O<sub>3</sub>, and WO<sub>3</sub>, and the p-type such as NiO, CuO, Cr<sub>2</sub>O<sub>3</sub>, etc. which have different physical and chemical properties<sup>1,14</sup>. Generally, p-type metal oxide gas sensors operate under low temperatures. However, most of the metal oxide gas sensors are utilized in n-type because of natural electron release by oxygen molecules. In Table 1-2, different metal oxide materials and corresponding gases for optimal detection can be seen. The table points out that CO can be detected by utilizing various metal oxide materials. At this point, it is essential to investigate the promising properties of tin dioxide (SnO<sub>2</sub>) over other metal oxide materials for CO detection. SnO<sub>2</sub> has a high surface-to-volume ratio which leads to more active

site and high sensitivity toward various gases and concentrations<sup>15</sup>. This is critical for gas sensors to accurately detect toxic target gases, both in low-concentration environments and at high-concentration environments, where the sensor may reach its saturation point. In addition, sensitivity toward reducing gases and high-temperature stability during operation make SnO<sub>2</sub> a preferred choice for CO detection. SnO<sub>2</sub> has a wide band gap (3.6 eV) compared to other metal oxides, which means more energy is needed to excite electrons<sup>16</sup>. This results in operating at high temperatures without suffering thermal degradation. On the other hand, poor selectivity or cross-sensitivity is an issue for SnO<sub>2</sub>-based sensors where the target gas cannot be detected accurately in an interfering gas environment. Various strategies are developed to improve the selectivity performance, such as the addition of dopants to eliminate the effect of interfering gases, using filters or chromatographic columns to differentiate gases based on their physical properties, and adjusting the operating temperature to maximize sensitivity toward the target gas<sup>1,6</sup>.

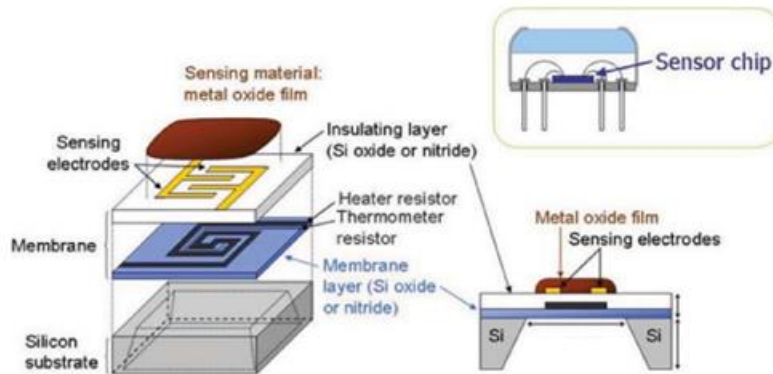


Figure 1-1. Semiconductor metal oxide gas sensor structure<sup>17</sup>

A typical semiconductor metal oxide gas sensor construction mainly contains a substrate, a heater element, an insulating layer, sensing electrodes, and a sensing layer, as seen in Figure 1-1. The heater element supports and helps the sensing layer reach and operates under a specific temperature. In addition, the heater element provides a uniform temperature for the sensing layer. The sensing electrodes (usually Pt or Au because of their high specific capacity and high electrical conductivity<sup>18</sup>) which are deposited on the active film, are responsible for the conductance measurement of the sensing material<sup>19</sup>. The sensor substrate provides a stable and inert surface to protect the sensing layer from environmental factors. In addition, the substrate part supports the heater element, and it can withstand elevated operating temperatures. Silicon is generally used as the substrate layer because of its high stability at high temperatures and robust mechanical properties<sup>20</sup>.

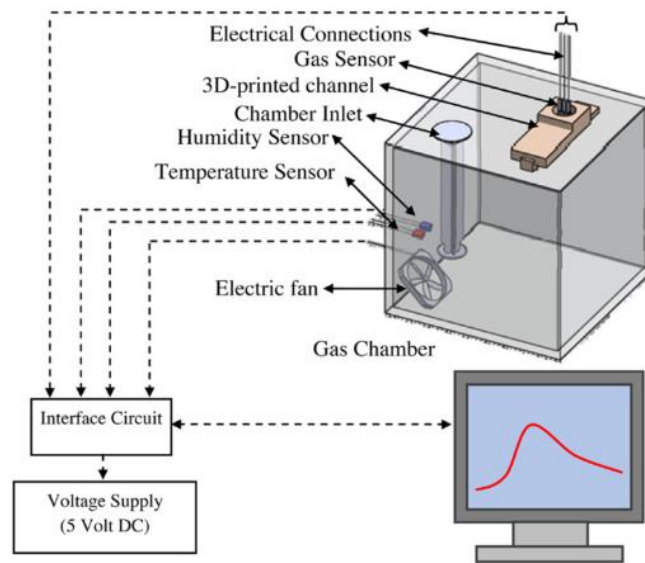


Figure 1-2. Schematic of a typical experimental setup of metal oxide gas sensors<sup>21</sup>

Figure 1-2 represents a schematic of a typical experimental setup of a semiconductor metal oxide gas sensor. The process begins with gas molecules from the chamber inlet moving through the gas chamber. Subsequently, it diffuses through the whole chamber. The electrical fan or flow controller is utilized to enhance the mass transfer of the target gas molecules within the chamber. Once the target gas molecules reach the sensing film target gas reaction takes place. In order to capture this reaction, a DC voltage is applied to both sides of the film. This setup enables the measurement of changes in electrical conductivity. Following the detection process, the sensing film should be recovered. In order to recover the sensing film and target gas-filled chamber from the target gas molecules, the chamber inlet is connected to fresh air.

However, incorporating a fully functional setup is a time-consuming process. An accurate model of such a setup, with the proper simplifications, could predict the sensor behavior in a dramatically reduced amount of time. To do so, the current study uses COMSOL Multiphysics which provides a platform to combine typical physics such as laminar flow, transport of species, and electrical current. In addition, it facilitates the capability of introducing user-defined equations. This capability is

crucial in the context of sensor response modeling because of the need for an accurate representation of the reactions inside the sensor. In the proceeding chapters, the results obtained from this numerical model are discussed. The primary purpose is to establish a fundamental approach to modeling the conjugate mass transfer associated with the experimental setups similar to the one shown in Figure 1-2.

## CHAPTER 2

### LITERATURE REVIEW

Semiconductor metal oxide gas sensors are extensively used based on reversible changes in electrical conductivity in response to various target gases. The gas sensing mechanism can be explained by microscopic and macroscopic mechanisms. Microscopic mechanisms focus mainly on Fermi-level control and charge carrier depletion layer theory, while macroscopic mechanisms focus mainly on gas transport and resistance mechanisms<sup>22</sup>.

The gas sensing mechanism is explained mainly by two fundamental functions called receptor and transducer. First, the target gas is perceived at the sensing surface, and electron change on the metal oxide surface takes place. This interaction between the target gas and the sensor surface, thus the change in surface oxygen equilibrium, is controlled by receptor function. Then, changes in the sensing surface are transformed into electrical conductivity changes and signals in the sensor with transducer function<sup>4</sup>.

Chemical adsorption and desorption explain the fundamental operating principle of metal oxide-based sensors. When the sensing surface comes in contact with the atmospheric air, oxygen molecules are adsorbed on the sensing surface because of their highly electronegative nature<sup>23</sup>. Then, adsorbed oxygen molecules start to capture electrons from the sensing material and form different charged forms of oxygen ions ( $O_2^-$ ,  $O^-$ , and  $O^{2-}$ ) depending on the operating temperature, as seen in Figure 2-1. Total surface electron density determines the resistance of the semiconductor metal oxide gas sensors.

Increase in Temperature and Increase in Electron Density			
25°C	150-200°C	400°C	500°C
$O_2$ (adsorption) $\rightarrow$ $O_2^-$ (adsorbed and charged) $\rightarrow$ $O^-$ (dissociative adsorption) $\rightarrow$ $O^{2-}$ [Dynamic Lattice]			
<b>Stable Chemisorbed Oxygen Species on the SMOs' Surfaces as Temperature Rises</b>			
Exothermic $\Delta H < 0$		Endothermic $\Delta H > 0$	

Figure 2-1. Stability of oxygen ions on metal oxide surface at different temperature ranges<sup>24</sup>

The stable forms of adsorbed oxygens are mainly described as neutral molecular oxygen that is physisorbed at room temperature and negatively charged chemisorbed oxygen ions ( $O_2^-$ ,  $O^-$ , and  $O^{2-}$ ) that are stable below 500°C. While the formation reaction of  $O_2^-$  ion is exothermic, other formations are endothermic<sup>24,25</sup>. The semiconductor metal oxide gas sensor's optimal operating temperature is typically between 500 to 800 Kelvin, in which  $O^-$  is the dominant surface oxygen species<sup>23</sup>.

As seen in Figure 2-2, semiconductor metal oxide gas sensors consist of linked adjacent grains<sup>17</sup>. The conductance model capturing the sensing mechanism of semiconductor metal oxide gas sensors explains the Schottky barrier formation when the grain size is large compared to the thickness of the space charge layer. This model covers the dependence of conductance on temperature and surface barrier that is a function of donor density and oxygen partial pressure<sup>26-29</sup>. The Fermi level concept forms the backbone of semiconductors explaining the flow of electrons through grain boundaries at high temperatures. It describes the energy state that has the highest probability of being occupied by an electron. Its position between the valence band and conduction band determines the semiconductor type. Semiconductors are mainly divided into two categories that are intrinsic and extrinsic. Intrinsic semiconductors are pure, and the Fermi energy level is positioned in the middle of the bandgap. For

an extrinsic semiconductor fermi level shifts toward valance or conduction band based on being n-type or p-type<sup>30</sup>. While n-type semiconductors such as SnO<sub>2</sub>, ZnO, and TiO<sub>2</sub> use electrons as the majority carrier, p-type metal oxides such as CuO, NiO, and Cr<sub>2</sub>O<sub>3</sub> have holes as the majority charge carrier. P-type semiconductors have fewer valance electrons than the intrinsic state leading to an acceptor state near the valance band. The acceptor level captures most of the electrons from the valance band, and electron transfer to the conduction band is limited<sup>31</sup>. Once the metal-oxide surface is exposed to air, oxygen from the air gets adsorbed on the metal oxide surface and captures electrons. This electron depletion leads higher hole accumulation layer in the valance band, which reduces the resistance inside the sensing film. If the target gas is a reducing gas, it increases the resistance in p-type semiconductors because of the electron-hole combination, which reduces the hole accumulation layer. On the other side, oxidizing target gases, due to their high electron affinity, capture electrons and lead increase in hole accumulation layer in p-type metal oxide sensors resulting in increased conductivity<sup>32</sup>.

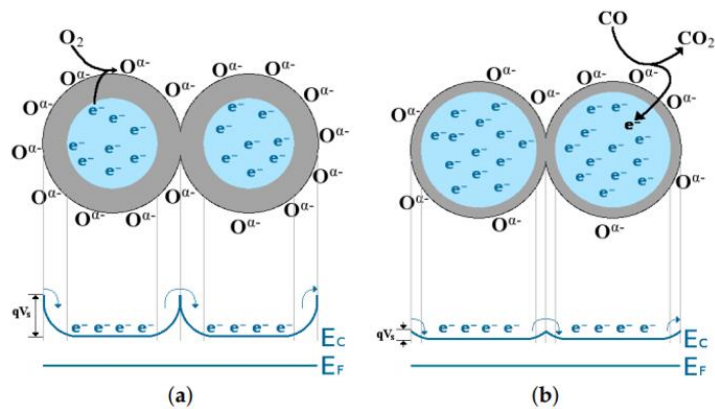
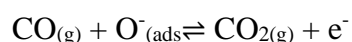


Figure 2-2. Band bending between the grains for n-type metal oxide  
a) O<sup>a-</sup> adsorbs on the grain surface results in depletion region and band bending  
b) CO oxidation reaction decreases band bending and thinning of the surface carrier space<sup>33</sup>

Figure 2-2 represents the n-type semiconductor depletion region and band bending mechanism. N-type semiconductors have more valance electrons than intrinsic ones, so the Fermi level shifts toward the conduction band. This shift toward the conduction band causes more electrons to be in the conduction band than the number of holes in the valance band. Once the metal oxide surface comes into contact with air, adsorbed oxygen molecules capture electrons in the conduction band and form ionized oxygen that leads to electron depletion layer formation called space charge layer and causes a Schottky potential barrier at the grain boundary ( $eV_{\text{surface}}$ ) which decreases the electron flow and increases the resistance. This potential barrier at the boundary is called conduction band bending. Based on the target gas, whether it is a donor or acceptor, conductivity changes. If the target gas is a reducing gas such as CO, electrons will be released to the conduction band, and conductivity will decrease. If the target gas is an acceptor molecule, electrons will be captured, and conductivity will decrease<sup>4</sup>. The charge transfer between the adsorbed gas molecules and semiconductor metal oxides, as well as the target gas surface interaction, determine the overall conductivity of a metal oxide semiconductor gas sensor<sup>34</sup>.

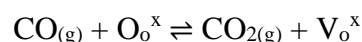
In order to explain conductivity changes in gas sensing, two different models, that are ionosorption and oxygen-vacancy models, are utilized. While the ionization model takes into account differences in electric surface potential as a result of gas ionosorption, the oxygen-vacancy model considers the changes in the oxygen stoichiometry, which corresponds to the differences in the number of surface oxygen vacancies and its reduction-reoxidation mechanisms as seen below<sup>19</sup>.

Ionosorption model:



where  $V_o^x$  is the neutral vacancy.

Oxygen-vacancy model:



The ionsorption model mainly considers that the sensing material forms charged sites to make an attractive surface for the target gas molecules. In the case of n-type semiconductor metal oxides, electrons are transferred from the conduction band to the oxygen molecules to form oxygen ions. When the reducing gas comes into contact with the ionized, based on different adsorption mechanisms such as Eley-Rideal or Langmuir Hinshelwood, oxygen electrons are returned to the conduction band affecting the electrical conductivity<sup>35</sup>. Langmuir-Hinshelwood mechanism explains the simultaneous adsorption of two molecules to the surface and bimolecular reaction of adsorbed molecules, as seen in Figure 2-3a. Conversely, in Eley-Rideal mechanism, one molecule is adsorbed to the surface, and the other molecules react with the pre-adsorbed molecule without adsorbing to the surface, as seen in Figure 2-3b<sup>36</sup>.

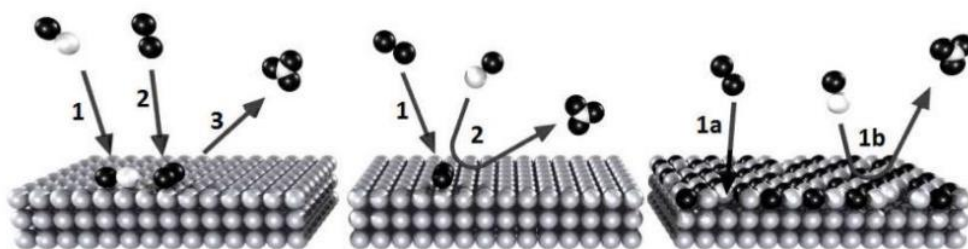


Figure 2-3. a)Langmuir–Hinshelwood mechanism, b)Eley–Rideal mechanism, c)Mars-Van Krevelen mechanism<sup>37</sup>

Alternatively, as seen in Figure 2-3c oxygen vacancy model considers oxygen vacancies at the metal oxide surface in which dynamic reduction and reoxidation take place. This model can be explained by Mars-Van Krevelen adsorption mechanism. When CO gas reaches the sensor surface, it reacts with oxygen to form carbon dioxide ( $\text{CO}_2$ ), resulting in oxygen vacancy. The oxygen vacancies continue to be ionized and release electrons to the conduction band simultaneously, which increases conductivity<sup>19</sup>.

The modeling of semiconductor metal oxide gas sensors has significant importance in describing the sensing mechanism and electrical response of metal oxide gas sensors in different operating conditions. The behavior of metal oxide porous sensing film to target gases has been approximated by different mathematical models that consider adsorption, desorption, mass transfer, and the reaction of the target gas simultaneously. In the literature, different numerical and experimental models explain the complex nature of gas sensing.

Many studies examine diffusion-reaction coupled models for metal oxide gas sensors. One of the preliminary models was developed by Gardner<sup>38</sup>, in which a linear model based on diffusion and reaction was studied to observe the electrical behavior of SnO<sub>2</sub> sensors numerically and experimentally. The model considered the diffusion-limited behavior of the porous thick sensing film to describe the steady state and transient response. In addition, Yamazoe et al.<sup>39</sup> investigated Knudsen diffusion and first-order reaction coupled numerical model to understand the sensor sensitivity of SnO<sub>2</sub>-based sensors. This study illustrated the competing effect of reaction and diffusion rates on sensor response and gas concentration profiles. The study also examined how the thickness of the sensor affects dominating factor for the overall response. This proposed model relates conductance with the target gas concentration linearly.

In the later studies, this linear relation between gas concentration and conductance is improved, and a nonlinear relation is proposed as a result of various numerical and experimental studies<sup>40-42</sup>. These studies investigated the fitted sensor response to power law equations. A nonlinear numerical model that couples the reaction with diffusion was developed by Lu et al.<sup>43</sup> by comparing theory and experiment in order to investigate the gas sensing behavior. This study provides the response time as a function of both thickness and gas concentration.

One of the prominent studies was conducted by Fort et al.<sup>44</sup>. This study provides a simplified and comprehensive surface state model that captures the mechanism in metal oxide gas sensing. This study proposed a grey box model which combines

system operation principles with data utilization to predict the behavior of SnO<sub>2</sub>-based sensors to CO gas molecules in an excess oxygen environment with different commercial metal oxide sensors. This study compared numerical and experimental results to determine the best model parameters. The proposed model contains a response model for oxygen and the reducing gas and conductance model based on the surface potential barrier between the grains of the metal oxide sensor. This study constitutes the main reference for this thesis because of its well-fitted parameters.

Due to the widespread use of semiconductor metal oxide gas sensors, having effective, reliable, and fast sensor response plays a crucial role. For this reason, research for improving sensor performance parameters has gained significant importance, and numerous studies have been conducted. The desired sensor characteristic for metal oxide gas sensors includes high sensitivity, which enables the detection of a wide range of gas concentrations, and high selectivity, allowing for the detection of the target gases. Additionally, short response and recovery times are desirable, enabling the sensor to quickly detect changes in gas levels and return to its initial state, particularly for safety-critical environments<sup>45,46</sup>.

Numerous studies investigate the effects of grain size, porous structure, and doping by metal or metal oxides on metal oxide gas sensor sensitivity. Yamazoe<sup>47</sup> conducted prior studies that the sensing characteristics can be improved by changing the transducer and receptor functions of the sensor. The study showed that the transducer function that explains the grain size and space charge layer plays a crucial role in improvements for the sensor response. In addition, the study revealed that the receptor function is modified by adding promoters to the SnO<sub>2</sub> surface to contribute electron deficient space charge layer and sensor sensitivity.

Grain size dependency on sensitivity has mainly three mechanisms based on comparative grain sizes and thickness of the space charge layer, also called Debye length<sup>48</sup>. If the grain size is large compared to the thickness of the space charge layer, conductance is controlled by the Schottky barrier, which makes sensitivity grain size independent and called grain boundary control. If the grain size is comparable with

the thickness of the space charge layer, sensor conductance is controlled by necks between grains. When the grain size is smaller than the space charge layer thickness, conductance is affected by every grain, so higher sensitivity can be achieved. This leads to significant changes in resistance in the presence of the target gas. This is because as grain size increases, grain boundary and specific surface area decreases<sup>23,49</sup>.

Zhang et al.<sup>27</sup> investigated the changes in SnO<sub>2</sub> sensor response with particle size and the addition of dopants experimentally. It is concluded that decreasing particle size results in higher sensitivity and fast response times. In addition, it is found that to form higher oxygen vacancies in the material, Sn ions are replaced by copper ions which leads to higher sensitivity. In the review of Chai et al.<sup>48</sup> the parameters that affect the stability of metal oxide gas sensors and the doping in semiconductor metal oxide gas sensors were explained. It is found that the doped element and content affect the overall stability of the sensing film. In some cases, doping may cause a decrease in porosity and specific surface area and limits the adsorption process so that sensor response decreases, which makes proper choice crucial. On the other side, Yamoze et al.<sup>50</sup> studied the grain size effect on SnO<sub>2</sub> thin films while the thickness was unchanged. The results showed that increasing grain size improves the sensor sensitivity to H<sub>2</sub>. This result conflicts with the literature findings that explain grain size sensitivity relation. This is because the particle size determines the average pore size of the sensor, which means a larger grain size leads to larger pores. Therefore, gas diffusion in the porous medium is enhanced, which results in higher sensitivity.

In addition to the porosity and grain size of the metal oxide gas sensors, the thickness of the sensing material plays an important role in the sensor performance parameters. The thickness effect on sensitivity has been investigated in several studies<sup>51-54</sup>. These experimental studies pointed out that the thickness significantly impacts sensor sensitivity, optimal operating temperature, and response time. In these studies, the effect of thickness has been explained by a simple reaction-diffusion model, and it has concluded that different kinetic barriers inside the metal oxide films determine the response. The procedure employed for the deposition of the sensing layer

significantly influences the performance of the sensor, as its operational conditions have a direct impact on the sensor layer's surface structure and thickness. Moreover, power usage and temperature consistency are influenced by the thickness of the sensor, which indirectly affects the sensitivity, selectivity, and response time of the sensor<sup>55,56</sup>. This thickness also has the potential to modulate the reactions and diffusion interactions within the sensing layer, which can consequently modify the final response<sup>57</sup>. However, maintaining precise control over the deposition parameters may not always be feasible, which could lead to unintentional morphological deviations from the desired target. The reasons behind these morphological deviations can be explained by investigating two commonly used thin film deposition techniques, such as sputtering and drop coating.

Sputtering is a technique that utilizes the fundamental process of DC glow discharge. The method involves creating plasma inside a vacuum environment, typically with an inert gas like argon as shown in Figure 2-4. Utilizing an inert gas minimizes the possibility of chemical reactions with the substrate or the target material. The essence of sputtering lies in applying a high-voltage bias to the target, which is positioned at the cathode. Positive gas ions are sped up in the vacuum tube, colliding with the target forcefully enough to remove one or more atoms from the target's surface. This action also releases secondary electrons. The removed neutral atoms travel across the chamber, eventually settling on the substrate or wafer. To ensure a dense deposition and clear off any detached atoms, the bias on the substrate is usually set to a negative value, significantly lower than the cathode voltage<sup>58</sup>.

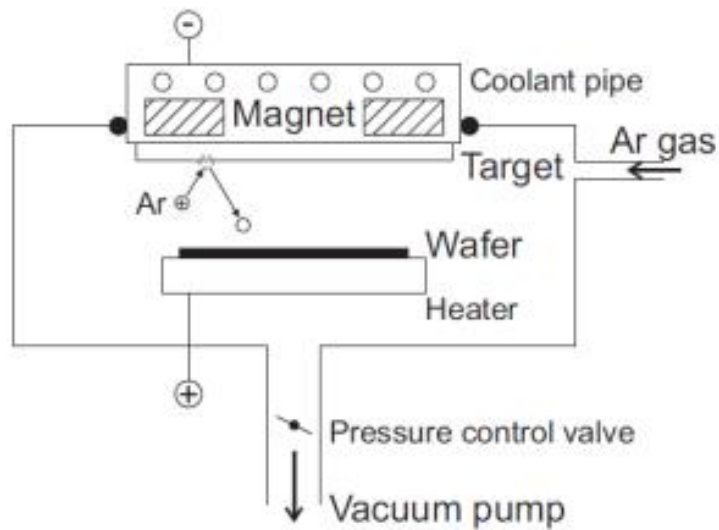


Figure 2-4. Schematic of sputtering deposition technique<sup>58</sup>

Another thin film deposition technique is drop coating which is simpler than sputtering. Drop coating is an efficient and straightforward deposition method that minimizes the use of solvent and reduces material waste. This technique does not need complex and expensive equipment. Instead, it needs a droplet generator, as shown in Figure 2-5. This technique involves depositing a solution or suspension onto a base material in droplet form. The structure and performance of the resulting film can be significantly impacted by the composition of the paste and the specific characteristics of the drop deposition process. The main drawback of this technique is the difficulties with controlling the uniform structure and thickness of the film. Yet, in the literature, it is found that the drop coating technique has been effectively employed to deposit SnO<sub>2</sub> films<sup>59</sup>. It is also worth mentioning that there are some ways to overcome the mentioned disadvantages. One of the techniques is known as spin coating, in which a spinning table can be used to produce a centrifugal force that facilitates the uniform structure of thin film<sup>60</sup>.

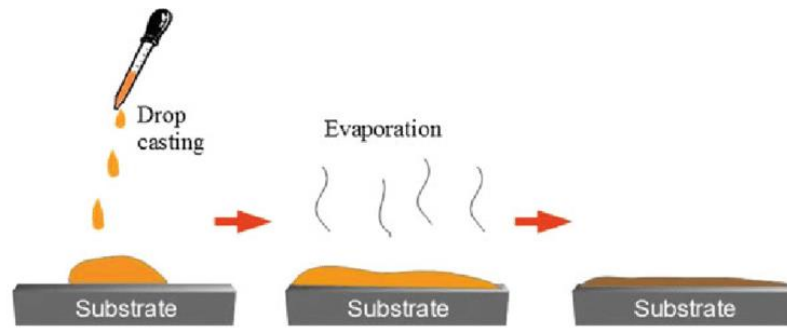


Figure 2-5. Schematic of drop coating deposition technique<sup>61</sup>

Besides the thickness effect, extensive research has been conducted on the impact of operating temperature on sensor response highlighting its critical role in influencing sensor performance<sup>4,23,60,62–73</sup>. The sensitivity and temperature have a bell-shaped curve that exhibits a maximum sensitivity point where the optimum temperature is obtained<sup>19</sup>. Below this maximum point, increasing temperature enhances the reaction rate in the sensing surface. On the other side, above the maximum sensitivity, the target gas is consumed at the surface of the sensing film before reaching deeper regions because of the high reaction rate. Moreover, when the temperature exceeds the optimal point, it leads to the desorption of chemisorbed oxygen ions from the sensor surface<sup>74</sup>.

There are several studies that use numerical models to understand the sensing mechanism in porous semiconductor metal oxide gas sensors as well as the dynamics within the measurement chamber. Sedlak et al.<sup>75</sup> investigated the effect of the flow rate of the target gas and the orientation of the gas sensor on sensor response and performance for electrochemical sensors experimentally. It is found that response and recovery time decreases as the target gas flow rate increases. In addition, the study showed that the lowest target gas flow rate compared to other studied flow rates had a negative effect on repeatability. The sensitivity and response/recovery time were improved by changing the sensor direction from parallel to the flow to vertical to the flow.

Another experimental study by Kida et al.<sup>76</sup> studied the response and recovery dynamics of semiconductor gas sensors in a fast gas switching system. The study revealed that the response time of the SnO<sub>2</sub>-based sensor for CO detection is significantly fast due to the fast reaction and diffusion dynamics. However, the recovery time is found to be larger than the response time because of the slow desorption of reaction products and adsorbed oxygen.

Furthermore, using computational fluid dynamics, Mahdavi et al.<sup>77</sup> investigated the flow rate and chamber structure effect on the performance of metal oxide gas sensors. The study concluded that increasing velocity decreases the rise time of the sensor. In addition, different configurations for sensor positions that affect the fluid flow characteristics were studied. The results showed that flow variations do not significantly affect the sensor surface temperature.

One of the studies pointed out that microfluidic gas sensors can be used as an alternative way of detection to costly techniques such as gas chromatography and mass spectroscopy systems by using different mass transfer rates in the microfluidic channel conducted by Montazeri et al.<sup>77</sup>. This numerical study investigated microfluidic flow modeling in metal oxide semiconductor gas sensors such as the one shown in Figure 2-6. The study revealed that diffusion in the microfluidic channel is the main parameter affecting the sensor response, while heat transfer had minimal effect on the sensor response. Another study that captures the detection principle and applications of the microfluidic gas sensors was conducted by Kaaliveetil et al.<sup>78</sup>. The paper pointed out that the selectivity of the gas sensor can be improved based on different diffusivities and depending on the properties of the target gas, different temporal responses can be achieved.

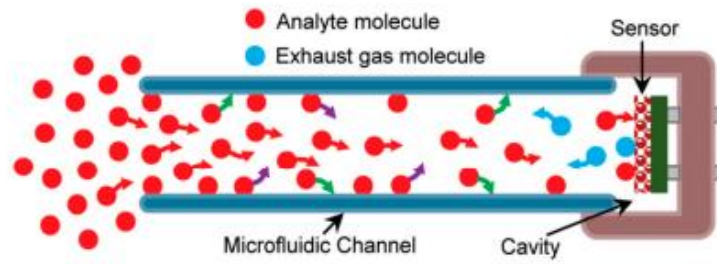


Figure 2-6. Target gas mass transfer along a microfluidic channel<sup>21</sup>

In conclusion, while existing literature provides valuable insights into the sensing mechanism of semiconductor metal-oxide gas sensors, models still need to consider the external mass transfer of the target gas prior to its interaction with the sensing surface. Current models do not consider this significant factor. Most of the aforementioned models investigate the diffusion characteristics inside the sensing layer. In practical applications of metal-oxide gas sensors, gas molecules must travel through the air before reaching the sensing layer, a process that impacts the sensor's response. Although some studies investigate the effect of flow on the sensor response experimentally, the study presented in this thesis stands out with its capability to provide a numerical model for the convective and diffusive mass transfer. In addition to solving the typical carbon monoxide detection problem at hand, it provides a methodology that could be utilized for further simulations. This is particularly valuable for industrial environments where estimation of the performance before production grants significant time reduction in the design process.



## CHAPTER 3

### MODEL DESCRIPTION

This research investigates a semiconductor metal oxide gas sensor system under transient conditions through the development of a comprehensive mathematical model. The model takes into account fluid flow, mass transfer, and reaction kinetics impact on the response of the gas sensor. Additionally, a conductance model is employed to characterize the sensor response further. Using the constructed model, the response dynamics and performance of the sensor are analyzed by varying key sensor parameters such as target gas inflow concentration, inlet velocity, operating temperature, the sensing film's thickness, the sensing film, and the porosity of the sensing film. Simulations were carried out on COMSOL Multiphysics software to explain the operating principle of metal oxide semiconductor gas sensors at different operating conditions. Overall, this study provides insights into the complex dynamics of semiconductor metal oxide gas sensors under transient conditions and highlights the importance of considering multiple factors when modeling their behavior.

The model is constructed by considering two rectangular domains, as seen in Figure 3-1. The outer domain is called the measurement chamber throughout the study. The measurement chamber is the domain where the carbon monoxide-air gas mixture is introduced with an inlet velocity. The sensing film is placed at the bottom center of the measurement chamber to minimize flow disturbances within the system.

The model considers the following:

- Two-dimensional convective and diffusive mass transfer of carbon monoxide within the measurement chamber
- Two-dimensional mass transfer of carbon monoxide within the sensing film coupled with the oxidation reaction

- Chemisorption and ionization reactions of oxygen molecules coupled with oxidation reaction with carbon monoxide based on the Eley-Rideal mechanism
- Conductance model that relates the Schottky barrier between the grains to electrical conductance
- Two-dimensional electrical current model that relates conductance with the applied voltage

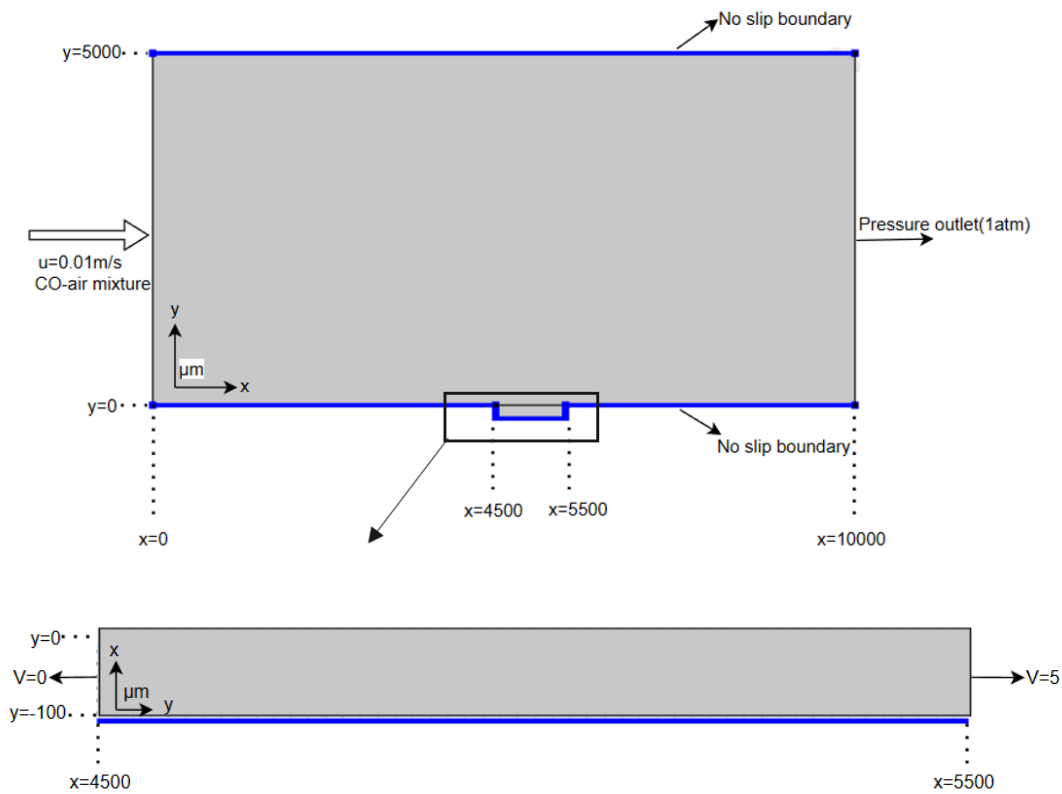


Figure 3-1. Geometry of the measurement chamber and the sensor for the model

The model is constructed based on the following assumptions:

- The flow behavior in the measurement chamber is assumed to be laminar.
- Incompressible flow is assumed.
- No slip boundary condition is assumed.
- A fully developed flow is assumed, and entrance effects are neglected.
- The sensor and the fluid temperature are assumed to have prior heating to the same temperature, varying between 450 K and 800 K.
- The uniform temperature distribution is assumed.
- Two-dimensional mass transfer of carbon monoxide is considered.
- The particle diameter range of SnO<sub>2</sub> sensing film leads Knudsen diffusion coefficient to dominate over surface diffusion.
- Humidity effects are neglected.
- The grains of the metal oxide are assumed uniform, and neck formation and agglomeration effects are neglected.
- The Eley-Rideal mechanism that considers only the adsorption of oxygen molecules and the reaction of carbon monoxide with pre-adsorbed ionized oxygen molecules is assumed.
- O<sup>-</sup> species dominates over other forms of negatively charged ions of oxygen.
- The diffusion of oxygen molecules within the sensing film is neglected.
- The chemisorption reaction of oxygen molecules is assumed to be steady state.
- All donors are assumed to be ionized, and each donor donates an electron to the conduction band.

### 3.1 The Transport of the Target Gas and Reaction Kinetics

The semiconductor tin dioxide gas sensor is placed inside a measurement chamber where there is no target gas and no flow initially. Before target gas exposure to the sensor, oxygen molecules are absorbed on the SnO<sub>2</sub> surface and reach an acceptor state. This leads chemisorbed oxygen molecules to be ionized and reach an equilibrium state. The system is stagnant initially at atmospheric conditions. At t=0, air(21% O<sub>2</sub> + 79% N<sub>2</sub>)-CO (200ppm (v/v)) gas mixture is introduced with a controlled total flow rate from the entrance of the measurement chamber.

#### 3.1.1 Laminar Flow Interface

The gas mixture has low Reynolds numbers, and viscous forces dominate and diminish disturbances so that the flow is assumed to be laminar. The Reynolds number is expressed in Equation 1 where  $\rho$ ,  $u$ ,  $L$ , and  $\mu$  denote the density of the fluid, the fluid flow speed, characteristic length, and dynamic viscosity of the fluid, respectively. In addition, the flow is fully developed throughout the domain, and entrance and end effects are neglected so that there is no significant change in the velocity profile in the direction of flow.

$$Re = \frac{\rho \cdot u \cdot L}{\mu} \quad 1$$

The gas mixture flow is modeled with Navier-Stokes equations by assuming that the flow is incompressible Newtonian fluid<sup>79</sup>. No slip boundary condition is defined at the top and the bottom of the measurement chamber to model that the fluid velocity relative to the wall velocity is zero for the stationary surfaces.

$$\nabla \cdot (\rho u) = 0 \quad 2$$

$$\rho \left( \frac{\partial u}{\partial t} \right) + \rho(u \cdot \nabla)u = -\nabla p + \mu \nabla^2 u \quad 3$$

where  $u$ ,  $p$ ,  $\rho$ ,  $\mu$  correspond to flow velocity, pressure, density, and dynamic viscosity, respectively. The inlet velocity is specified, and the outlet boundary condition is set as suppress backflow with 1 atm to prevent fluid entrance through the outlet as in the real case.

In the measurement chamber, there is no reaction taking place. Only convection and diffusion mechanism takes place. The following equation describes the concentration distribution in this domain.

$$\frac{\partial c_{CO}}{\partial t} = D \nabla^2 c_{CO} + u \cdot \nabla c_{CO} \quad 4$$

where  $u$ ,  $D$ ,  $c$  corresponds to the gas velocity, diffusion coefficient, and concentration of the species, respectively. The gas sensing starts when carbon monoxide molecules transfer along the measurement chamber and reach the sensor surface.

The temperature dependency of the diffusion coefficient of CO in the air inside the measurement chamber is found by fitting a linear curve to the empirical data<sup>80</sup>. The corresponding diffusion coefficient at different operating temperatures is found by interpolation or extrapolation based on Equation 5.

$$D_{CO} = 1.867 \times 10^{-7} \cdot T - 3.947 \times 10^{-5} \text{ m}^2/\text{s} \quad 5$$

Schmidt number is a dimensionless number in order to describe the relative importance of momentum transport and mass transfer of species in the fluid flow, which is defined as Equation 6.

$$Sc = \frac{v}{D} \quad 6$$

where  $v$ , and  $D$  correspond the kinematic viscosity of the fluid and diffusion coefficient, respectively. A higher Schmidt number indicates that momentum transport is dominant compared to mass transfer. For carbon monoxide molecules at 600 K, it is calculated as 0.36. This means carbon monoxide molecules have relatively high diffusivity in the air compared to momentum transfer. This implies that carbon monoxide molecules can easily diffuse within the air mixture.

### 3.1.2 Porous Media Transfer

Inside the sensor, the transport model considers the advection, the diffusion, and the reaction of gas molecules within the semiconductor metal oxide gas sensor. The mass transfer model considers the combined effect of the movement of gas molecules due to the flow of the gas and the movement of gas molecules due to the concentration gradient. In addition, the reaction term describes the rate of change of the concentration of the target gas due to the reaction with ionized oxygen.

$$\frac{\partial c_{CO}}{\partial t} + \nabla(-D_{k,eff} \nabla c_{CO}) + u \cdot \nabla c_{CO} = R_{rxn} \quad 7$$

where  $c$  is the concentration of gas molecules,  $t$  is time,  $D_{k,eff}$  is the effective diffusion coefficient,  $u$  is the velocity of the gas, and  $\nabla$  is the gradient operator.

The reaction term in the mass transfer equation corresponds to the carbon monoxide oxidation reaction with ionized oxygen molecules.  $Av$  refers to Avogadro's number, while  $a$  stands for the specific surface area of  $\text{SnO}_2$ .

$$R_{rxn} = -k_{3,0} \cdot \exp\left(\frac{-E_3}{RT}\right) \cdot c_{CO} \cdot N_S \cdot \frac{1}{Av} \cdot a \quad 8$$

In order to take into account of mesoporous structure of  $\text{SnO}_2$ , Knudsen diffusion coefficient is used for the target gas diffusion where  $r$  is the pore radius,  $R$  is the universal gas constant, and  $M$  is the molecular weight of the gas molecule<sup>81</sup>.

$$D_k = \frac{4r}{3} \sqrt{\frac{2RT}{\pi M}} \quad 9$$

The volume available to fluid transport is taken into account in order to model the diffusion coefficient in the porous media by using effective diffusion based on the approximation of the Bruggeman relation for porous materials<sup>82</sup>.

$$D_{k,eff} = \frac{\varepsilon}{\tau} D_{void} \quad 10$$

$$\tau = \varepsilon^{-0.5} \quad 11$$

The gas flow through the porous medium is explained by Darcy's law. The gas flow rate through the porous medium is based on the permeability of the sensing material. In order to estimate the permeability of the porous medium Carman-Kozeny empirical model is used by considering laminar flow<sup>83</sup>.

$$K_{C-K} = \frac{d_p^2}{180} \frac{\varepsilon^3}{(1 - \varepsilon)^2} \quad 12$$

$$U = \frac{-K}{\varepsilon \mu} \nabla p$$

13

where  $U$ ,  $K$ ,  $\mu$ ,  $p$ ,  $\varepsilon$  correspond to darcy velocity, permeability, the dynamic viscosity of the fluid, pressure, and porosity, respectively. Darcy equation describes the flow velocity of the fluid through the porous medium by considering a pressure-driven mass transfer.

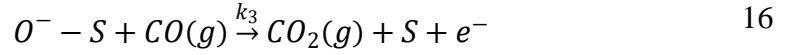
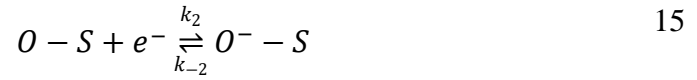
The initial and boundary conditions for the model is given in Table 3-1. The solution of the equations provides information about the temporal and spatial distribution of the target gas in the system.

Table 3-1. Initial and boundary conditions of the model

Initial Conditions:	Boundary Conditions:
$c_{CO}(x, y, t = 0) = 0$  $u(x, y, t = 0) = 0$	$u(x = 0, y, t) = 0.01 \text{ m/s}$  $c_{CO}(x = 0, y, t) = 0.00714 \frac{\text{mol}}{\text{m}^3}$
No Flux Boundary Conditions:	
$\frac{\partial c_{CO}}{\partial x}(x = 4500, -100 < y < 0, t) = 0$  $\frac{\partial c_{CO}}{\partial y}(4500 < x < 5500, y = -100, t) = 0$  $\frac{\partial c_{CO}}{\partial y}(0 < x < 4500, y = 0, t) = 0$	$\frac{\partial c_{CO}}{\partial x}(x = 5500, -100 < y < 0, t) = 0$  $\frac{\partial c_{CO}}{\partial y}(0 < x < 10000, y = 5000, t) = 0$  $\frac{\partial c_{CO}}{\partial y}(5500 < x < 10000, y = 0, t) = 0$

### 3.1.3 Reaction Kinetics

In order to explain reaction kinetics inside the sensing film adsorption, ionization and the reaction between the target gas and pre-adsorbed ionized oxygen molecules are considered based on the Eley-Rideal mechanism. This mechanism is based on the adsorption of one reactant to the surface while the other reactant directly reacts with the pre-adsorbed species. Chemisorption is associated with the neutral state of adsorption of oxygen molecules, while ionization creates ionized oxygen from adsorbed neutral oxygen molecules. When carbon monoxide gas molecules come into contact with SnO<sub>2</sub> material, it reacts with the pre-adsorbed ionized oxygen molecules. Following reactions given in Equation 14, Equation 15, and Equation 16 explain chemisorption, ionization, and oxidation reactions, respectively.



The major aim is to find two main differential equations that show the ionized oxygen density and carbon monoxide consumption which is coupled with the transport equation.

The differential equation for the neutral oxygen molecules that explains reversible chemisorption and ionization reactions is constructed as seen in Equation 17.

$$\frac{dN_o}{dt} = k_1([S] - N_o - N_s)[O_2]^{1/2} - k_{-1}N_o - k_2n_sN_o - k_{-2}N_s \quad 17$$

$N_O$  and  $N_S$  refer to chemisorbed neutral oxygen [O-S] and ionized oxygen density  $[O^- - S]$ , respectively. In addition,  $[S]$  and  $n_s$  represent total available adsorption sites and electron concentration, respectively. The latter is expressed in Equation 18.

$$n_s = N_d \exp\left(\frac{-q^2 N_S^2}{2k_B \epsilon_r \epsilon_0 N_d T}\right) \quad 18$$

The number of total adsorption sites is assumed to be much larger than the sum of chemisorbed and ionized oxygen density so that Equation 17 is simplified to Equation 19. As stated before, because of the higher reactivity of oxygen molecules with the sensor surface, the rate-determining step is determined by the ionization reaction. For this reason, the chemisorption reaction is assumed to be in a steady-state.

$$\frac{dN_O}{dt} = k_1[S][O_2]^{\frac{1}{2}} - k_{-1}N_O - k_2n_sN_O - k_{-2}N_S = 0 \quad 19$$

$$\frac{dc_{CO}}{dt} = -k_3N_Sc_{CO} \quad 20$$

Steady-state expression for the chemisorbed oxygen is placed into ionized oxygen differential equation, as seen in Equation 21.

$$\frac{dN_S}{dt} = k_2n_sN_O^0 - k_{-2}N_S - k_3N_Sc_{CO} \quad 21$$

Substituting steady-state neutral oxygen density into Equation 21 leads to Equation 22.

$$\frac{dN_S}{dt} = k_2 N_d \exp\left(\frac{-q^2 N_S^2}{2k_B \epsilon_0 \epsilon_r N_d T}\right) \left[ \frac{k_1 [S][O_2]^{\frac{1}{2}} + k_{-2} N_S}{\frac{k_{-1}}{k_2} + N_d \exp\left(\frac{-q^2 N_S^2}{2k_B \epsilon_0 \epsilon_r N_d T}\right)} \right] - k_{-2} N_S - k_3 N_S c_{CO} \quad 22$$

In order to make the ionized oxygen density differential equation temperature dependent, the reaction rate constants are expressed with Arrhenius expression, and the differential equation has the final form given in Equation 23.

$$\frac{dN_S}{dt} = \exp\left(\frac{-q^2 N_S^2}{2k_B \epsilon_0 \epsilon_r N_d T}\right) \left( \frac{k_{10} \exp\left(\frac{-E_1}{RT}\right) [S][O_2]^{\frac{1}{2}} + k_{-20} \exp\left(\frac{-E_{-2}}{RT}\right) N_S}{\left(\frac{k_{-10}}{k_{-20} N_d}\right) \exp\left(\frac{-(E_{-1}-E_2)}{RT}\right) + \exp\left(\frac{-q^2 N_S^2}{2k_B \epsilon_0 \epsilon_r N_d T}\right)} \right) - k_{-20} \exp\left(\frac{-E_{-2}}{RT}\right) N_S - k_{30} \exp\left(\frac{-E_3}{RT}\right) N_S c_{CO} \quad 23$$

Before the target gas reaches the sensor surface, the SnO<sub>2</sub> sensor is at equilibrium between the neutral oxygen and negatively charged oxygen ions. Initial ionized oxygen density is calculated for each temperature when there is no carbon monoxide in the sensor, and the rate of ionization of oxygen molecules is equal to the rate of reverse ionization of oxygen molecules.

### 3.2 Conductance and Electrical Current Model

The conductance model explains the changes in the conductivity due to sensor surface charge distribution caused by the gas reaction. The drift-diffusion equation, given in Equation 24, is used to explain the electrical current in the semiconductors<sup>33</sup>.

$$\vec{J} = q \cdot n_s \cdot \mu_s \cdot \vec{E} + q \cdot D \cdot \nabla n_s \quad 24$$

where  $\vec{J}$ ,  $\mu_s$ ,  $D$ ,  $q$ , and  $n_s$  correspond to current density, carrier mobility, the diffusion coefficient of carriers, the charge of electrons, and electron concentration, respectively. The thickness of the space charge carrier layer is assumed to have a small size compared to the average electron-free path, so the diffusion term in Equation 24 is neglected. The conductivity is the ratio of the current flux to the electric field, so the conductivity equation is finally expressed as in Equation 26. The mobility is a function of temperature only so that the conductivity is only dependent on the electron concentration at a certain temperature.

$$\sigma = \vec{J} / \vec{E} \quad 25$$

$$\sigma = q \cdot n_s \cdot \mu_s \quad 26$$

The grain size is assumed as greater than the width of the depletion layer so that the inter-grain contact conductance is considered. In order to get the value of  $n_s$ , the charge conservation inside the depletion layer can be investigated as shown in Figure 3-2. The density of surface charge ( $\rho$ ) is calculated by the Poisson equation given in Equation 27.

$$-\nabla(\epsilon_0 \epsilon_r \nabla V) = \rho \quad 27$$

where  $\epsilon_0$ ,  $\epsilon_r$ , and  $V$  corresponds to vacuum permittivity, the relative permittivity of the material, and potential energy, respectively.

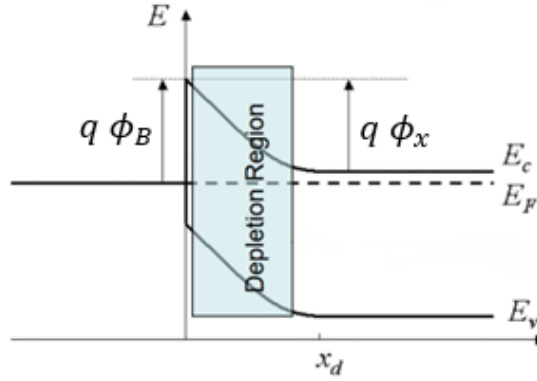


Figure 3-2. Band energy and depletion layer between the grains<sup>84</sup>

Inside the depletion layer, charge  $q\phi_x$  density is given by  $qN_i$  where  $N_i$  is the net density of ions.  $V$  is related to the Fermi level energy of the semiconductor material  $\phi_b$  and the potential inside the depletion layer  $\phi_x$  as given below.

$$V(x) = \phi_b - \phi_x \quad 28$$

Then the solution of the Poisson equation yields,

$$V = \frac{q \cdot N_i (x - x_0)^2}{2\epsilon_0\epsilon_r} \quad 29$$

where  $x_0$  is the thickness of the depletion region. In this equation,  $N_i$  can be written as  $N_i = N_s/x_0$  where  $N_s$  is the number of electrons moved to the surface. The voltage at  $x_0$  is then calculated by equating  $\phi_{x=x_0} = \phi_b$  which gives  $V = 0$ . Substituting  $x_0^2 = N_s^2/N_i^2$  into Equation 29 gives the potential barrier at the grain boundary or the Schottky barrier. For n-type semiconductors, the net density of ions is equal to the donor density, so the  $N_i=N_d$  equality is valid. The resulting potential barrier is given by Equation 30.

$$V_s = \frac{q \cdot N_s^2}{2\epsilon_0\epsilon_r N_d} \quad 30$$

The electron density at the surface is expressed as in Equation 31 by considering Boltzmann distribution that relates the probability of finding a particle in a certain energy state.

$$n_s = N_d \cdot e^{-qV_s/k_B T} \quad 31$$

where  $qV_s$  represents the band bending energy of the surface band.

The ionized oxygen density determines the surface potential, the charge concentration, and the conductance change of the sensor. This Schottky potential energy barrier results in conductance, as given in Equation 32. This is the equation where the solved differential equation ionized oxygen density is substituted to obtain the final conductance of the sensor.

$$G(T, V_s) = G_0 \exp\left(\frac{-qV_s}{k_B T}\right) + G_c \quad 32$$

where  $G_c$  is conductance constant while the pre-exponential term is expressed as Equation 33.

$$G_0 = gq\mu_s N_d \quad 33$$

where  $g$ ,  $q$ ,  $\mu_s$  and  $N_d$  corresponds to semiconductor geometry constant, electron charge, mobility of electrons, and ionized donor density, respectively.

In order to model two-dimensional electrical current through the sensing film, two electrodes are applied to two center points of the side boundaries of the sensor, as seen in Figure 3-3. The ground node is applied to one side point at 0 V while the other side is exposed to an electrical potential of 5 V. The electrical current flux is described, as seen in Equation 34.

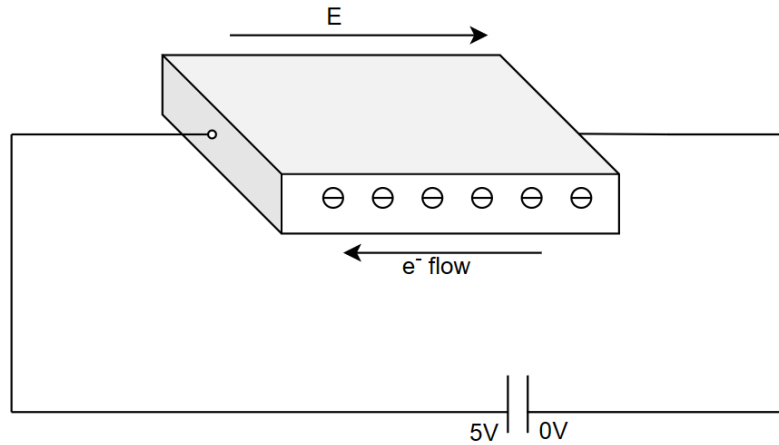


Figure 3-3. Electrical current inside the sensing film

$$\vec{j} = \frac{A \cdot V}{R} \quad 34$$

where  $\vec{j}$ ,  $A$ , and  $R$  correspond to current density, the cross-sectional area of the sensor that is the width multiplied by the thickness and resistance, respectively. Resistance is expressed in terms of conductance as  $R=1/G$ .

In this study, it is assumed that both the gas mixture and the sensor is heated to a certain temperature prior to operation, and as stated, a constant DC voltage is applied to two sides of the sensing film as 0-5V. The model considers joule heating in which temperature increases due to the resistive heating from electrical current.

$$P = V^2/R \quad 35$$

where  $P$ ,  $V$  and  $R$  correspond to the dissipated power, the voltage applied on both sides of the film with electrodes and the total resistance, respectively. The total heat dissipated is calculated by integrating the power in Equation 36.

$$Q = \int_{t_0}^{t_f} P dt \quad 36$$

where  $t_0$ , and  $t_f$  correspond to initial time and final time points. The calculated total heat is investigated to observe temperature changes within the sensing film based on Equation 37.

$$Q = m c_p \Delta T \quad 37$$

Most devices that integrate such kind of thin film sensors utilize active control of the heater circuit underneath the sensing layer. This results in a layer that is operating at constant temperature despite the self-heating effect.  $\Delta T$  is calculated as 3.3 Kelvin so that the resulting heat dissipation is found to have almost no contribution to the heat transfer and heat distribution inside the measurement chamber.

### 3.3 COMSOL Multiphysics

In order to simulate and analyze semiconductor metal oxide gas sensor dynamic behavior under different operating conditions, COMSOL Multiphysics is used as a finite element analysis software. The laminar flow physics is used to simulate the flow of gas mixture from the entrance of the outer domain before it reaches the sensor surface and to simulate the porous matrix in the sensor. The transport of diluted species physics is utilized to simulate the gas transport for both the outer domain and sensor surface. The COMSOL Multiphysics is utilized in order to couple laminar flow physics and transport of diluted species physics. This flow coupling interface takes the laminar flow module as the source and couples with the transport of diluted species module as the destination. In addition, the domain ODEs and DAEs physics is applied to solve the complex equation of the rate of change of ionized oxygen with respect to time. Furthermore, electrical current physics is applied in order to analyze

the conductance and electrical current model. The heat transfer model is used to simulate heat dissipation caused by resistance changes in the sensor.

### 3.3.1 Time Discretization

An important factor in representing fluid flow behavior is the Courant number ( $Co$ ). In computational fluid dynamics (CFD), the Courant number, a dimensionless variable, is used to evaluate the stability and convergence of numerical simulations. It is particularly crucial in microfluidic systems where small sizes are common. The Courant number is defined as the relationship between the typical fluid velocity and the characteristic length scale of the system, multiplied by the time step<sup>85</sup>. It has the following mathematical representation:

$$Co = \frac{(u \cdot \Delta t)}{\Delta x} \quad 38$$

The difference between the size of the discretized spatial domain and the fluid's step-by-step travel distance is characterized by  $Co$ . If the fluid moves only a small portion of the spatial domain in one time step, Courant number will be low. A very low Courant number may require more processing time and resources without significantly improving solution accuracy. In contrast, a Courant number that is too high might cause numerical instability and erroneous predictions.

### **3.3.2 Model Parameters**

The parameters for the model adopted from various studies from the literature are presented in Table 3-2 to provide a clear and accessible overview. These parameters are crucial to model the sensing mechanism and the performance because all parameters represent the underlying mathematical and conceptual principles that govern the model's behavior. The careful adoption of these parameters from previous studies ensures that the model is built upon tested assumptions, enhancing the reliability of this research.

Table 3-2. Model parameters and units

Model Parameter	Value	Unit	Reference
$q$	$1.602 \times 10^{-19}$	C	
$k_B$	$1.381 \times 10^{-23}$	$m^2.kg/s^2.K$	
$\epsilon_0$	$8.854 \times 10^{-12}$	F/m	86
$\epsilon_r$	12		87
$N_d$	$10^{24}-10^{26}$	$1/m^3$	88
$k_{-2,0}$	0.0001-0.106	1/s	44
$\frac{k_{-1,0}}{k_{2,0}N_d}$	81.45-92.44		44
$k_{3,0}[c_{CO}]^*$	0.0001-16.7	1/s	44
$k_{1,0}[S][O_2]^{1/2} \frac{q}{\sqrt{2\epsilon_0\epsilon_r N_d k_B}}$	5068-1745000	$K^{1/2}/s$	44
$E_1$	31453-72043	J/mol	44
$E_{-2}$	4641-17053	J/mol	44
$E_{-1} - E_2$	55340-58582	J/mol	44
$E_3$	5122-37414	J/mol	44
$\epsilon$	0.2-0.5		89
$d_p$	1-25	nm	90
$Av$	$6.02 \times 10$	1/mol	23
$v$	$2.62 \times 10^{-5}$	$m^2/s$	93
$G_0$	2	S	91
$M$	28.01	g/mol	
$a$	32	$m^2/g$	92
$D_h$	0.005	m	
$w$	0.005	m	
$c_p$	48.7	J/mol.K	93
$\rho_{SnO_2}$	6.95	$g/cm^3$	80

\*[ $c_{CO}$ ] is taken as 200 ppm in the reference

### 3.3.3 Mesh Independency

Mesh independency is a critical component of this research, providing confidence that the outcomes remain stable, regardless of the size variations in the model's elements. The simulations start with larger elements in the mesh. These elements undergo a process of refinement, becoming smaller. Significant changes in conductance values are observed with the first refinement. However, a point is eventually reached, known as mesh independency, where further refinement results in minimal changes to the conductance value, as shown in Figure 3-4.

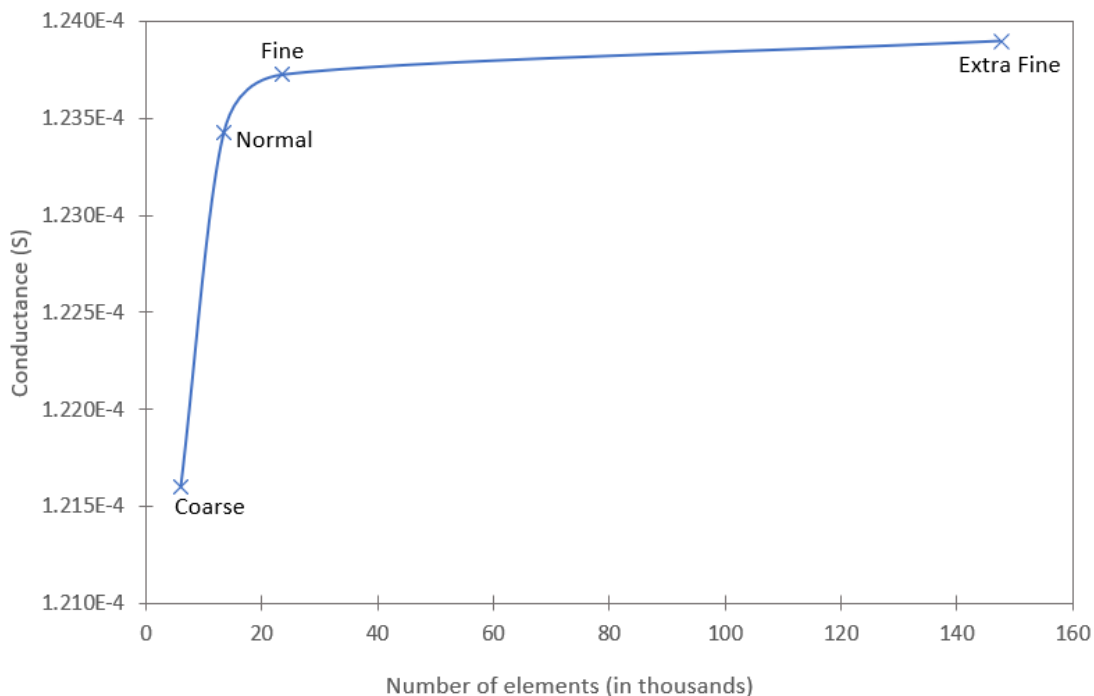


Figure 3-4. Relationship between steady-state conductance and the number of elements in different meshes

In addition, in Figure 3-5, it is seen that the spatial distribution of conductance changes significantly with the mesh size. This is also a crucial observation, as the purpose of this study is to capture the effect of reaction, diffusion, and convection interactions causing spatial gradients.

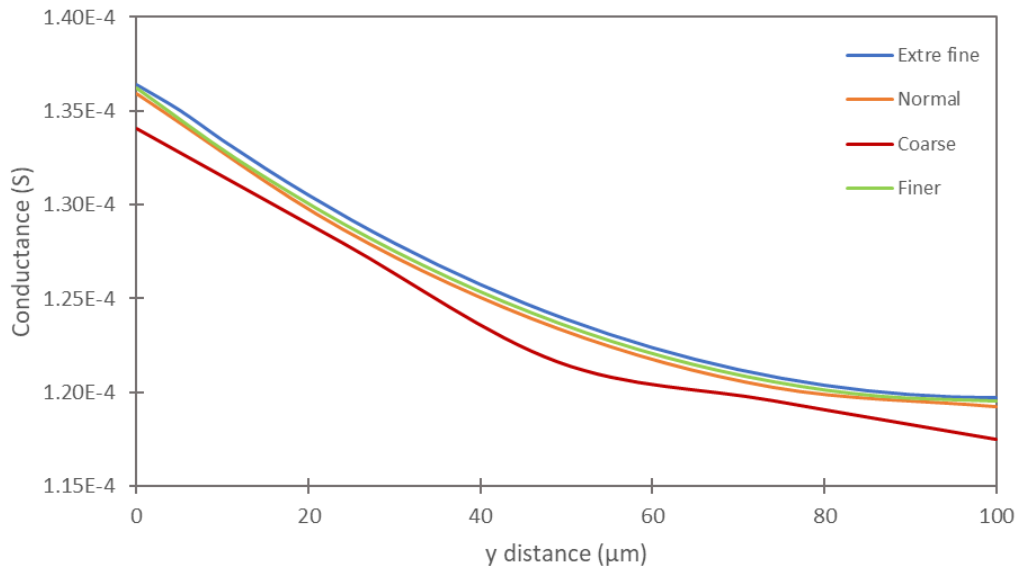


Figure 3-5. Conductance spatial distribution for varying meshes

Achieving mesh independence does not promise an absolutely accurate solution. However, it suggests that any errors introduced due to the mesh size selection are minor enough to be disregarded for the purpose of this study. When mesh independence is achieved in the simulations, it confirms the credibility of the conductance findings of the gas sensor. It ensures that the results accurately capture the sensor's physical behavior rather than being influenced by numerical errors. In Figure 3-6, extra fine mesh is shown, which has been used as the reference or the benchmark.

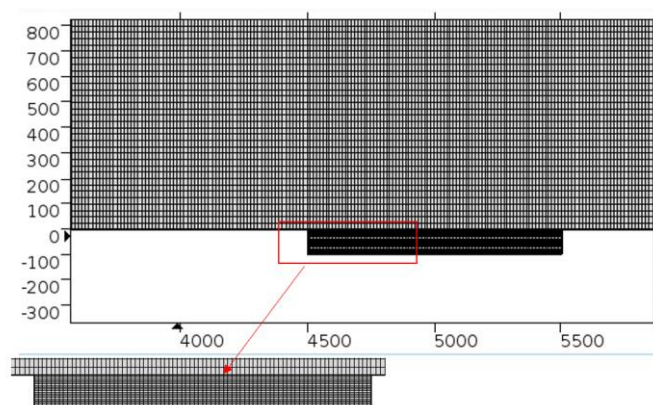


Figure 3-6. Extra fine mesh structure



## CHAPTER 4

### RESULTS AND DISCUSSION

In the following section of this thesis, the results and discussion derived from the computational analysis of the study are presented. The focus of this study is on understanding the behavior of n-type semiconductor metal oxide gas sensors to the reducing gas (CO) in an excess oxygen environment under various conditions by utilizing simulations. The conditions and the sensor parameters are determined by considering typical ranges of semiconductor metal oxide gas sensors for CO detection produced and tested by Figora<sup>94</sup>. The interaction between laminar flow physics, transport of diluted species physics, reaction kinetics, and electrical conductance is considered essential in the functioning of the semiconductor metal oxide gas sensors, which form the backbone of this investigation. The constructed model explains:

- The microfluidic flow in the measurement chamber, which was modeled as laminar flow of the air-CO mixture
- Two-dimensional mass transfer of CO in the sensing film from the surface and the surface reaction between CO and ionized oxygen molecules
- The reversible chemisorption and ionization reaction of oxygen molecules
- The conductance model based on the surface potential barrier between metal oxide grains
- Two-dimensional electrical current model

The results explain the methodology used in this study and present a detailed analysis of the findings and the knowledge gained from this research. The simulations were performed in COMSOL Multiphysics. In addition, the ordinary differential equation representing the change of ionized oxygen density based on the chemisorption and

ionization reactions was numerically solved in order to find the initial equilibrium density of the ionized oxygen for different temperatures by utilizing MATLAB.

#### **4.1 Transient Analysis of CO Detection**

The SnO<sub>2</sub>-based semiconductor gas sensor having 100 μm thickness was exposed to CO (200ppm (v/v)) - air (21% O<sub>2</sub> + 79% N<sub>2</sub>) mixture with an inlet velocity of 0.01 m/s to the measurement chamber to investigate the sensor response at an operating temperature of 600 Kelvin. The porosity is taken as 0.2 as the default condition. Initially, there is no CO inside the measurement chamber and the sensor. At t=0 CO-air mixture is introduced from the inlet of the chamber. The spatial distributions of CO concentration, ionized oxygen density, and electrical current flux were investigated to understand the sensor detection mechanism. In addition, the timewise change in sensor response was investigated. The sensor response refers to the change in the electrical conductance of the sensor.

##### **4.1.1 CO Concentration Spatial Distribution Timewise Comparison**

Figure 4-1 displays the CO concentration spatial distribution profile timewise change within the sensing film. The x-axis represents the distance between the sensor surface and the bottom of the sensor, while the y-axis corresponds to the CO concentration. Through the thickness of the sensing film, x=0 refers to the sensor surface, while x=100 μm corresponds to the bottom of the sensor, which is the impermeable boundary. Different lines correspond to different time points until the system reaches a steady state.

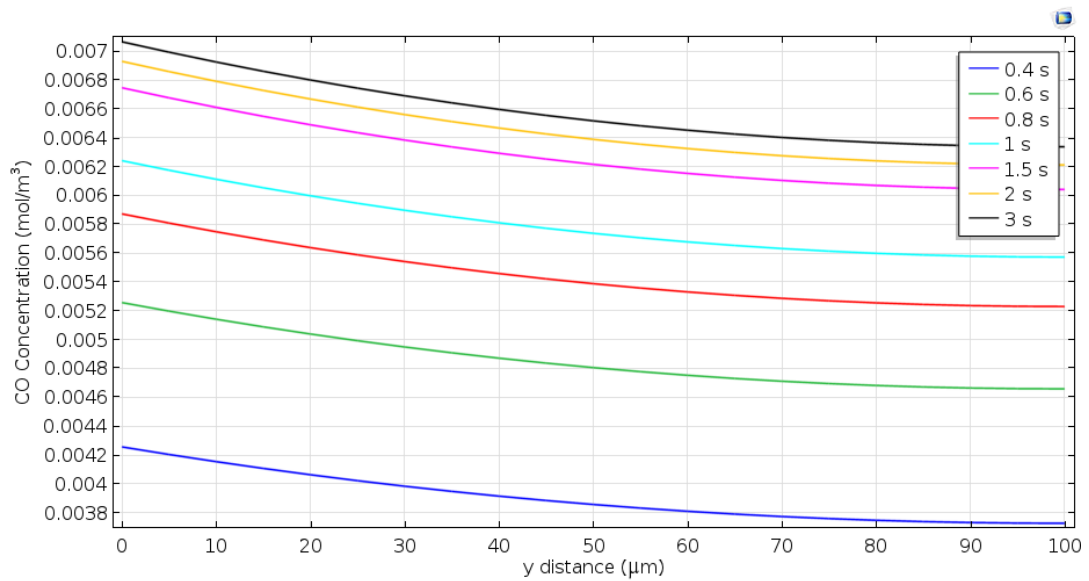


Figure 4-1. CO concentration profile at the vertical line placed in the center of the 100 μm sensing film at 600 K exposed to 200 ppm of CO, with an inlet velocity of 0.01 m/s

The sensor surface is exposed to different concentrations of CO at each temporal point. This is the effect of air movement on top of the sensor, and it is beneficial to investigate the behavior of the sensor under these conditions to understand response characteristics in an actual case where target gas is introduced with the air flow. The spatial distribution is nonuniform through the vertical direction inside the sensor. The nonuniform spatial distribution inside the sensor is primarily caused by the reaction of CO with ionized oxygen while the molecules are diffusing. This spatial distribution of CO concentration reflects the competing effect of CO supply from the outer domain with fluid flow and CO consumption with the oxidation reaction. The curves became closer as time progressed, indicating that the system approached the steady state condition. The effective parameters in this process are the porosity and particle diameter of the metal oxide sensor, which affects the diffusion rate. This has a similarity with what affects only diffusive transport. In this model, what is distinguishably influential is the impact of inlet fluid velocity at the convective mass transfer coefficient. This effect will further be elaborated in the upcoming sections that compare the sensor behavior under different velocities.

Figure 4-2 represents CO concentration change along the center longitudinal axis inside the sensor. Along the x-axis,  $x=0$  is the left wall of the sensor, while  $x=1000 \mu\text{m}$  is the right end of the sensor. It is seen that the concentration of CO gradually decreases from left to right because CO was introduced from the entrance that is placed to the left side of the measurement chamber. The mass transfer coefficient changes through the longitudinal direction. This can be explained by the change in the local Sherwood number along the sensor surface, as seen in Figure 4-3.

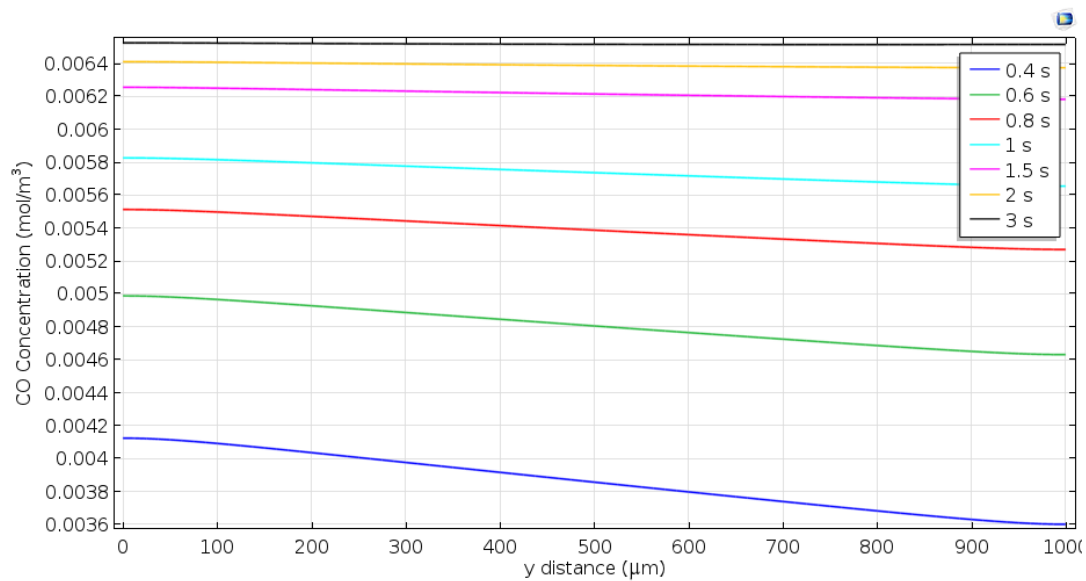


Figure 4-2. CO concentration profile at the horizontal line placed in the center of the  $100 \mu\text{m}$  sensing film at  $600 \text{ K}$  exposed to  $200 \text{ ppm}$  of CO, with an inlet velocity of  $0.01 \text{ m/s}$

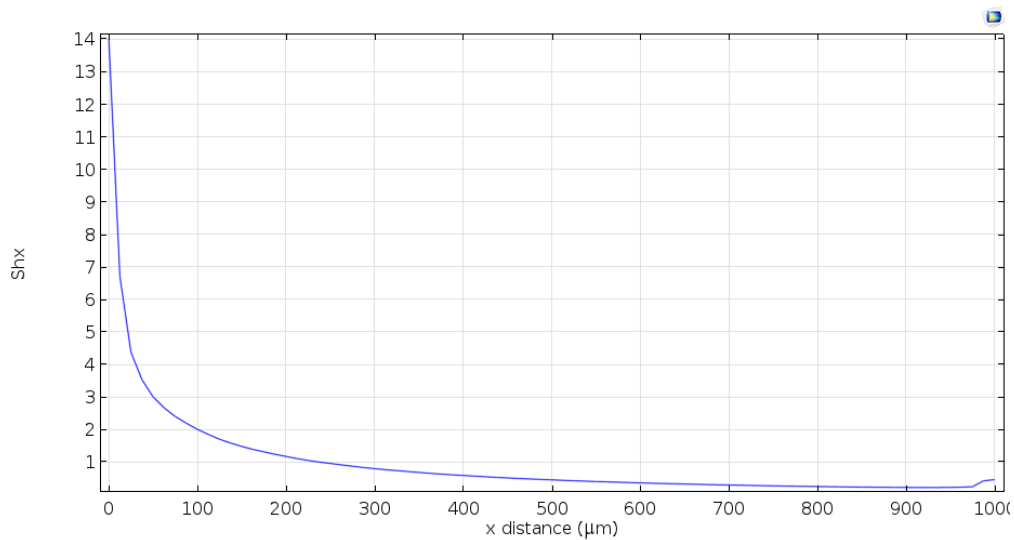


Figure 4-3. Local Sherwood number along the sensor surface at t=0.2sec

The local Sherwood number measures the ratio of mass transfer flux to the diffusive driving force as described in Equation 39 where  $\phi$ ,  $D_h$ ,  $C_\infty$ ,  $C_{surface}$ , and  $D_{CO}$  represent total mass flux, hydraulic diameter, free stream concentration, surface concentration, and diffusivity of CO in the sensor. The local Sherwood number is highest at the entrance of the sensor film, and then it decreases along the longitudinal axis. At the entrance of the sensing film, the difference between CO concentration in the flow and in the sensor surface is high due to the thin boundary layer, which causes higher mass flux. However, downstream of the sensor, this difference becomes smaller because mass transfer boundary layer thickness increases. This lower concentration gradient results in lower mass fluxes. As time passes, CO concentration in the longitudinal axis becomes uniform. This is because of the complete coverage of the surface with the laminar flow. However, at the earlier points, the flow is still not in complete contact with the sensor surface, which causes the difference in concentration in the longitudinal direction.

$$Sh_x = \frac{\phi \cdot D_h}{(C_\infty - C_{surface})D_{CO}} \quad 39$$

### 4.1.2 Ionized Oxygen Spatial Distribution Timewise Comparison

Figure 4-4 illustrates the spatial distribution of the ionized oxygen density at different time points. The x-axis corresponds to the vertical cutline in the sensor. The  $x=0$  refers to the sensor surface, while  $x=100\ \mu\text{m}$  represents the bottom impermeable boundary of the sensor. Initially, ionized oxygen is distributed homogeneously inside the sensor. When the CO reaches the sensor surface, the oxidation reaction consumes the ionized oxygen. This consumption reaction is higher at the surface because of higher CO concentrations than at the bottom of the sensor at earlier times. In addition, decreasing density indicates that the ionization reaction rate is lower than the oxidation reaction. As time passes, the oxidation reaction rate decreases, and the change of ionized oxygen becomes smaller. Ionized oxygen distribution through the sensor determines the surface potential barrier distribution of the sensor based on Equation 40.

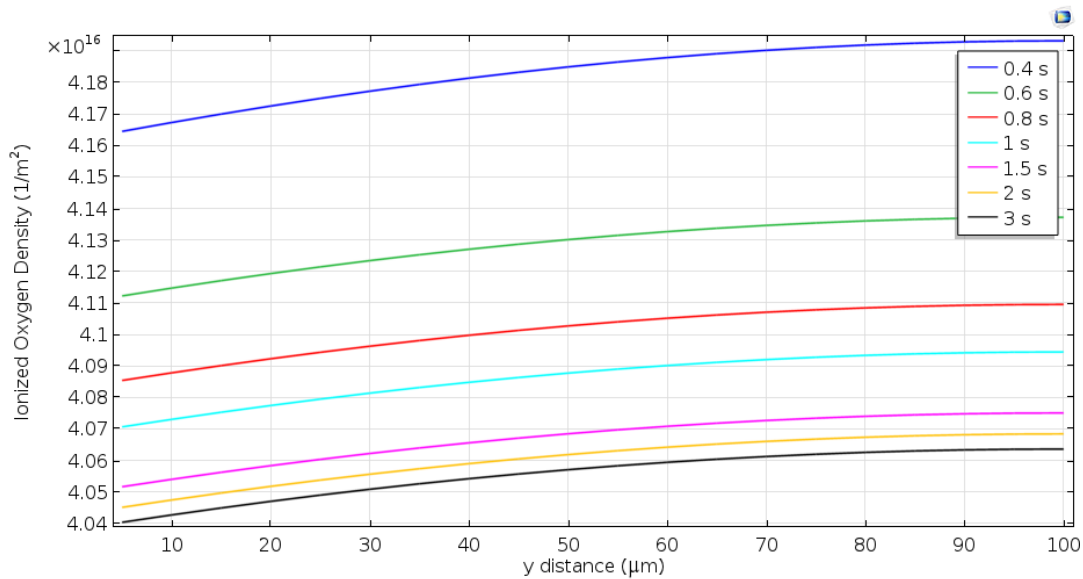


Figure 4-4. Ionized oxygen density profile at the vertical line placed in the center of the  $100\ \mu\text{m}$  sensing film at 600 K exposed to 200 ppm of CO, with an inlet velocity of 0.01 m/s

$$V_s = \frac{q \cdot N_s^2}{2\epsilon_0 \epsilon_r N_d} \quad 40$$

The surface potential barrier is lower when ionized oxygen density is less. This is because consumed ionized oxygens release free electrons to the conduction band, lowering the potential barrier and easing the electron flow inside the sensor.

Figure 4-5 represents the electrical current density spatial distribution at different time points. The x-axis corresponds to the center vertical outline of the sensing film, while the y-axis corresponds to the electrical current flux in A/m<sup>2</sup>. The electrical current density is highest near the top of the sensing film where x=0. As the point moves along the vertical outline, electrical current density decreases and has the smallest value at the deep of the sensing film.

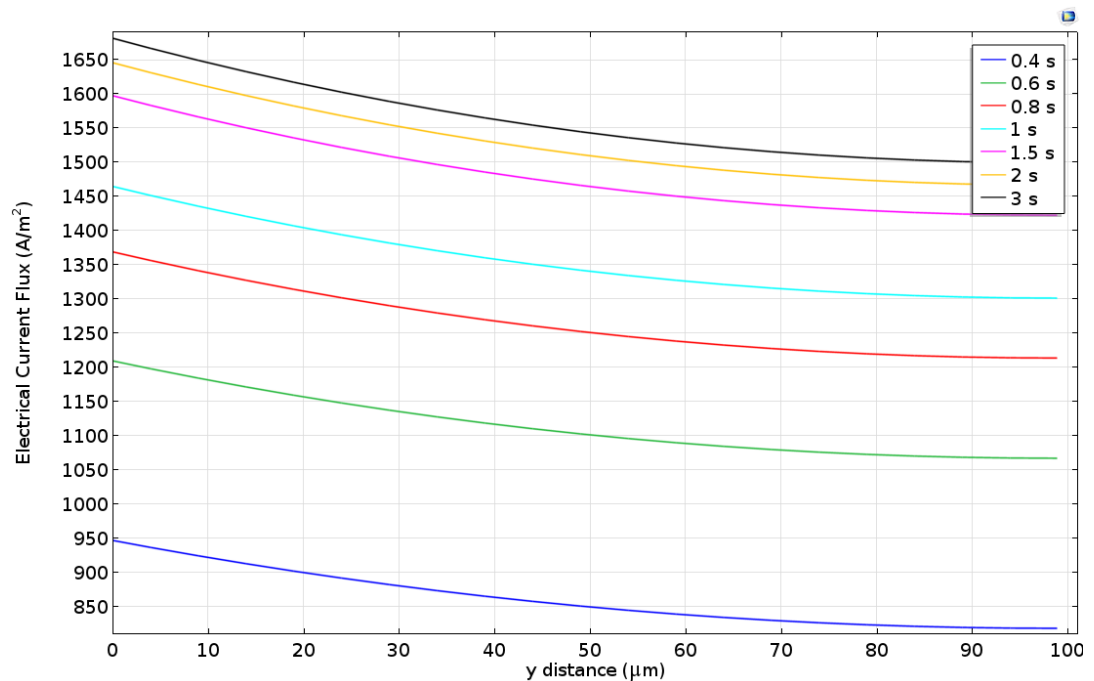


Figure 4-5. Electrical current flux profile at the vertical line placed in the center of the 100 µm sensing film at 600 K exposed to 200 ppm of CO, with an inlet velocity of 0.01 m/s

The electrical current flux, also called electrical current density, has the same trend as the ionized oxygen density because the change in the ionized oxygen density leads

to a decrease in the resistance of the sensor. This change in the resistance correlates with the difference in the current when 0-5V is applied across the sensing film. When CO molecules come into contact with the sensor, the interaction between CO and the ionized oxygen changes the charge carrier density primarily near the surface of the sensing film because of a higher surface reaction.

### 4.1.3 Surface Averaged Conductance Timewise Profile

Figure 4-6 represents the surface averaged conductance change in time. Conductance is a measure of how easily electrical current flows in the semiconductor sensor. Initially, the conductance has a low initial value that interferes with the flow of free electrons inside the semiconductor sensor. The surface averaged conductance is described by Equation 41.

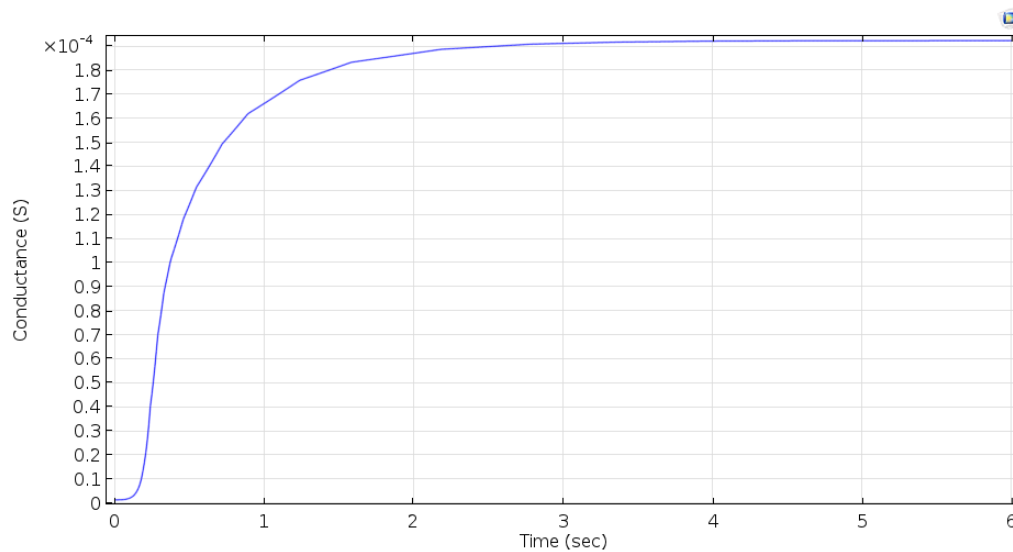


Figure 4-6. Surface averaged conductance timewise profile of the 100 μm sensing film at 600 K exposed to 200 ppm of CO, with an inlet velocity of 0.01 m/s

$$G_{avg} = \frac{1}{A} \int G dA \quad 41$$

When the CO molecules reach the sensor surface, the oxidation reaction with the ionized oxygen releases electrons to the conduction band, which improves electrical current flow in the sensor. The consumption of the ionized oxygen is greater than the production of it, thus  $\frac{dN_s}{dt}$  has a negative value. The conductance curve shows an exponential increase and reaches a steady value based on the Schottky conductance model. The model considers the charge carriers as only electrons and calculates conductance based on Boltzmann statistics. The exponential behavior of the conductance can be explained by the electron transfer rate dependency on the surface potential barrier based on Equation 42.

$$G(T, V_s) = G_0 \exp\left(\frac{-qV_s}{k_B T}\right) \quad 42$$

Decreasing the density of the ionized oxygen leads lower surface potential barrier thus conductance increases up to the equilibrium, where  $\frac{dN_s}{dt}$  becomes equal to zero. This means that the consumption and production of the ionized oxygen become equalized. The higher surface potential barrier leads to the slower change of the ionized oxygen thus slower response is obtained.

## 4.2 Effect of Inlet Concentration

The different inlet concentrations of CO in the gas mixture were investigated to observe changes in the sensor response. The expectation is that as the target gas concentration increases, more gas molecules will interact with pre-adsorbed oxygen ions. Due to the higher interaction between the target gas and ionized oxygen, more

electrons will be released to the conduction band, which results in higher conductance. However, there should be a concentration limit where conductance cannot be increased further. The study examined CO concentrations within a range of 50 ppm to 300 ppm at an operating temperature of 600 Kelvin and with an inlet velocity of 0.01 m/s. The corresponding surface averaged conductance of the sensor, surface averaged conductance, and sensor sensitivity with increasing concentrations of CO were investigated.

Figure 4-7 shows the relationship between time and surface averaged conductance in the sensor with varying inflow target gas concentrations. The x-axis represents time in seconds while the y-axis represents surface averaged conductance in Siemens.

When the CO reaches to SnO<sub>2</sub>-based sensor, the oxidation reaction leads to the donation of electrons to the sensor resulting in an increase in the concentration of free electrons within the material. This increase in free electron concentration leads to an increase in the electrical conductivity of the material. The increase in the inflow concentration of the target gas is accompanied by a corresponding increase in conductance which means more current flows through the sensor. This is mainly because of the fact that higher target gas concentrations consume more ionized oxygen and more electron released to the sensor surface. However, as seen in Figure 4-7 increase in the conductance becomes smaller as the concentration increases, which explains the sensitivity decrease.

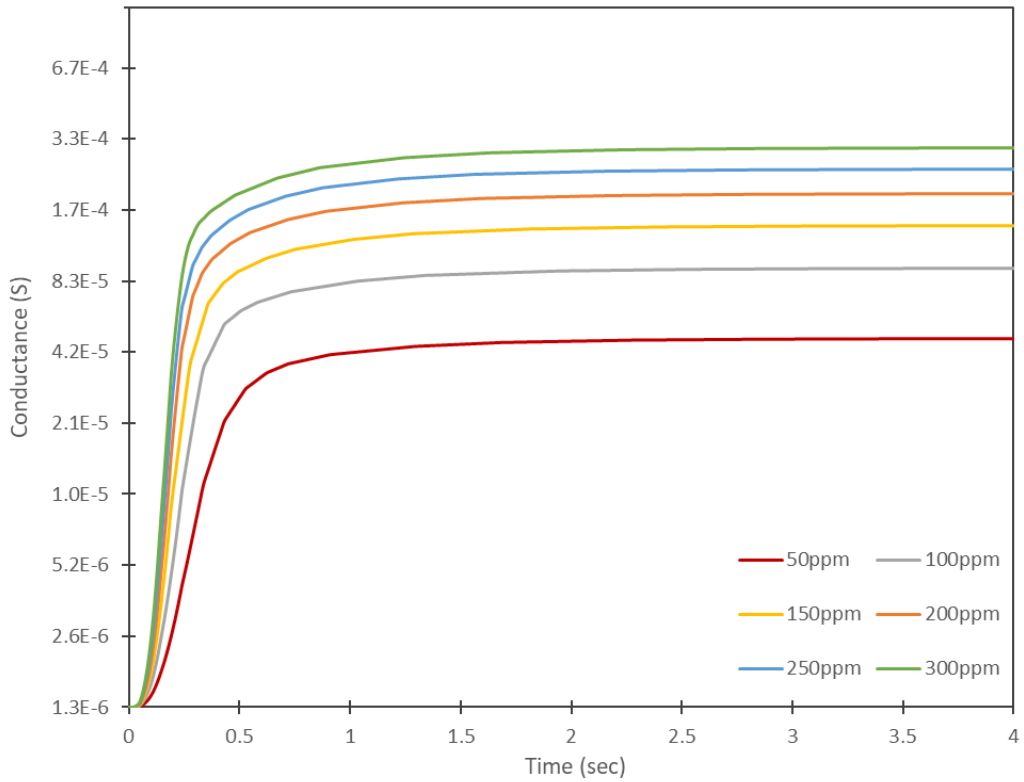


Figure 4-7. Surface averaged conductance change over time in response to different CO inlet concentrations at 600 K, with an inlet velocity of 0.01 m/s

Figure 4-8 represents the surface potential barrier for different inlet CO concentrations. The surface potential barrier has lower values near the surface of the sensor due to the surface reaction of CO. The figure shows that 50 ppm has the highest surface potential barrier. The trend indicates as the concentration increases, the higher interaction of ionized oxygen with the reducing gas reduces the surface potential barrier. The initial steady-state surface potential barrier was found as 0.74 V. The difference in surface potential barrier from the initial steady-state decreases from low concentrations to high concentrations. This means that the change in ionized oxygen density reduces.

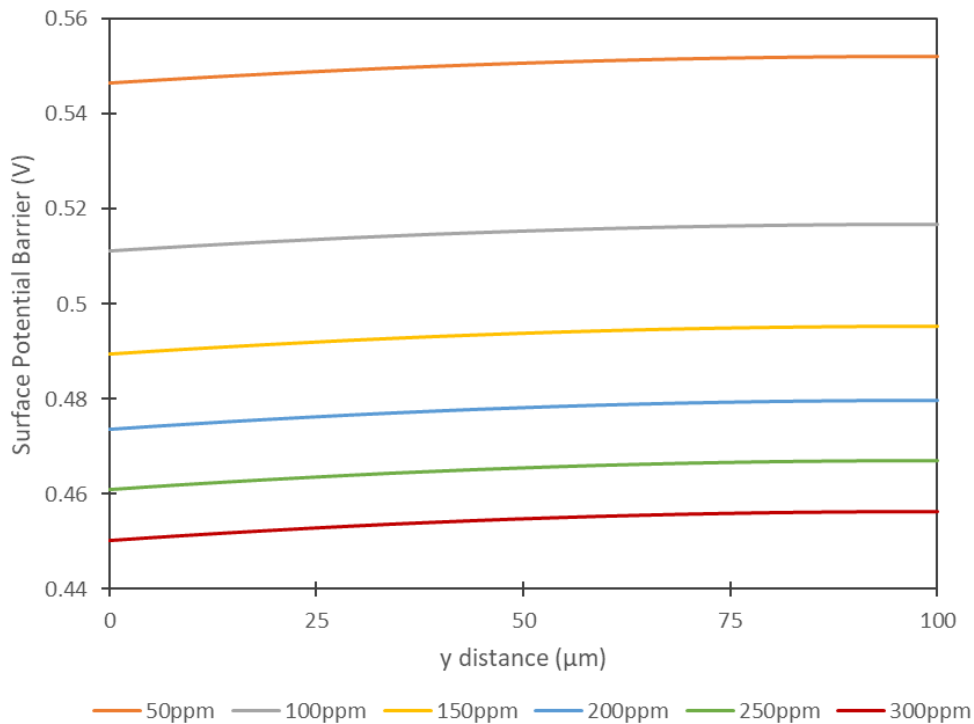


Figure 4-8. Steady-state surface potential barrier in response to different CO inlet concentrations at 600 K, with an inlet velocity of 0.01 m/s

Figure 4-9 shows the sensor sensitivity as a function of CO concentration, where  $R_i$  is the electrical resistance of the sensor in air, and  $R$  is the electrical resistance of the sensor in the presence of CO gas. As the CO concentration increases, the change in resistance becomes more pronounced, which results in a higher value of sensor response. In other words, the response increases because of low resistance values accompanied by increasing target gas concentrations. However, as concentration increases after a certain point, resistance cannot be decreased as in lower concentration regions which results in a plateau in sensor response. This plateau explains the saturation of the sensor response and can be attributed to the occupation of more active sites on the sensor surface by gas molecules at high gas concentrations. However, in high-concentration regions, the sensor responses get closer, and the increase of the response tends to decrease. This is mainly due to the

fact that at a low concentration range, recovery of the ionized oxygen can compete with the consumption of it. As CO concentration increases, ionized oxygen consumption increases, and the recovery effect decreases.

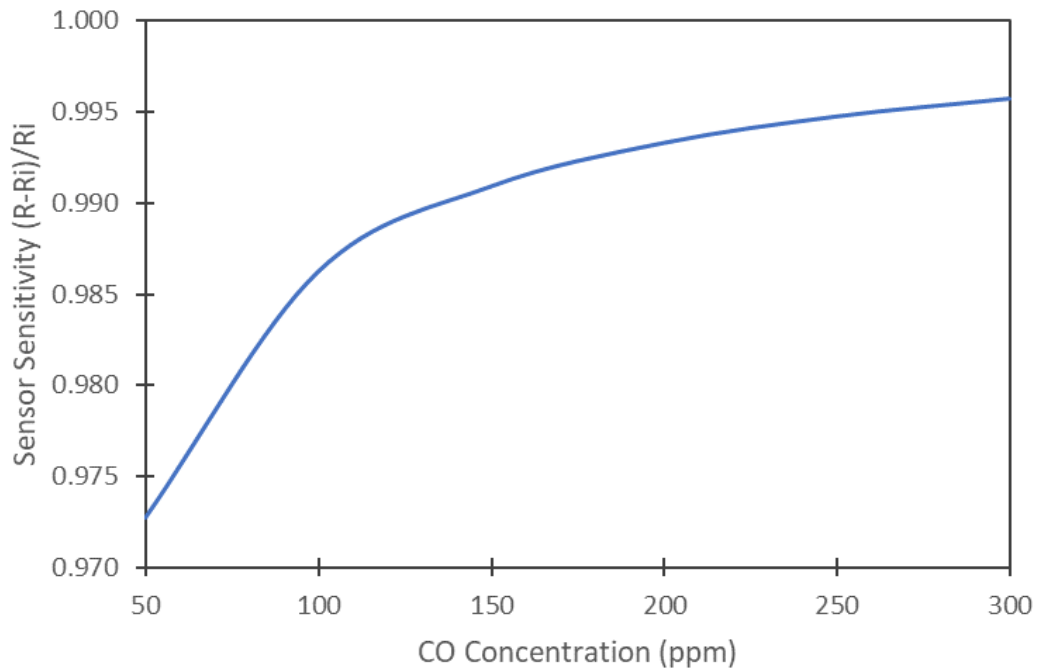


Figure 4-9. Sensor sensitivity in response to different CO inlet concentrations at 600 K, with an inlet velocity of 0.01 m/s

### 4.3 Effect of Inlet Velocity

The effect of fluid flow velocity on the sensor response was investigated for varying flow velocities as 0.005 m/s, 0.01 m/s, 0.03 m/s, 0.05 m/s, and 0.1 m/s. The simulations were conducted with 200 ppm of CO at an operating temperature of 600 Kelvin and an inlet velocity of 0.01 m/s for the 100  $\mu\text{m}$  sensing film. It is found that due to the low permeability of  $\text{SnO}_2$ , convective mass transfer is effective on the surface of the sensing film. In addition, diffusion is the effective mass transfer inside the sensing film.

In the microfluidic system, the characteristic length scale is small, and the velocity of the air-CO mixture introduced from the measurement chamber is typically low. This low velocity corresponds to low Reynolds numbers where inertial forces are much smaller than viscous forces. Reynolds numbers are, therefore, much lower than the critical Reynolds number for the ideal laminar flow of 2000, as seen in Table 4-1. This laminar flow condition leads to highly ordered flow, and turbulent fluctuations are eliminated.

Table 4-1. The gas mixture velocity and corresponding Reynolds number

Velocity (m/s)	Reynolds Number
0.005	0.52
0.01	1.05
0.05	5.25
0.1	10.49

Figure 4-10 shows the flow velocity change along the center longitudinal axis of the measurement chamber starting from the entrance. It is seen that the entrance effect on the flow becomes insignificant before it reaches the sensor surface. It shows that the flow becomes independent of the location inside the chamber around  $x=4000 \mu\text{m}$ , which is well before the first touch with the sensing film,  $x=4500 \mu\text{m}$ .

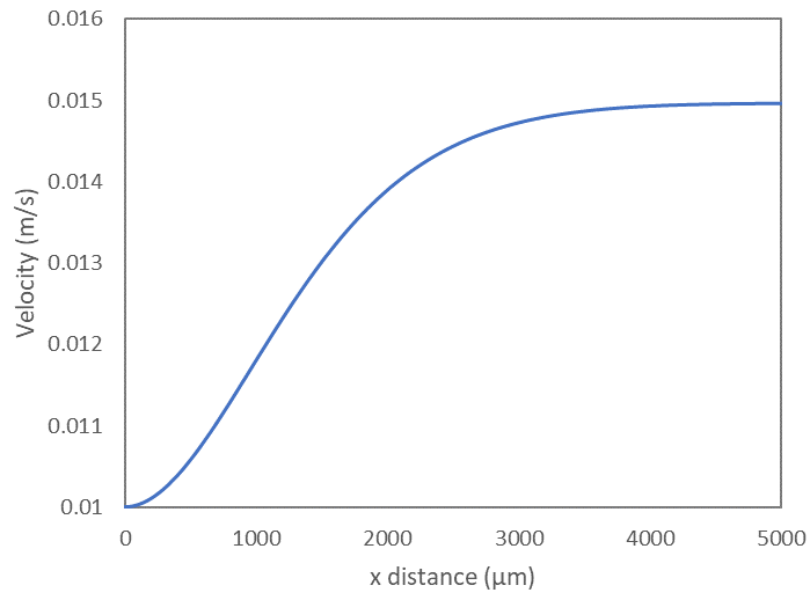
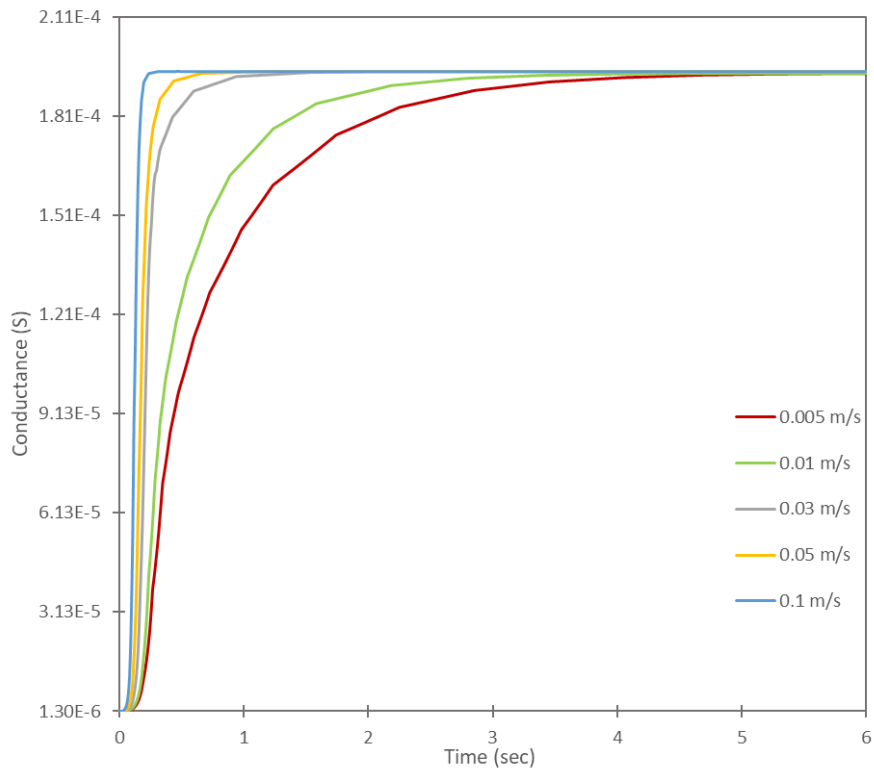
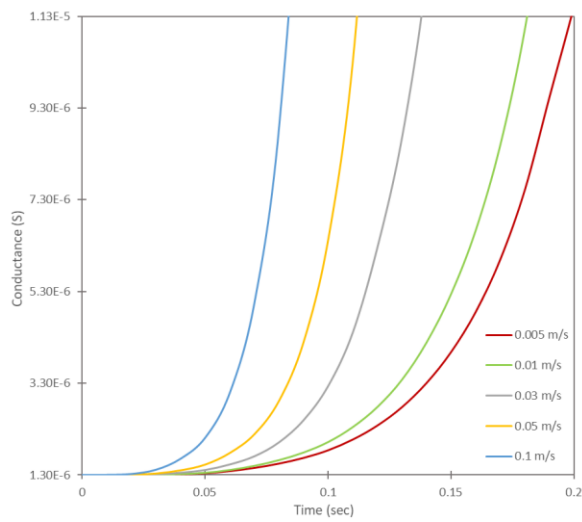


Figure 4-10. Flow velocity change along the center longitudinal axis of the measurement chamber

Figure 4-11a describes the effect of fluid velocity on the surface averaged conductance temporal profile. The x-axis represents time in seconds, and the y-axis corresponds to the surface averaged conductance of the sensor. The lines show the different inlet velocities of the measurement chamber. Increasing velocity contributes to the convective term in the transport equation and enhances the mass transfer rate of the target gas through the sensing surface. Higher velocities improve the arrival time of the fluid to the sensor, as seen in Figure 4-11b. Increasing fluid velocities not only shortened the arrival of the target gas to the sensor surface but also caused steeper sensor response curves. The steeper curve means that the response of the sensor changes more rapidly to changes in the target gas concentration. Furthermore, it is apparent that when the convective mass transfer becomes less pronounced, the rate at which the sensor reaches the steady-state is the slowest.



a)



b)

Figure 4-11. Surface averaged conductance profile in response to different inlet flow velocities for 100  $\mu\text{m}$  thickness sensing film at 600K  
a) whole profile b) zoomed profile to early time points

It is seen that the steady-state surface averaged conductance is the same for all inlet velocities. This is explained by the Peclet number for the measurement chamber. Peclet number is used as a dimensionless number to evaluate the relative importance of convective and diffusive mass transfer in the gas chamber. It is defined as given in Equation 43.

$$Pe = \frac{u \cdot D_h}{D_{CO}} \quad 43$$

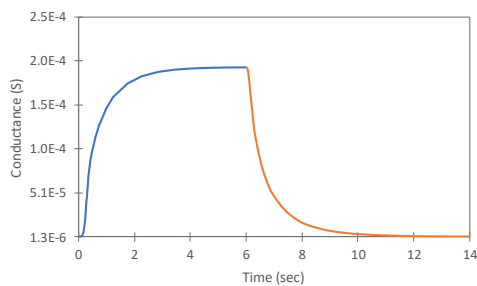
where  $u$ ,  $D_h$ , and  $D_{CO}$  correspond to the fluid velocity, hydraulic diameter, and diffusivity of CO molecules in the chamber. Calculated Peclet numbers corresponding to different inlet velocities for the measurement chamber are represented in Table 4-2.

Table 4-2. Fluid velocities condition and corresponding Peclet number

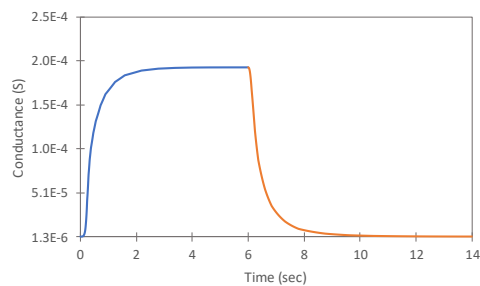
Inlet velocity (m/s)	Peclet number
0.005	0.34
0.01	0.69
0.03	2.07
0.05	3.45
0.1	6.89

Peclet numbers less than unity for 0.005 m/s and 0.01 m/s inlet velocities refer to diffusion-dominated behavior of the mass transfer for the measurement chamber. For the other inlet velocities, Peclet number is greater than unity; however, the contribution of diffusion mass transfer to the overall mass transfer is still significant. Because of diffusion-dominated fluid flow behavior, inlet velocity has no effect on the final surface averaged conductance. This is because of the effective gas access through the sensor surface, which is facilitated by mass transfer through diffusion. If the Peclet number becomes larger because of a lower diffusion coefficient in the

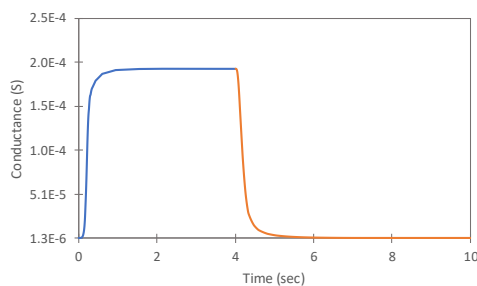
measurement chamber, gas access to the sensor surface is restricted, and the sensitivity of the sensor can be affected. The concentration gradient growth in the measurement chamber is stretched with low diffusivity. The lower diffusion coefficient in the measurement chamber may result from a filter or protective layer that is placed over the sensing film. The sensor may take longer to respond to changes in gas concentration because the gas molecules take longer to diffuse through the filter or protective layer to reach the sensor surface.



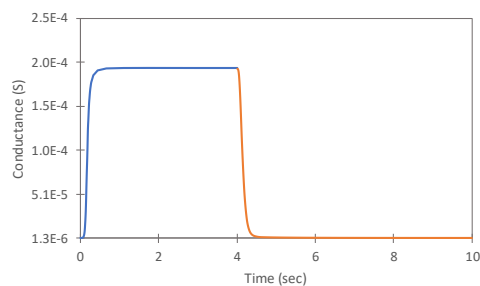
a)



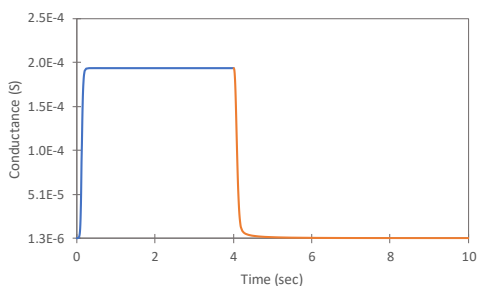
b)



c)



d)



e)

Figure 4-12. Response/recovery timewise profile for varying inlet velocities in response to 200 ppm of CO at 600 K  
 a) 0.005 m/s b) 0.01 m/s c) 0.03 m/s d) 0.05 m/s e) 0.1 m/s

Figure 4-12 shows the response and recovery dynamics of the sensor when exposed to 200 ppm CO and operated at a temperature of 600 Kelvin for different velocities as 0.005 m/s, 0.01 m/s, 0.03 m/s, 0.05 m/s, and 0.1 m/s. The figure displays how conductance changes both during the response to the target gas and the subsequent recovery when the target gas exposure is cut with increasing inlet velocities.

The response time in this research corresponds to the time required for the gas sensor to reach 90% of its saturation resistance in the presence of the target gas, while the recovery time corresponds to the time required to reach 90% of the baseline resistance after the removal of the target gas in excess oxygen environment<sup>95</sup>.

It is obvious that as the fluid velocity increases, steeper response and recovery curves are obtained, indicating both response and recovery time decrease. The reason behind this rapid decrease in response and recovery time is the increase in mass transfer coefficient because of the high velocity. However, as the velocity of the fluid increases, both curves become steeper and further improvement in time is limited. This means the rate of decrease in response and recovery decreases as the velocity increases.

Table 4-3. Fluid inlet velocities and corresponding response/recovery time

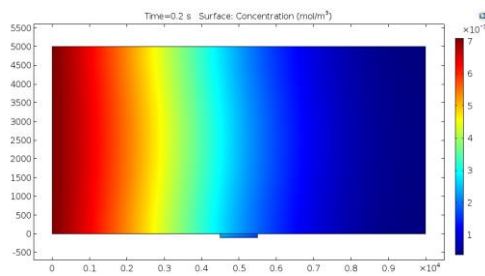
Velocity (m/s)	Response time (sec)	Recovery time (sec)
0.005	1.72	7.04
0.01	1.17	6.25
0.03	0.37	4.33
0.05	0.26	3.72
0.1	0.17	3.58

In Table 4-3, velocity values and corresponding response and recovery time are shown. It is evident that the higher fluid velocities result in a shorter response and recovery time because of the fact that increasing velocity accelerates the convective transport of gas molecules to the sensor surface. Furthermore, the recovery time is greater than the response time. This is due to the fact that initially, there is no CO in the measurement chamber thus concentration gradient is higher when the target gas is introduced to the measurement chamber. However, when the system reaches a steady-state, the presence of CO in the measurement chamber leads lower concentration gradient than the initial state. In addition, there is a time period required to exchange the filled gas with fresh air before the sensor surface recovery. It can be concluded that air with high velocity is preferable for fast recovery times.

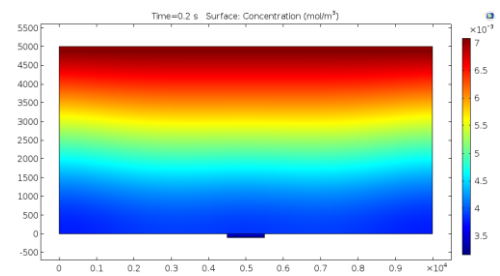
### **4.3.1 Comparison of Horizontal and Vertical Flow Configurations**

In the default configuration of the system discussed in this study, the flow is introduced into the chamber from the left wall. This standard setup is commonly seen in many applications, particularly those encountered in household appliances. However, there is value in exploring alternative configurations, especially when there is specific knowledge about the direction of the inlet velocity. To illustrate this, a second configuration is introduced in which the flow enters the channel from the top wall and proceeds downwards to reach the sensing layer, which is located 5000 micrometers away from the inlet.

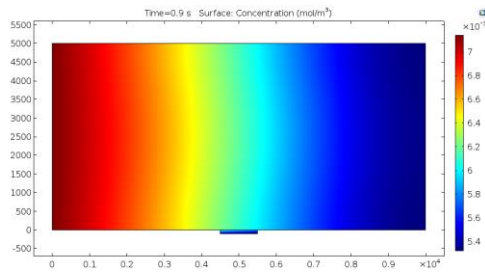
Figure 4-13 shows two different flow configurations through the measurement chamber. Figure 4-13a, Figure 4-13b, and Figure 4-13c represent the aforementioned configuration in which flow is introduced from the left of the measurement chamber, while Figure 4-13d, Figure 4-13e, and Figure 4-13f represent that the flow is introduced from the top of the measurement chamber vertically. Figure 4-13a and Figure 4-13d correspond to the  $t=0.2$  second. The other figures represent  $t=0.9$  second.



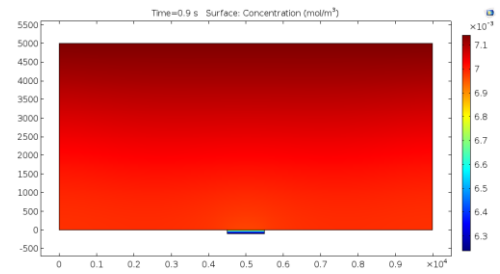
a)



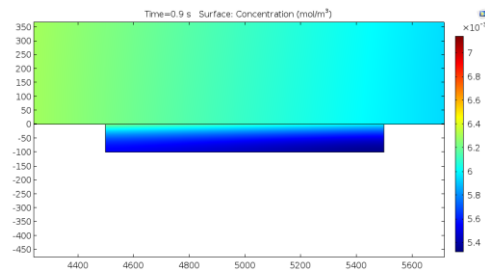
d)



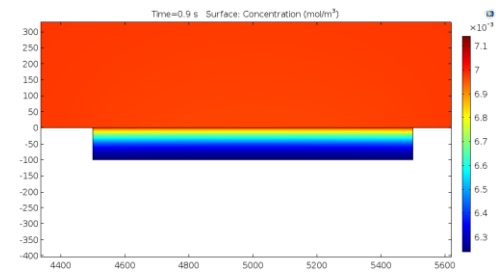
b)



e)



c)



f)

Figure 4-13. Two different flow configurations to the measurement chamber  
a, b, c) Horizontal flow from the left  
d, e, f) Vertical flow from the top

Figure 4-14 shows the surface averaged conductance timewise change for the two configurations. A remarkable feature of vertical flow configuration is that the species transport within the sensing layer is significantly faster compared to the default configuration. This increased transport speed is largely due to the minimal viscous effects of the wall. With the flow directed from the top, the fluid's influence from the wall's viscous forces is reduced. This is because the fluid's velocity profile does not encounter any no-slip boundary prior to reaching the sensing layer, thereby minimizing the viscous shear stress that could otherwise impede the transport of species.

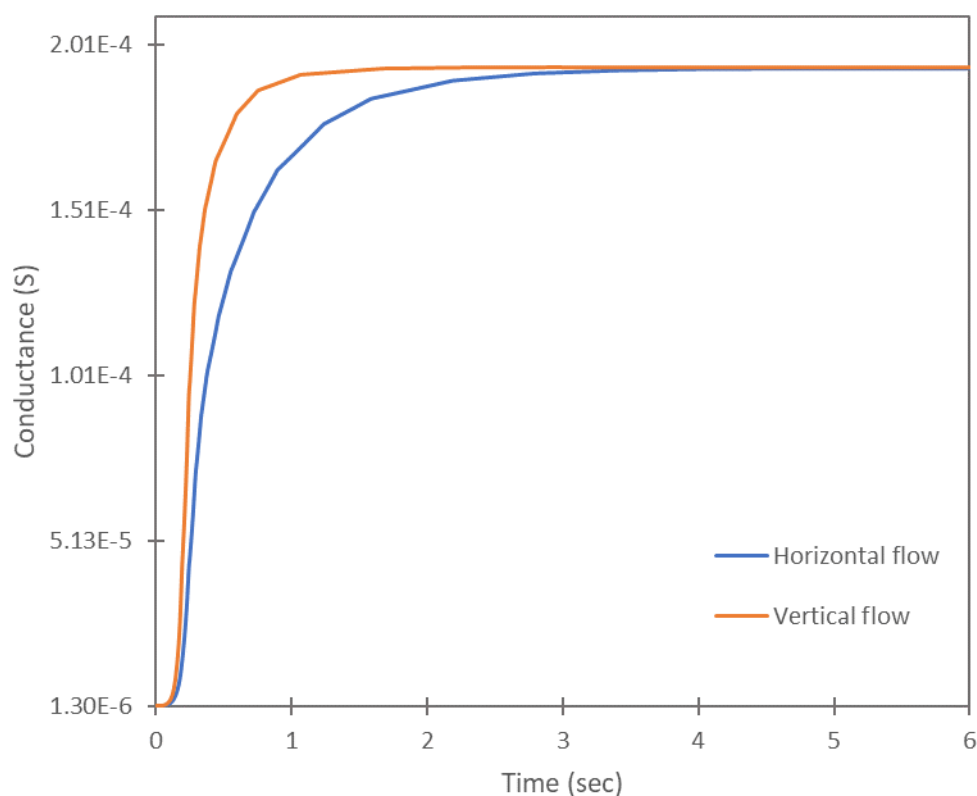


Figure 4-14. Surface averaged conductance timewise profile for horizontal and vertical flow configurations in response to 200 ppm of CO at 600 K, with an inlet velocity of 0.01 m/s

In contrast, in the default configuration, where the flow enters from the left wall, the fluid is in constant contact with the wall, leading to a more prominent presence of viscous effects. This results in slower species transport due to the increased resistance from the shear stress.

Additionally, the directionality of the flow also significantly impacts the concentration distribution within the sensing layer. In the default configuration, the concentration distribution along the centerline of the sensing layer is not homogeneous, likely due to the influence of wall effects and the development of the velocity profile. However, when the flow originates from the top wall, the sensing layer exhibits a uniform concentration distribution from left to right. This uniformity is likely due to the reduction in viscous effects, leading to less disturbance in the flow and, thus, more evenly distributed species concentration.

In conclusion, the top-down flow configuration provides a more efficient and faster species transport within the sensing layer by minimizing the impact of wall viscous effects. This, coupled with the uniform concentration distribution, could represent a critical discovery for optimizing sensor placement within industrial chambers.

#### 4.4 Effect of Temperature

The effect of temperature on the sensor response, the response/recovery characteristics, and the sensitivity of the sensor were examined. The temperature range investigated varied from 450 K to 800 K, which corresponds to the operating temperature range of the sensors, with 50 K intervals. The study was conducted for 100  $\mu\text{m}$  sensing film exposing 200 ppm of CO, with an inlet velocity of 0.01 m/s.

The operating temperature has a significant effect on the gas sensing process. Mass transfer in the measurement chamber and porous medium and the reaction kinetics are temperature dependent and effective for the sensor response. Knudsen diffusion coefficient is proportional to temperature as  $T^{1/2}$ , and the reaction rate changes exponentially with temperature based on Arrhenius expression, as seen in Equation 45.

$$D_k = \frac{4r}{3} \sqrt{\frac{2RT}{\pi M}} \quad 44$$

$$k = k_0 \exp\left(-\frac{E}{RT}\right) \quad 45$$

As explained before, the equation describing the temperature dependency of the CO diffusion in the measurement chamber was also obtained by fitting a curve to data points corresponding to specific temperatures, and the resulting fitted curve was used to model the relationship between temperature and diffusion.

In addition, the conductance of the sensor was modeled dependent on temperature exponentially, as seen in Equation 46. This exponential relation indicates that as the temperature increases, the final conductance of the sensor rises exponentially.

$$G(T, V_s) = G_0 \exp\left(\frac{-q^2 N_s^2}{2\epsilon_0 \epsilon_r N_d k_B T}\right)$$

Depending on the oxygen concentration and the operation temperature, adsorbed oxygen molecules maintain a dynamic equilibrium within the system. The ionized oxygen density at initial steady-state conditions was determined mainly by the rates of chemisorption and ionization reactions for each operating temperature. These initial values of ionized oxygen density correspond to different initial conductance values for the sensor, as seen in Table 4-4. The increase in operating temperature leads to the higher thermal energy of the gas molecules, which means more oxygen molecules have enough energy to be ionized. In addition, higher thermal energy results in a narrower energy band gap, so higher conductance is achieved.

Table 4-4. Initial values of ionized oxygen density and initial conductance

Temperature (K)	Initial Ionized Oxygen Density (1/m <sup>2</sup> ) (10 <sup>-16</sup> )	Initial Conductance (S) (10 <sup>6</sup> )
450	4.68	0.14
500	4.80	0.35
550	4.92	0.71
600	5.03	1.30
650	5.14	2.16
700	5.25	3.36
750	5.36	4.93
800	5.46	6.91

Figure 4-15 illustrates steady-state CO concentration change over the vertical direction of the sensing film. The x-axis corresponds to the central vertical cutline of the sensor. The  $x=0$  corresponds to the sensor surface, while  $x=100\ \mu\text{m}$  refers to the impermeable boundary. At steady-state conditions, CO concentration at the sensor surface reaches  $0.00714\ \text{mol}/\text{m}^3$  for all temperatures. However, the distribution of CO changes as temperature increases.

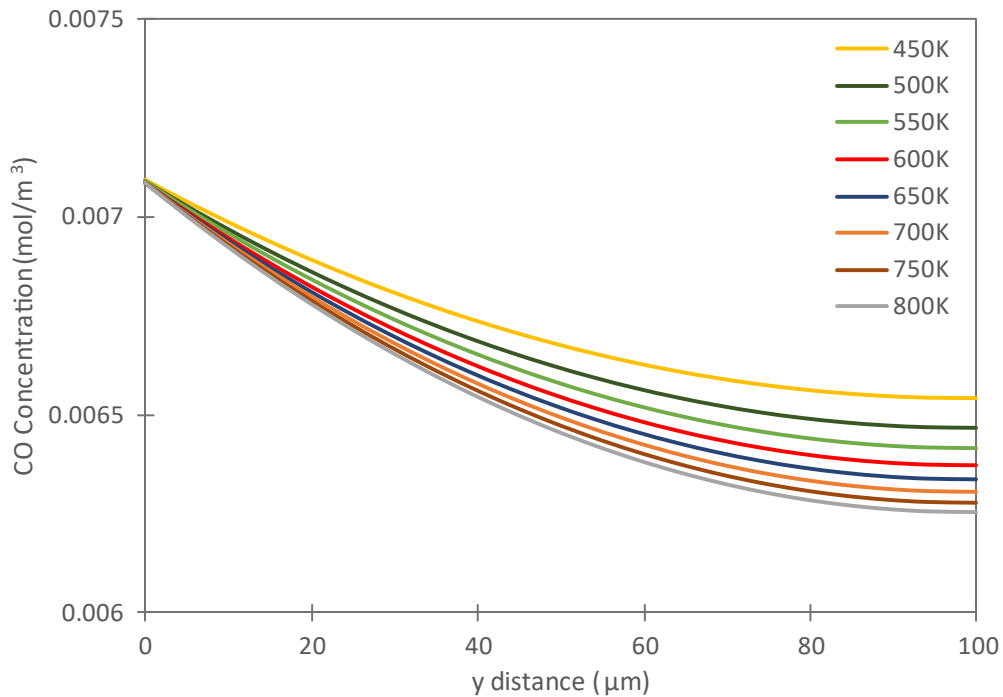
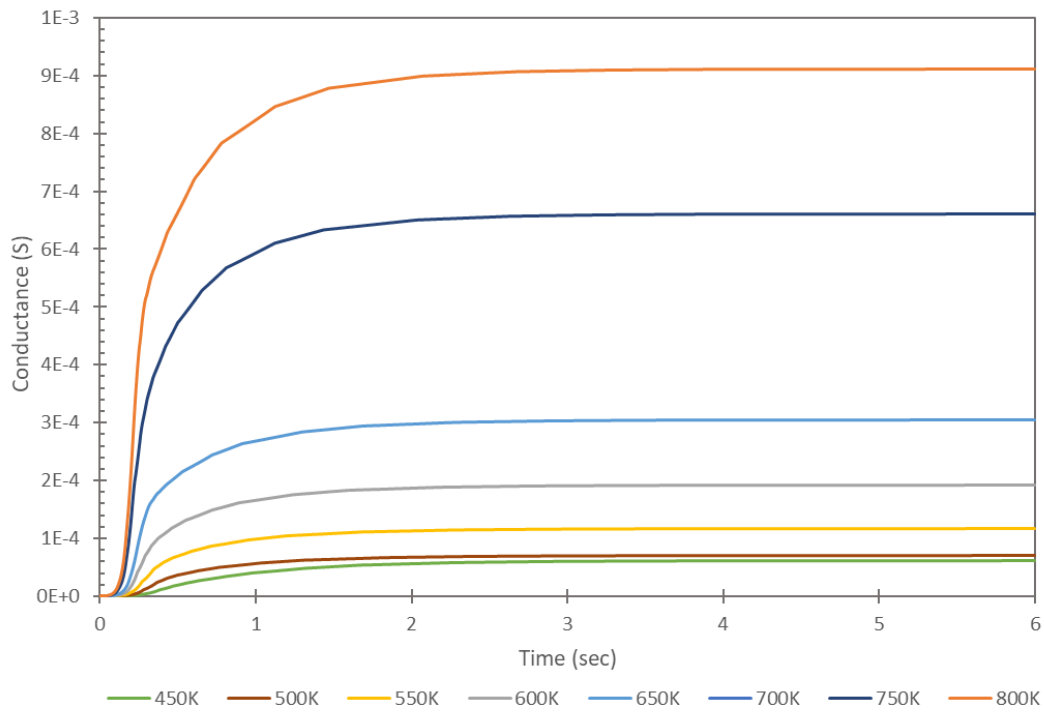


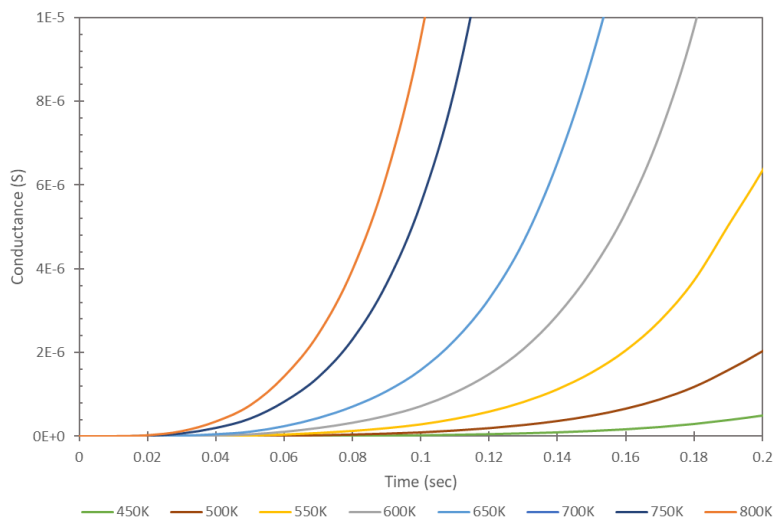
Figure 4-15. Steady-state CO concentration spatial profile for varying operating temperatures in response to 200 ppm of CO, with an inlet velocity of 0.01 m/s

It is observed that CO concentration is higher at the deeper regions of the sensor for lower operating temperatures. Temperature affects both diffusion rate and reaction rate. The temperature influence on the competing effect of reaction and diffusion

determines the overall CO distribution. As stated before, temperature affects the reaction rate exponentially as  $T^{-1}$  while it affects the diffusion rate as  $T^{1/2}$ . The diffusion rate varies between  $6.96 \times 10^{-8}$  and  $9.26 \times 10^{-8}$  from the lowest temperature to the highest temperature, respectively. Lower CO concentration at the deeper regions of the sensing film with increasing temperature means that reaction becomes dominant over diffusion, and CO molecules are consumed easily before reaching the bottom surface even if their diffusion becomes faster with the increase in temperature. A higher reaction rate on the surface penetrates CO gas diffusion to the deeper regions, which makes the gas penetration highly temperature dependent.



a)



b)

Figure 4-16. Absolute surface averaged conductance profile for varying temperatures in response to 200 ppm of CO, with an inlet velocity of 0.01 m/s  
a) whole profile b) zoomed profile to early time points

Figure 4-16a represents absolute surface averaged conductance change with time for varying temperatures. The absolute surface averaged conductance is used to eliminate varying baseline conductance for all temperatures. The x-axis represents time in seconds, and the lines correspond to different operating temperatures. The y-axis represents the difference between the measured conductance and initial conductance in order to show the absolute change in the sensor response. It is evident that the absolute conductance increases as temperature increases. This is due to the fact that increased thermal energy allows more electrons to cross the energy gap and release to the conduction band.

This can be explained theoretically by the relationship between band gap energy and temperature which is described by Varshni's empirical equation<sup>96</sup>.

$$E_g(T) = E_g(0) - \frac{\alpha T^2}{T + \beta} \quad 47$$

$$E_g'(T) = -\frac{\alpha T(T + 2\beta)}{(T + \beta)^2} \quad 48$$

where  $E_g(0)$ ,  $\alpha$  and  $\beta$  are material constants while  $E_g$ , and  $T$  correspond to the band energy gap and temperature, respectively. As temperature increases, the band gap energy decreases because of the fact that increasing thermal energy increases electron mobility based on the electron mobility temperature dependency that is characterized by  $T^{-3/2}$ . Thus, more electrons move through the conduction band and increasing the electrical conductivity of the semiconductor material. The first derivative of Equation 47 results in Equation 48, which shows how the band energy gap change with increasing temperature. The equation shows that the band energy gap decreases as temperature rises. When the ionized oxygen density is higher, there are more charge carriers available for the electrical current. As a result, higher ionized oxygen density leads to higher conductance as temperature increases. In addition, Figure 4-16b depicts the zoomed plot to earlier time points. As the temperature increases, the sensor begins to provide a response at an earlier point in

time. Increasing temperature improves both reaction rate and mass transfer rate, as stated before. CO molecules more readily reach the sensor surface, reacts, and diffuse through the sensor as temperature increases.

Figure 4-17 represents sensor sensitivity changes in time with varying operating temperatures. The x-axis corresponds to time, the y-axis represents the sensor response, and the lines correspond to different operating temperatures. The sensor sensitivity is defined as the ratio of the difference between the measured conductance and the initial conductance to the initial conductance, which represents the relative change of sensor response. It is observed that as operating temperature increases, sensor sensitivity tends to decrease, as seen in Table 4-5. The maximum sensitivity was observed for the 450 K.

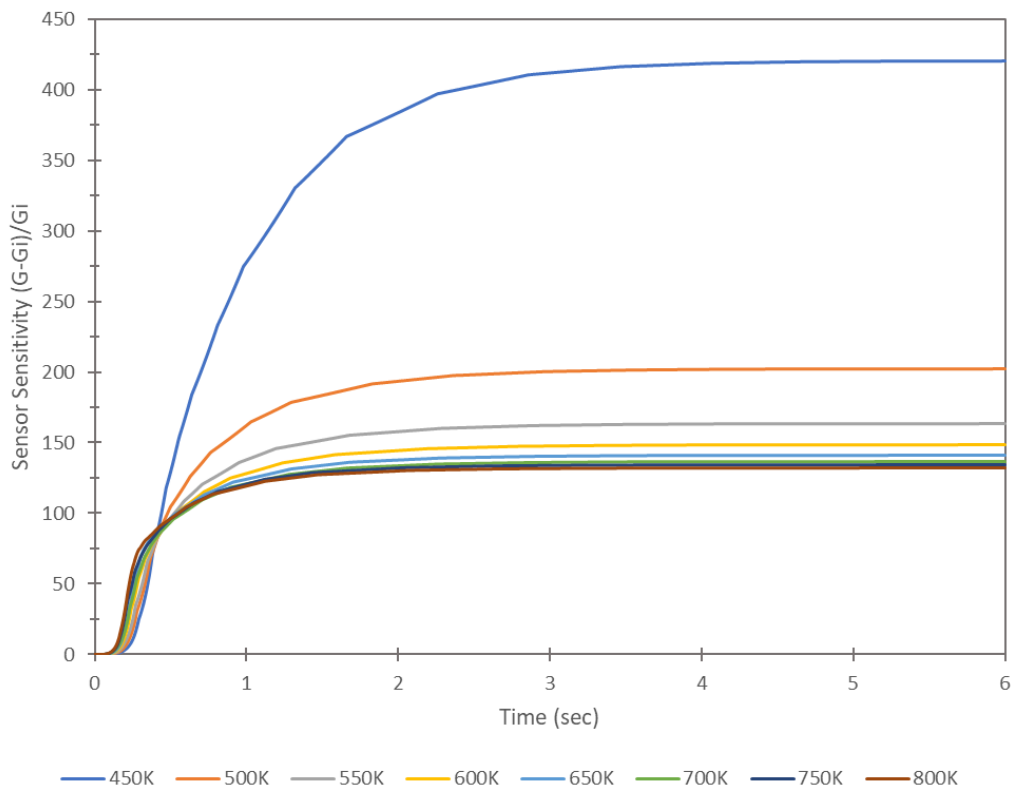


Figure 4-17. Sensor sensitivity for different operating temperatures in response to 200 ppm of CO, with an inlet velocity of 0.01 m/s

Table 4-5. Different operating temperatures and corresponding initial, steady-state, and normalized conductance values

Temperature (K)	Initial	Steady-state	Sensor Sensitivity
	Conductance (S) (10 <sup>6</sup> )	Conductance (S) (10 <sup>4</sup> )	
450	0.14	0.61	421
500	0.35	0.71	202
550	0.71	1.17	163
600	1.30	1.94	149
650	2.16	3.08	141
700	3.36	4.64	137
750	4.93	6.66	134
800	6.91	9.18	132

As the temperature increases further, the sensor sensitivity exhibits a gradual reduction and converges with each other at higher temperatures. It can be said that this converges starts at 600 K. Investigating Figure 4-18 reveals the reason for this.

Overall, the sensor response is determined by the ionized oxygen density change of the sensor. The differential equation of the ionized oxygen density depends on the comparative effects of consumption and recovery of ionized oxygens. In Figure 4-18, the difference between the rate of recovery of the ionized oxygen and the rate of the oxidation reaction is presented. This difference curve explains that the consumption rate of the ionized oxygen is always greater than the net recovery. After 600 K, this difference curve becomes almost flat. Therefore, the sensor sensitivity tends to remain unresponsive to temperature changes. This stems from the fact that the change in sensitivity is mainly attributed to the gradient in the difference between these two kinetics that governs the sensing mechanism.

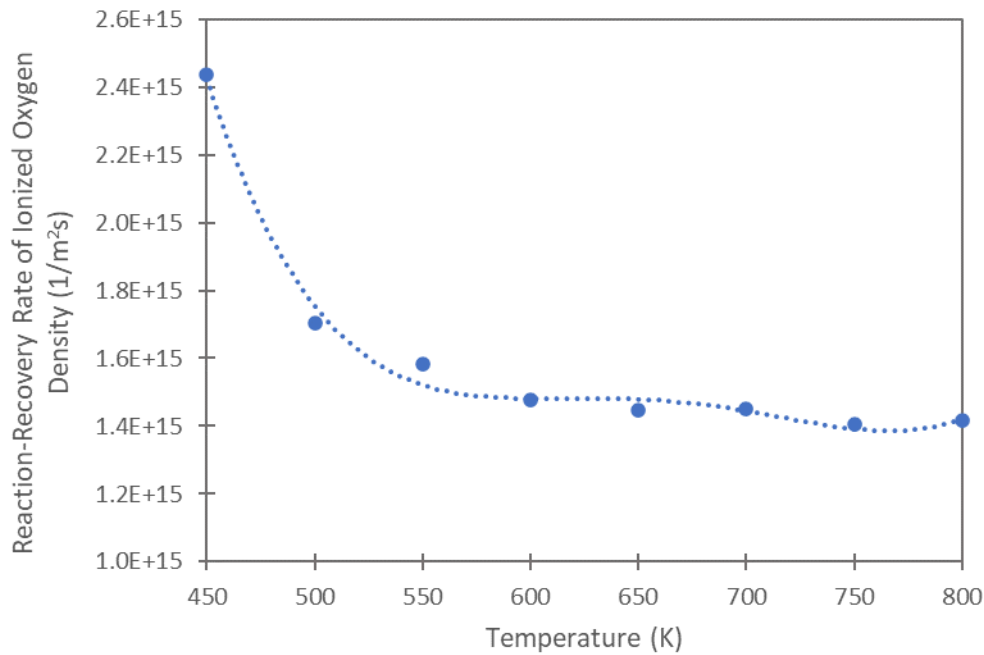


Figure 4-18. Difference between reaction rate and recovery rate of ionized oxygen density for different operating temperatures

This behavior of the curve could be explained mainly by the activation energy of the ionization reaction. At low temperatures, the high activation energy of the ionization makes it difficult to recover consumed ionized oxygen molecules, making the difference greater. As temperature increases, ionized oxygen recovery increases and competes with the oxidation reaction, which results in low difference values. However, overall, the effect of temperature on the oxidation reaction predominates, leading to a decrease in the density of ionized oxygen, even in the presence of simultaneous ionization. The reason for the flatness of the curve after 600 K is attributed to the fact that the increase in oxidation reaction is challenged by the recovery process. As a result, ionized oxygen density cannot change as in the case of 450 K.

Another reason for the sensitivity decrease is explained by the gas depletion layer caused by reaction-dominated behavior. As temperature rises, both diffusion of CO and the reaction of ionized oxygen with CO molecule increases. However, the reaction rate dominates the diffusion rate, which results in the reaction taking place

mostly external surface of the sensing layer. This limited reaction surface depletes CO molecules before it transported along the sensing film, thus preventing any significant change in electrical conductance.

Figure 4-19 represents response and recovery temporal profiles for different temperatures. The system is switched to the recovery profile at  $t=6\text{sec}$ . The response profile corresponds to the conductance change over time as CO gas introduction to the measurement chamber until the sensor reaches a steady-state response output. The recovery profile refers to returning to the initial state of the sensor after the CO gas supply is stopped and excess air continues to flow. The diffusion rate of the CO molecules both in the measurement chamber and in the sensing film increases as the temperature rises. Furthermore, based on the Arrhenius equation, as the temperature increases, the exponential term in the reaction equation becomes larger, leading to a higher reaction rate constant. The combined effect of reaction rate and diffusion leads shorter response time for higher temperatures. The same trend is valid for the recovery phase because of the fact that higher kinetic energy for gas molecules leads to faster diffusion through the measurement chamber.

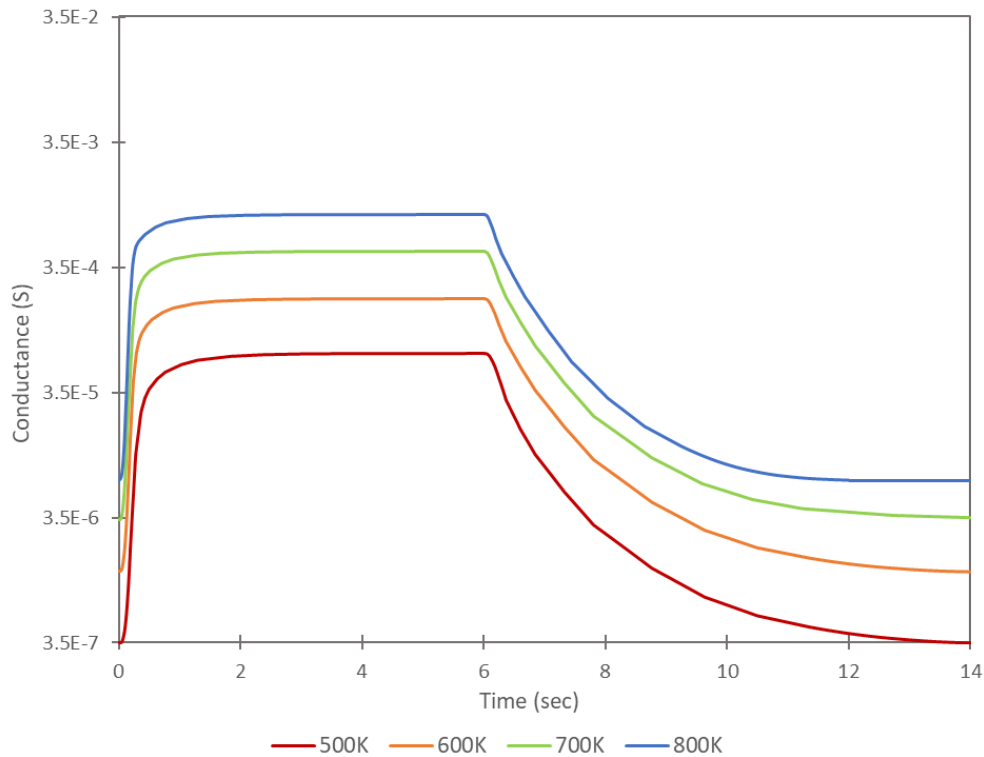


Figure 4-19. Response/recovery profiles for different operating temperatures in response to 200 ppm of CO, with an inlet velocity of 0.01 m/s

Table 4-6 displays response and recovery times for operating temperatures 500 K, 600 K, 700 K, and 800 K. Once the target gas begins to escape from the sensing film, the ionized oxygen molecules are regenerated to the initial state. The higher activation energy of the ionization reaction than the reverse ionization, and the oxidation makes the recovery time longer than the response time. In addition, in recovery region the recovery dominates over the oxidation reaction because of a decrease in CO concentration. At the beginning of the recovery phase, the measurement chamber is filled with CO at a concentration of  $0.00714 \text{ mol/m}^3$ . The lower concentration gradient because of the target gas-filled measurement chamber results in longer durations compared to the response time. This is because of the slow diminishing effect of the oxidation reaction as explained in Figure 4-20.

Table 4-6. Different temperatures and corresponding response/recovery times

Temperature(K)	Response time(sec)	Recovery time(sec)
500	1.46	6.57
600	1.17	6.25
700	1.08	5.16
800	0.98	4.75

Figure 4-20 depicts ionized oxygen density profile in response and recovery regions. Ionized oxygen reaches a steady-state in the response region earlier than the recovery region. This can be attributed to the fact that CO molecules require a longer time to leave the sensing film. The term in the differential equation of the ionized oxygen that explains the oxidation reaction,  $-k_{30} \exp\left(\frac{-E_3}{RT}\right) N_S c_{CO}$ , continues to consume ionized oxygen molecules as long as the CO molecules remain within the sensing film.

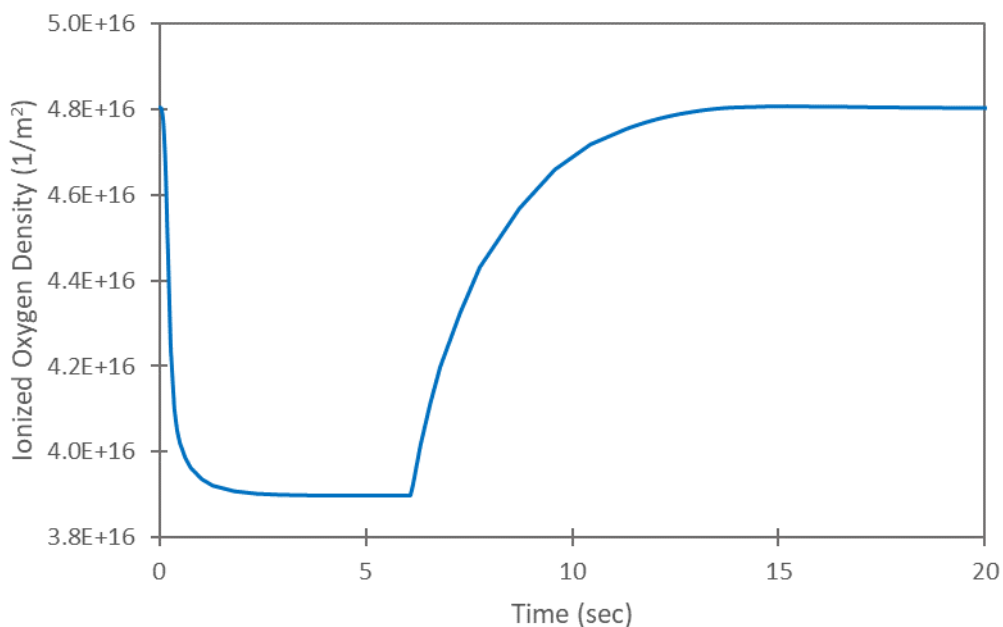


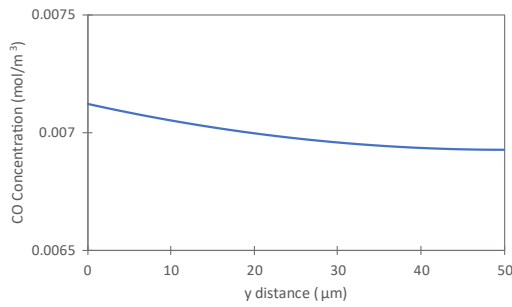
Figure 4-20. Surface averaged CO and ionized oxygen density response/recovery profiles in response to 200 ppm of CO at 500 K, with an inlet velocity of 0.01 m/s

## 4.5 Effect of Thickness

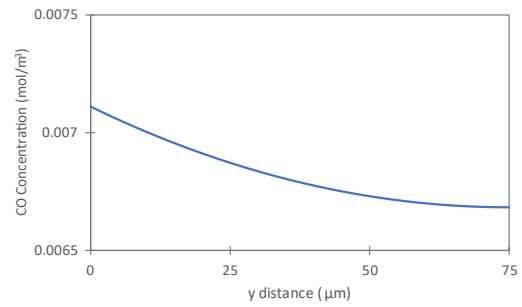
The thickness effect on the target gas distribution in the sensing film, sensor response, and sensitivity was analyzed for 50  $\mu\text{m}$ , 75  $\mu\text{m}$ , 100  $\mu\text{m}$ , 125  $\mu\text{m}$  and 150  $\mu\text{m}$  thickness sensing film exposing 200 ppm of CO with an inlet velocity of 0.01 m/s and operating at 600 Kelvin. The density of ionized oxygen is set to the value corresponding to 600 Kelvin for all different thicknesses.

The expectation for ideal sensing is that gas molecules should diffuse throughout the sensing film and should interact with as many ionized oxygen as possible in order to release more free electrons to the conduction band. This would lead to a greater change in conductance, thus, higher sensitivity. However, as thickness increases or decreases, the competing effect of diffusion and reaction determines the overall response of the sensor.

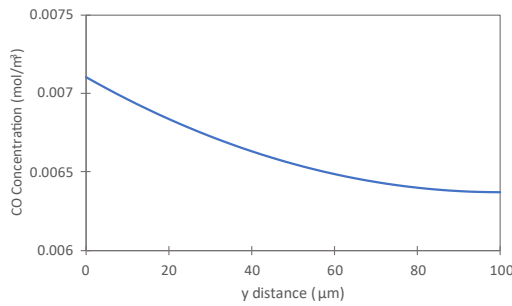
Figure 4-21 represents CO concentration spatial profile at steady-state for different thicknesses. For all cases,  $x=0$  corresponds to the sensor surface, while the other side corresponds to the bottom impermeable surface of the sensor. The sensor surface reaches 0.00714 mol/m<sup>3</sup> CO concentration for all thicknesses. However, CO distribution through the sensing layer differs for sensors with different thicknesses. It is seen that CO concentration is more uniform for the 50  $\mu\text{m}$  case in Figure 4-21a. This uniformity tends to decrease as the thickness of the sensing film increases. The maximum CO concentration difference between the surface and the impermeable surface is observed for the 150  $\mu\text{m}$  in Figure 4-21e. The effects of reaction and diffusion through the reactive porous medium determine spatial distribution. In the thinner case, CO molecules can more easily access the deeper regions of the film because of the shorter diffusion path. However, for thicker films the distribution of CO molecules to the deeper regions becomes difficult because of the simultaneous consumption of CO molecules at the sensor surface. The reaction limits the supply of CO to the deeper part of the sensing film, thus influencing both the transient profile and steady-state sensor response.



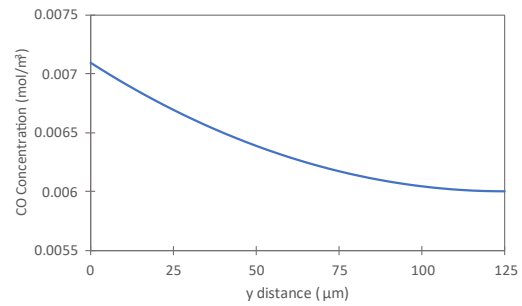
a)



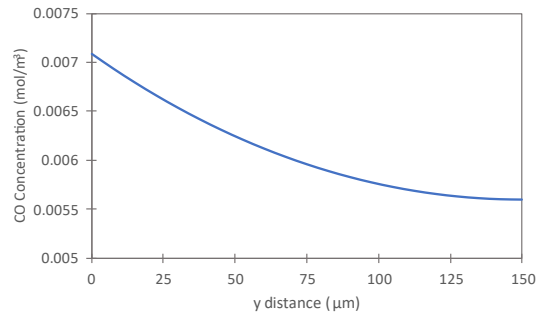
b)



c)



d)



e)

Figure 4-21. Steady-state CO concentration spatial profiles for varying thicknesses in response to 200 ppm of CO at 600 K, an inlet velocity of 0.01 m/s  
a) 50 μm b) 75 μm c) 100 μm d) 125 μm e) 150 μm

In Figure 4-22, surface potential barrier along y direction inside the sensor for different thicknesses is illustrated. The x-axis corresponds to the dimensionless y distance between the sensor surface ( $y=0$ ) and the bottom boundary.

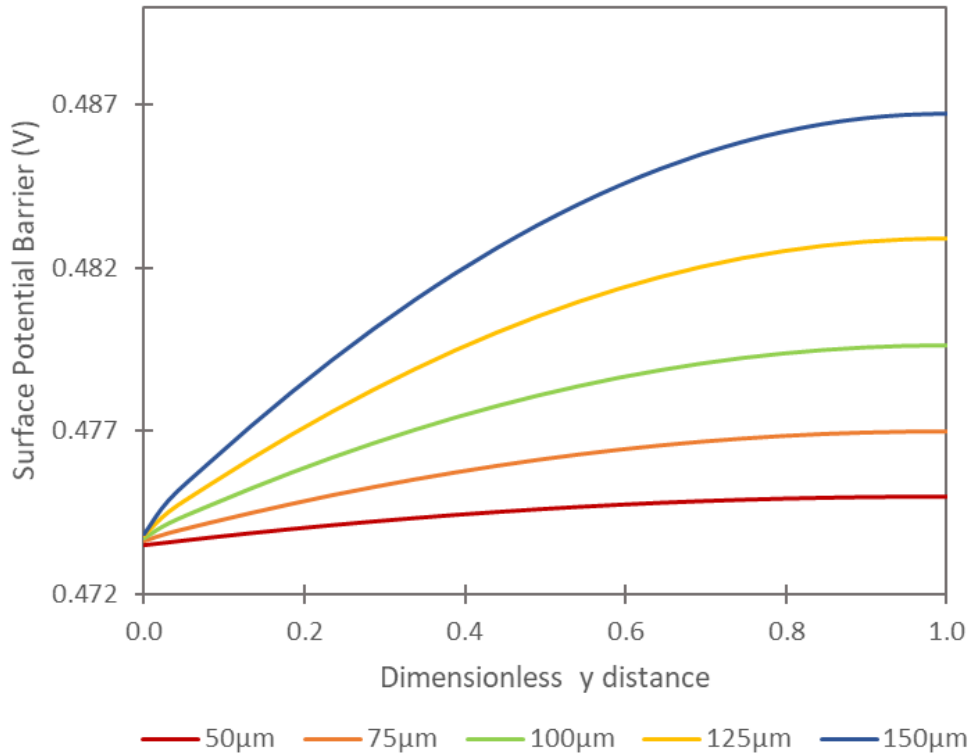


Figure 4-22. Steady-state surface potential barrier spatial distribution for varying thicknesses in response to 200 ppm of CO at 600 K, with an inlet velocity of 0.01 m/s

It is seen that the surface potential barrier is highest for the thickest sensor, which is 150 µm. The trend shows that as the thickness becomes smaller, the difference in the surface potential barrier between the surface and the bottom of the sensor decreases. As the sensor becomes thicker, the depletion of CO gas primarily occurs at the bottom of the sensing film, and the consumption of ionized oxygen in the deeper regions of the sensing film decreases. The surface potential barrier is directly proportional to the square of the ionized oxygen density. Thus, the surface potential

barrier is the representation of the distribution of ionized oxygen species within the sensing layer. In the deeper regions of thicker films, there is a higher amount of ionized oxygen compared to thinner films. This greater ionized oxygen density means unreacted ionized oxygen molecules hence less electron is released to the conduction band. Therefore, the surface potential barrier in the bottom layer of the sensor cannot be decreased further in thicker films. Figure 4-23 represents the conductance temporal profile for sensing films that are 50  $\mu\text{m}$ , 75  $\mu\text{m}$ , 100  $\mu\text{m}$ , 125  $\mu\text{m}$ , and 150  $\mu\text{m}$ . It illustrates how conductance changes over time and equilibrium conductance values for different thicknesses.

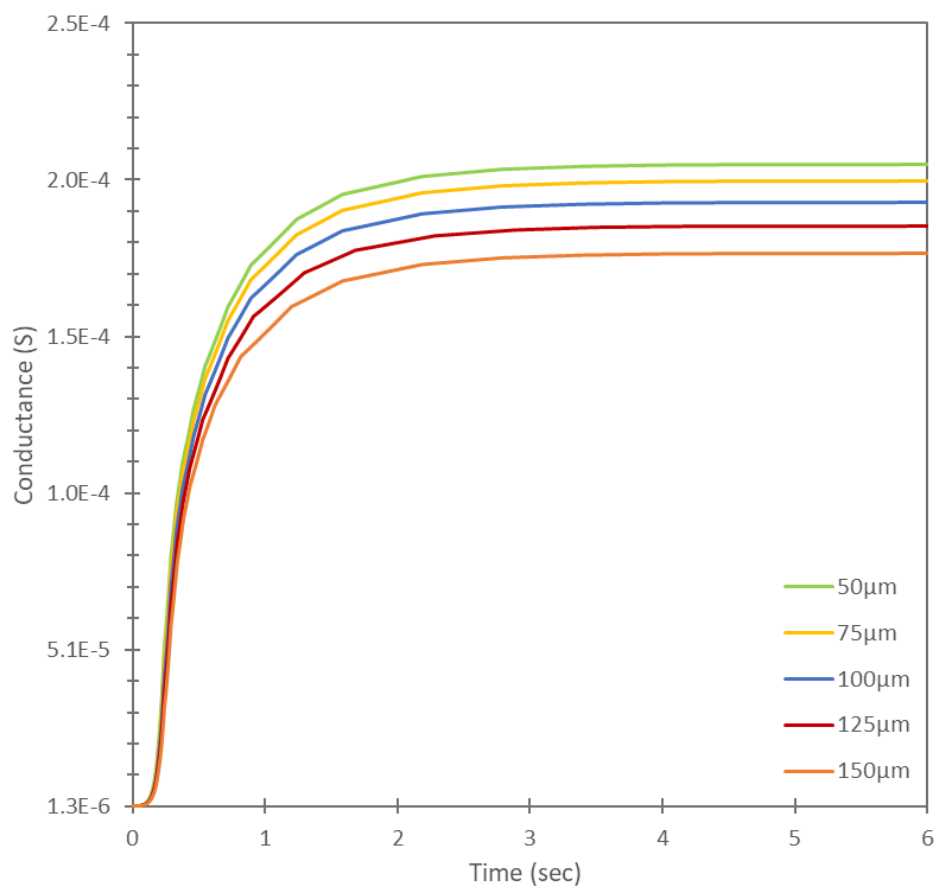


Figure 4-23. Surface averaged conductance timewise profile for varying thicknesses in response to 200 ppm of CO at 600 K, with an inlet velocity of 0.01 m/s

The initial conductance value is the same for all cases and corresponds to the density at 600 Kelvin. The thinnest sensor, which is 50  $\mu\text{m}$ , shows the highest conductance value compared to others. The trend depicts that as the thickness increases, conductance decreases for the sensor. The higher conductance means that more ionized oxygen reacts with the reducing gas and releases electrons to the conduction band. Despite having the same amount of inlet CO concentration, lower conductance explains the diffusion-limited behavior of the sensing film. Unaffected regions of the sensor limit surface reaction; therefore, lower conductance is achieved.

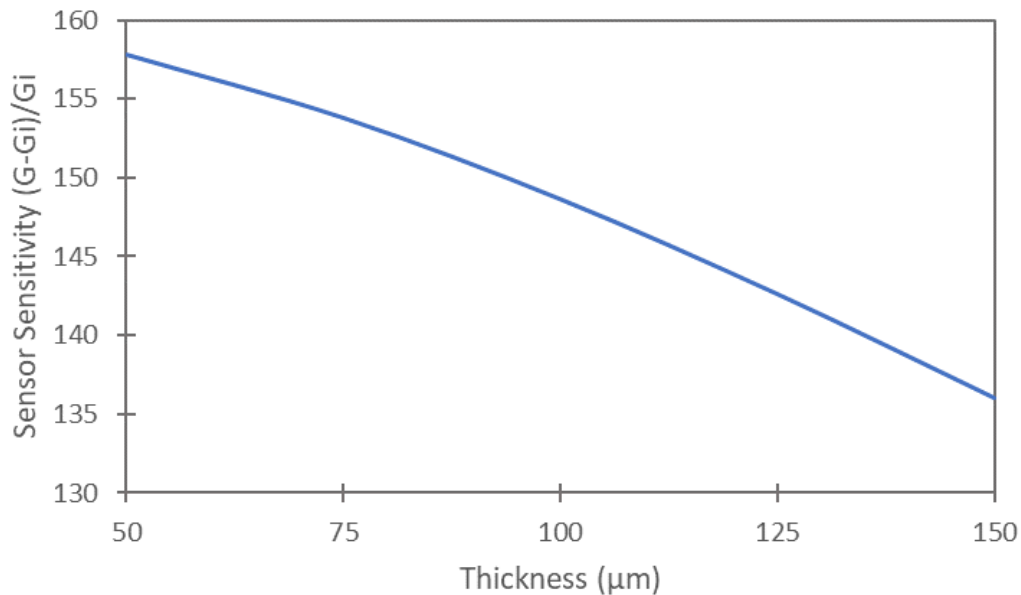


Figure 4-24. Sensor sensitivity with varying thicknesses in response to 200 ppm of CO at 600 K, with an inlet velocity of 0.01 m/s

The sensitivity of the sensor decreases as the thickness of the sensing film increases as seen in Figure 4-24. This can be explained by the simultaneous consumption and supply of the target gas within the sensing film. Inside the sensor, CO is consumed with the oxidation reaction with ionized oxygen molecules. At the same time, the

supply of CO molecules continues through the sensor from the measurement chamber. As the sensing film becomes thicker, CO access to the deeper regions is limited by gas depletion effects. The gas depletion effect refers to CO gas consumption before it can penetrate into the inner layers of the sensing film. For a thin sensing film, CO gas penetrates more efficiently to the deeper regions of the sensor, which causes the reaction to take place throughout the sensing film. As a result, resistance cannot be decreased further for the thicker films, and sensitivity decreases. It can be concluded that a thinner sensing film is preferable as long as the deposition technique allows.

#### 4.6 Effect of Porosity

The influence of porosity on the ionized oxygen density, sensor response, and sensitivity of the metal oxide gas sensor was investigated for the sensing film that is 100  $\mu\text{m}$  and operated under a fluid velocity of 0.01 m/s, with an inlet CO concentration of 200 ppm and an operating temperature of 600 K. It is expected that the porosity of the sensing film significantly influences the penetration of target gas molecules through the sensor.

Figure 4-25 represents steady-state ionized oxygen density spatial distribution along the center vertical cutline of the sensor for different porosities, including 0.1, 0.2, 0.3, 0.4, and 0.5. The x-axis corresponds to the vertical distance where  $x=0$  is the sensor surface, while  $x=100 \mu\text{m}$  is the bottom of the sensor.  $\varepsilon=0.5$  has the highest uniformity along the vertical distance. The distribution tends to become nonuniform as the porosity is reduced. This is due to the fact that porosity enhances the effective diffusion coefficient based on Equation 49.

$$D_{k,eff} = \frac{\varepsilon}{\tau} \frac{4r}{3} \sqrt{\frac{2RT}{\pi M}} \quad 49$$

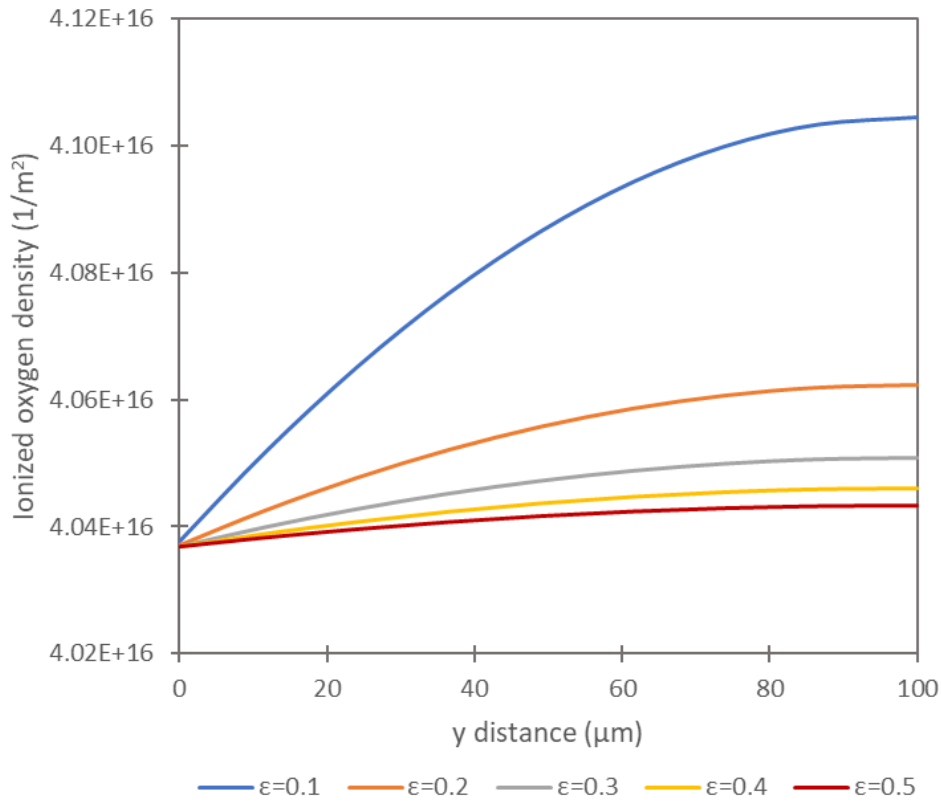


Figure 4-25. Steady-state ionized oxygen density spatial distribution for different porosities of the sensing film in response to 200 ppm of CO at 600 K, with an inlet velocity of 0.01 m/s

The diffusion coefficient range is between  $2.48 \times 10^{-8}$  and  $3.18 \times 10^{-7}$  for the lowest and highest porosities, respectively. When the effective diffusion coefficient is higher, carbon monoxide molecules diffuse more easily through the sensing film because higher porosity provides more channels for gas diffusion. This results in a greater distribution of CO through the film. This increased diffusion leads to higher competition between the diffusion process with the oxidation reaction. Hence, the reaction between ionized oxygen and CO molecules extends through the deeper regions. The observation that  $\epsilon=0.1$  leads to the highest ionized oxygen density in the impermeable boundary of the sensor is directly related to the depletion of carbon monoxide gas in deeper regions.

Figure 4-26 displays time-dependent surface averaged conductance profile for different porosities, including 0.1, 0.2, 0.3, 0.4, and 0.5. The figure illustrates that the final conductance increases as porosity increases. In addition, it is seen that the magnitude of the conductance increase is more pronounced with lower porosities, whereas the increase becomes less significant as the porosity increases. The limited depth of gas penetration tends to restrict the gas sensing primarily to the exterior regions of the sensing layer. As a result, the deeper regions of the layer remain mostly unresponsive or unaffected by the presence of the gas being analyzed, which results in low conductance.

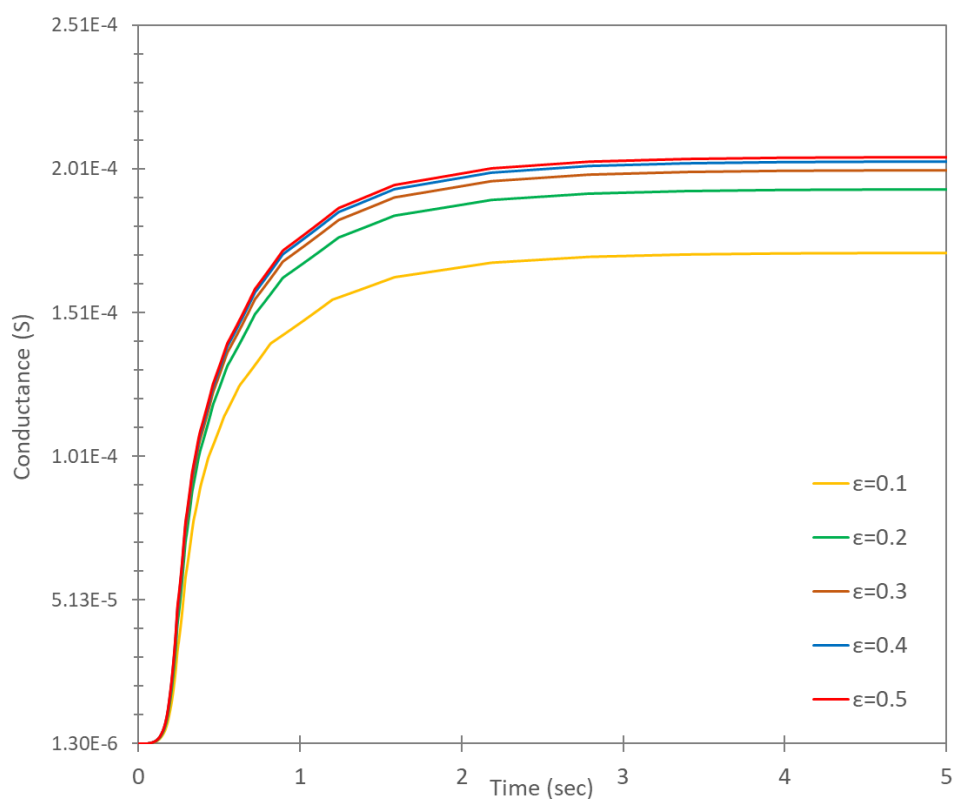


Figure 4-26. Surface averaged conductance change over time for different porosities of the sensing film in response to 200 ppm of CO at 600 K, with an inlet velocity of 0.01 m/s

Table 4-7. Porosity of the sensing film and corresponding sensor sensitivity

Porosity	Sensor Sensitivity (G-Gi)/Gi
0.1	131.6
0.2	148.7
0.3	153.8
0.4	156.1
0.5	157.3

The corresponding sensor sensitivity to the aforementioned porosities is represented in Table 4-7. Sensitivity is improved with increasing porosity. This is because the total volume of sensing material involved in the detection process becomes larger. However, the sensor sensitivity cannot be further improved significantly at higher porosities because the gas molecules can already reach and interact with most of the volume of the sensor. It is recommended that the porosity of the sensing film is kept as high as possible however structural integrity should be considered to ensure stable design.

## CHAPTER 5

### CONCLUSION

The final section of this study concludes the important findings from the whole chapters in the text. This study delved deep into the understanding of the sensing behavior of a SnO<sub>2</sub>-based metal oxide gas sensor in response to CO. In order to do so, a study on six different aspects was conducted.

First section covered the spatial distribution timewise comparison for CO and ionized oxygen density in the vertical direction. The findings reveal that the competing effect of reaction and diffusion determines the overall distribution inside the sensing film. In this part, the spatial distribution of CO concentration in the longitudinal direction change in time was also investigated. This profile was of particular interest due to the gradient introduced by the convective mass transfer. It revealed that the introduction of CO molecules, carried along the air flow caused the longitudinal gradient inside the film. This finding is then realized in the investigation of the Sherwood number profile, which had a peak at the air flow's initial contact with the sensor.

The second section investigated the effect of inlet concentration of CO on the conductance and sensitivity of the sensor. The timewise conductance profile showed that as CO inlet concentration increases, conductance increases. The sensitivity profile in relation to CO concentration exhibited a progressive increase, eventually reaching a plateau due to the saturation of reactive sites.

Following that, the third part examined the effect of inlet velocity on the timewise conductance profile of the sensor. The steady-state conductance is found to be the same for all inlet velocities. This result is attributed to low Peclet numbers, indicating a higher diffusion rate that facilitates gas access through the sensing film. Furthermore, two different flow configurations, that are vertical and horizontal, were

investigated for the same geometry. The conductance profile showed that the vertical flow configuration is significantly faster compared to the default configuration that is parallel to the sensing film because of the minimal viscous effects from the wall. The findings revealed that the response and recovery time become smaller as the fluid velocity increases due to the increased transport rate. In addition, higher recovery time compared to response time is a result of concentration gradient differences within the measurement chamber.

The fourth section covered the temperature effect on sensor response, sensitivity, and response/recovery dynamics. The results showed that the conductance increases as the temperature increases. However, the sensor sensitivity is the highest for 450 K, and it decreases asymptotically as the temperature approaches 800 K. This is explained by higher recovery of the ionized oxygen density at higher temperatures. In addition, CO spatial profile with respect to varying temperatures showed that higher temperature contributes more to the reaction rate than the diffusion rate, which limits the gas access through the sensing film.

The thickness effect on the spatial distribution of the CO and surface potential barrier, sensor response, and sensitivity were studied in the fifth section. The spatial distribution of CO along the vertical cutline in the sensing film showed that uniformity is the highest for the 50  $\mu\text{m}$  sensor that is thinnest. In addition, the surface potential spatial distribution revealed that the highest difference between the sensor surface and the deep of the sensor was observed for the thickest case, that is 150  $\mu\text{m}$ . This is a result of low gas access through the deeper regions of the sensor that leads to less ionized oxygen consumption at the deep for the thickest sensor. Furthermore, it is found that the sensitivity decreases as the thickness of the sensing film increases.

The final section covered the effect of the porosity of the sensing film. It examined the spatial ionized oxygen density along the cutline of the sensor and the sensor sensitivity. The results showed that as the porosity increases uniformity of ionized oxygen density increases. In addition, the sensor sensitivity increases asymptotically as the porosity increases.

For future work, a 3D model can be introduced to capture sensor behavior and improve accuracy. Moreover, humidity effects can be investigated to understand the performance of metal oxide gas sensors in real-world applications. In addition, by using this framework, different conditions can be worked on, and an optimum condition can be concluded for the use case scenario, which shows that this computational framework could make it faster to design such a sensor.



## REFERENCES

1. Neri, G. First fifty years of chemoresistive gas sensors. *Chemosensors* vol. 3 Preprint at <https://doi.org/10.3390/chemosensors3010001> (2015).
2. Mahajan, S. & Jagtap, S. Metal-oxide semiconductors for carbon monoxide (CO) gas sensing: A review. *Appl Mater Today* **18**, 100483 (2020).
3. Naz, S. *et al.* Solid state gas sensor. in *Materials Today: Proceedings* vol. 49 3245–3249 (Elsevier Ltd, 2020).
4. Dey, A. Semiconductor metal oxide gas sensors: A review. *Materials Science and Engineering: B* **229**, 206–217 (2018).
5. Mirzaei, A. *et al.* Resistive gas sensors based on metal-oxide nanowires. *J Appl Phys* **126**, 241102 (2019).
6. Capone, S. *et al.* Solid State Gas Sensors: State of the Art and Future Activities. *Cheminform* **35**, (2004).
7. Mahajan, S. & Jagtap, S. Metal-oxide semiconductors for carbon monoxide (CO) gas sensing: A review. 100483 (2019)  
doi:10.1016/j.apmt.2019.100483.
8. Nazemi, H., Joseph, A., Park, J. & Emadi, A. Advanced Micro- and Nano-Gas Sensor Technology: A Review. *Sensors* **19**, 1285 (2019).
9. Chai, H. *et al.* Stability of Metal Oxide Semiconductor Gas Sensors: A Review. *IEEE Sens J* **22**, 1 (2022).
10. Goel, N., Kunal, K., Kushwaha, A. & Kumar, M. Metal oxide semiconductors for gas sensing. *Engineering Reports* (2022)  
doi:10.1002/eng2.12604.
11. Varma, D., Mulay, S. & Chemtob, S. Carbon Monoxide: From Public Health Risk to Painless Killer. in *Handbook of Toxicology of Chemical Warfare Agents* 271–292 (2009). doi:10.1016/B978-0-12-374484-5.00020-1.

12. Korotcenkov, G. Metal Oxides for Solid-State Gas Sensors: What Determines Our Choice? *Materials Science and Engineering: B* **139**, 1–23 (2007).
13. Padvī, M., Moholkar, A., Prasad, S. & Prasad, N. A Critical Review on Design and Development of Gas Sensing Materials. *Engineered Science* (2021) doi:10.30919/es8d431.
14. Korotcenkov, G., Brinzari, V. & Ham, M. H. Materials Acceptable for Gas Sensor Design: Advantages and Limitations. *Key Eng Mater* **780**, 80–89 (2018).
15. Wetchakun, K. *et al.* Semiconducting metal oxides as sensors for environmentally hazardous gases. *Sens Actuators B Chem* **160**, 580–591 (2011).
16. Yuliarto, B., Gumilar, G. & Septiani, N. SnO<sub>2</sub> Nanostructure as Pollutant Gas Sensors: Synthesis, Sensing Performances, and Mechanism. *Advances in Materials Science and Engineering* **2015**, 1–14 (2015).
17. Velmathi, G., Mohan, S. & Henry, R. Analysis and review of tin oxide-based chemoresistive gas sensor. *IETE Technical Review (Institution of Electronics and Telecommunication Engineers, India)* **33**, 323–331 (2016).
18. Pamula, R., Kartik, A., Sai, S., Karnam, A. & Suja, K. *Design, Simulation and Optimization of Metal Oxide Sensor for Ammonia Detection Using Nanowires*. (2018). doi:10.1109/ICETIETR.2018.8529104.
19. Gurlo, A. & Riedel, R. In Situ and Operando Spectroscopy for Assessing Mechanisms of Gas Sensing. *Angew Chem Int Ed Engl* **46**, 3826–3848 (2007).
20. Sberveglieri, G., Hellmich, W. & Müller, G. Silicon hotplates for metal oxide gas sensor elements. *Microsystem Technologies* **3**, 183–190 (1997).

21. Rebordão, G., Palma, S. & Roque, A. Microfluidics in Gas Sensing and Artificial Olfaction. *Sensors* **20**, 5742 (2020).
22. Goel, N., Kunal, K., Kushwaha, A. & Kumar, M. Metal oxide semiconductors for gas sensing. *Engineering Reports* (2022) doi:10.1002/eng2.12604.
23. Grimes, C. A., Dickey, E. C. & Pishko, M. V. *Encyclopedia of Sensors*. (American Scientific Publishers, 2006).
24. Çiftyürek, E., Li, Z. & Schierbaum, K. *Adsorbed Oxygen Ions and Oxygen Vacancies; Their Concentration and Distribution in Metal Oxide Chemical Sensors and Influencing Role in Sensitivity and Sensing Mechanism*. (2022). doi:10.20944/preprints202212.0037.v1.
25. Tetenoire, A., Juaristi, J. & Alducin, M. *Insights into the Coadsorption and Reactivity of O and CO on Ru(0001) and Their Coverage Dependence*. (2021).
26. Lantto, V., Romppainen, P. & Leppävuori, S. A study of the temperature dependence of the barrier energy in porous tin dioxide. *Sensors and Actuators* **14**, 149–163 (1988).
27. Zhang, G. & Liu, M. Effect of Particle Size and Dopant on Properties of SnO<sub>2</sub>-Based Gas Sensors. *Sens Actuators B Chem* **69**, 144–152 (2000).
28. Bârsan, N., Huebner, M. & Weimar, U. Conduction mechanism in semiconducting metal oxide sensing films: impact on transduction. *Semiconductor Gas Sensors* 39–69 (2020) doi:10.1016/B978-0-08-102559-8.00002-1.
29. Malagù, C., Guidi, V., Stefancich, M., Carotta, M. & Martinelli, G. Model for Schottky barrier and surface states in nanostructured n-type semiconductors. *J Appl Phys* **91**, 808–814 (2002).

30. Gurlo, A. Interplay Between O<sub>2</sub> and SnO<sub>2</sub>: Oxygen Ionosorption and Spectroscopic Evidence for Adsorbed Oxygen. *Chemphyschem* **7**, 2041–2052 (2006).
31. Moumen, A., Kumarage, G. C. W. & Comini, E. P-Type Metal Oxide Semiconductor Thin Films: Synthesis and Chemical Sensor Applications. *Sensors* **22**, (2022).
32. Hu, C. *Modern Semiconductor Devices for Integrated Circuits*. (Prentice Hall, 2010).
33. Filipovic, L. & Selberherr, S. Thermo-electro-mechanical simulation of semiconductor metal oxide gas sensors. *Materials* **12**, (2019).
34. Graf, M., Gurlo, A., Bârsan, N., Weimar, U. & Hierlemann, A. Microfabricated gas sensor systems with sensitive nanocrystalline metal-oxide films. *Journal of Nanoparticle Research* **8**, 823–839 (2006).
35. Baxter, R. J. & Hu, P. Insight into why the Langmuir-Hinshelwood mechanism is generally preferred. *Journal of Chemical Physics* **116**, 4379–4381 (2002).
36. Yuan, C. *et al.* Modeling Interfacial Interaction between Gas Molecules and Semiconductor Metal Oxides: A New View Angle on Gas Sensing. *Advanced Science* **9**, (2022).
37. Vandenbroucke, A. Abatement of volatile organic compounds by combined use of non-thermal plasma and heterogeneous catalysis. (2015).
38. Gardner, J. W. A non-linear diffusion-reaction model of electrical conduction in semiconductor gas sensors. *Sens Actuators B Chem* **1**, 166–170 (1990).
39. Matsunaga, N., Sakai, G., Shimano, K. & Yamazoe, N. Diffusion equation-based study of thin film semiconductor gas sensor-response transient. *Sens Actuators B Chem* **83**, 216–221 (2002).

40. Urasinska-Wojcik, B., Vincent, T. A., Chowdhury, M. F. & Gardner, J. W. Ultrasensitive WO<sub>3</sub> gas sensors for NO<sub>2</sub> detection in air and low oxygen environment. *Sens Actuators B Chem* **239**, 1051–1059 (2017).
41. Ghosh, A., Maity, A., Banerjee, R. & Majumder, S. B. Volatile organic compound sensing using copper oxide thin films: Addressing the cross sensitivity issue. *J Alloys Compd* **692**, 108–118 (2017).
42. Maity, A. & Majumder, S. B. NO<sub>2</sub> sensing and selectivity characteristics of tungsten oxide thin films. *Sens Actuators B Chem* **206**, 423–429 (2015).
43. Lu, H., Ma, W., Gao, J. & Li, J. Diffusion-reaction theory for conductance response in metal oxide gas sensing thin films. *Sens Actuators B Chem* **66**, 228–231 (2000).
44. Fort, A. *et al.* CO sensing with SnO<sub>2</sub>-based thick film sensors: Surface state model for conductance responses during thermal-modulation. *Sens Actuators B Chem* **116**, 43–48 (2006).
45. Dadkhah, M. & Tulliani, J.-M. Nanostructured Metal Oxide Semiconductors towards Greenhouse Gas Detection. *Chemosensors* **10**, 57 (2022).
46. Umar, A. *Metal Oxide Nanostructures and Their Applications: Part-2*. (2010).
47. Yamazoe, N. New approaches for improving semiconductor gas sensors. *Sens Actuators B Chem* **5**, 7–19 (1991).
48. Chai, H. *et al.* Stability of Metal Oxide Semiconductor Gas Sensors: A Review. *IEEE Sens J* **22**, 1 (2022).
49. Wagner, T., Haffer, S., Weinberger, C., Klaus, D. & Tiemann, M. Mesoporous materials as gas sensors. *Chem Soc Rev* **42**, 4036–4053 (2013).

50. Vuong, D. D., Sakai, G., Shimano, K. & Yamazoe, N. Hydrogen sulfide gas sensing properties of thin films derived from SnO<sub>2</sub> sols different in grain size. *Sens Actuators B Chem* **105**, 437–442 (2005).
51. Korotcenkov, G. & Cho, B. K. Thin film SnO<sub>2</sub>-based gas sensors: Film thickness influence. *Sens Actuators B Chem* **142**, 321–330 (2009).
52. Sakai, G., Baik, N., Miura, N. & Yamazoe, N. Gas sensing properties of tin oxide thin films fabricated from hydrothermally treated nanoparticles: Dependence of CO and H<sub>2</sub> response on film thickness. *Sens Actuators B Chem* **77**, 116–121 (2001).
53. Jandow, N. N. *et al.* Thickness effect of ZnO/PPC gas sensor on the sensing properties of NO<sub>2</sub> gas. *AIP Conference Proceedings* vol. 2083 (2019).
54. Becker, T., Ahlers, S., Bosch-v.Braunmühl, C., Müller, G. & Kiesewetter, O. Gas Sensing Properties of Thin and Thick Film Tin Oxide Materials. *Sens Actuators B Chem* **77**, 55–61 (2001).
55. Saruhan, B., Lontio Fomekong, R. & Nahiriak, S. Review: Influences of Semiconductor Metal Oxide Properties on Gas Sensing Characteristics. *Frontiers in Sensors* **2**, (2021).
56. Wang, C., Yin, L., Zhang, L., Xiang, D. & Gao, R. Metal Oxide Gas Sensor: Sensitivity and Influencing Factors. *Sensors (Basel)* **10**, 2088–2106 (2010).
57. Chang, J. F., Kuo, H. H., Leu, I.-C. & Hon, M. H. The Effects of Thickness and Operation Temperature on ZnO:Al Thin Film CO gas Sensor. *Sens Actuators B Chem* **84**, 258–264 (2002).
58. Chollet, F. & Liu, H. *A (not so) short introduction to MEMS*. (2018).
59. Moon, S. E., Choi, N. J., Lee, H. K., Lee, J. & Yang, W. S. Semiconductor-type MEMS gas sensor for real-time environmental monitoring applications. *ETRI Journal* **35**, 617–624 (2013).

60. Fine, G., Cavanagh, L., Afonja, A. & Binions, R. Metal Oxide Semiconductor Gas Sensors in Environmental Monitoring. *Sensors (Basel)* **10**, 5469–5502 (2010).
61. Tyagi, H., Agarwal, A., Chakraborty, P. & Powar, S. *Applications of Solar Energy*. (2018). doi:10.1007/978-981-10-7206-2.
62. Shwetha, H. R., Sharath, S. M., Guruprasad, B. & Rudraswamy, S. B. MEMS based metal oxide semiconductor carbon dioxide gas sensor. *Micro and Nano Engineering* **16**, (2022).
63. Latino, M. & Neri, G. CHEMORESISTIVE METAL OXIDE GAS SENSOR: WORKING PRINCIPLES AND APPLICATIONS. **98**, 41 (2021).
64. Du, X. & George, S. M. Thickness dependence of sensor response for CO gas sensing by tin oxide films grown using atomic layer deposition. *Sens Actuators B Chem* **135**, 152–160 (2008).
65. Wang, C., Yin, L., Zhang, L., Xiang, D. & Gao, R. Metal oxide gas sensors: Sensitivity and influencing factors. *Sensors* vol. 10 2088–2106 Preprint at <https://doi.org/10.3390/s100302088> (2010).
66. Huang, J. & Wan, Q. Gas sensors based on semiconducting metal oxide one-dimensional nanostructures. *Sensors* vol. 9 9903–9924 Preprint at <https://doi.org/10.3390/s91209903> (2009).
67. Shooshtari, M., Salehi, A. & Vollebregt, S. Effect of temperature and humidity on the sensing performance of TiO<sub>2</sub>nanowire-based ethanol vapor sensors. *Nanotechnology* **32**, (2021).
68. Wang, T. *et al.* Highly sensitive and rapidly responding room-temperature NO<sub>2</sub> gas sensors based on WO<sub>3</sub> nanorods/sulfonated graphene nanocomposites. *Nano Res* **11**, 791–803 (2018).

69. Clifford, P. K. & Tuma, D. T. Characteristics of semiconductor gas sensors I. Steady state gas response. *Sensors and Actuators* **3**, 233–254 (1982).
70. Isaac, N. A., Pikaar, I. & Biskos, G. Metal oxide semiconducting nanomaterials for air quality gas sensors: operating principles, performance, and synthesis techniques. *Microchimica Acta* **189**, (2022).
71. Lin, T., Xin, Iv, Li, S. & Wang, Q. The Morphologies of the Semiconductor Oxides and Their Gas-Sensing Properties. *Sensors* **17**, 2779 (2017).
72. Rella, R. *et al.* CO sensing properties of SnO<sub>2</sub> thin films prepared by the sol-gel process. *Thin Solid Films* **304**, 339–343 (1997).
73. Lee, A. P. & Reedy, B. J. Temperature modulation in semiconductor gas sensing. *Sensors and Actuators B-chemical* **60**, 35–42 (1999).
74. Ciftyurek, E., Li, Z. & Schierbaum, K. Adsorbed Oxygen Ions and Oxygen Vacancies: Their Concentration and Distribution in Metal Oxide Chemical Sensors and Influencing Role in Sensitivity and Sensing Mechanisms. *Sensors* **23**, (2023).
75. Sedlák, P. & Kuberský, P. The effect of the orientation towards analyte flow on electrochemical sensor performance and current fluctuations. *Sensors (Switzerland)* **20**, (2020).
76. Kida, T., Kuroiwa, T., Yuasa, M., Shimano, K. & Yamazoe, N. Study on the response and recovery properties of semiconductor gas sensors using a high-speed gas-switching system. *Sens Actuators B Chem* **134**, 928–933 (2008).
77. Mohaghegh Montazeri, M., O'Brien, A. & Hoorfar, M. Understanding microfluidic-based gas detectors: A numerical model to investigate fundamental sensor operation, influencing phenomena and optimum geometries. *Sens Actuators B Chem* **300**, (2019).

78. Kaaliveetil, S. *et al.* Microfluidic Gas Sensors: Detection Principle and Applications. *Micromachines (Basel)* **13**, (2022).
79. White, F. M. *Fluid Mechanics*. (WCB/McGraw-Hill, 1999).
80. Haynes, W. M., Lide, D. R. & Bruno, T. J. *CRC Handbook of Chemistry and Physics 97 th Edition*.
81. Tiemann, M. Porous Metal Oxides as Gas Sensors. *Chemistry – A European Journal* **13**, 8376–8388 (2007).
82. Pisani, L. Simple Expression for the Tortuosity of Porous Media. *Transp Porous Media* **88**, 193–203 (2011).
83. Kawagoe, Y. *et al.* A study on pressure-driven gas transport in porous media: from nanoscale to microscale. *Microfluid Nanofluidics* **20**, (2016).
84. Madou, M. J. & Morrison, S. R. (Stanley R. *Chemical sensing with solid state devices*. (Academic Press, 1989).
85. Versteeg, H. K. & Malalasekera, W. *An Introduction to Computational Fluid Dynamics: The Finite Volume Method*. (Pearson Education Limited, 2007).
86. Sagadevan, S. & Podder, J. Optical and Electrical Properties of Nanocrystalline SnO<sub>2</sub> Thin Films Synthesized by Chemical Bath Deposition Method. *Soft Nanoscience Letters* **05**, 55–64 (2015).
87. Brynzari, V., Korotchenkov, G. & Dmitriev, S. Simulation of thin film gas sensors kinetics. *Sens Actuators B Chem* **61**, 143–153 (1999).
88. McAleer, J. F., Moseley, P. T., Norris, J. O. W. & Williams, D. E. Tin dioxide gas sensors. Part 1. - Aspects of the surface chemistry revealed by electrical conductance variations. *Journal of the Chemical Society, Faraday Transactions 1: Physical Chemistry in Condensed Phases* **83**, 1323–1346 (1987).

89. Han, M. A., Kim, H. J., Lee, H. C., Park, J. S. & Lee, H. N. Effects of porosity and particle size on the gas sensing properties of SnO<sub>2</sub> films. *Appl Surf Sci* **481**, 133–137 (2019).
90. Yuan, Z., Zhang, S., Meng, F., Zhang, H. & Zuo, K. Investigation of Grain Radius Dependence of Sensitivity for Porous Thin Film Semiconducting Metal Oxide Gas Sensor. *IEEE Sens J* **20**, 4275–4282 (2020).
91. Ionescu, R. *et al.* Response model for thermally modulated tin oxide-based microhotplate gas sensors. *Sens Actuators B Chem* **95**, 203–211 (2003).
92. Mirkelamoglu, B. & Karakas, G. CO oxidation over palladium- And sodium-promoted tin dioxide: Catalyst characterization and temperature-programmed studies. *Appl Catal A Gen* **281**, 275–284 (2005).
93. Bezzerrouk, M. A. *et al.* Thermodynamic, structural and electronic, properties of SnO<sub>2</sub>: By GGA and GGA + trans-blaha-modified Becke–Johnson (TB-mBJ) calculation. *Superlattices Microstruct* **84**, 80–90 (2015).
94. Figaro Inc. *TGS 2442-for the detection of Carbon Monoxide*. (2013).
95. Mirzaei, A. *et al.* Resistive gas sensors based on metal-oxide nanowires. *J Appl Phys* **126**, 241102 (2019).
96. Ravindra, N. M. & Srivastava, V. K. Temperature dependence of the energy gap in semiconductors. *Journal of Physics and Chemistry of Solids* **40**, 791–793 (1979).

## APPENDICES

### A. Initial Ionized Oxygen Density Calculation

Initial ionized oxygen density is calculated by considering the steady-state condition of the differential equation without the consumption term that corresponds to the oxidation reaction because of CO absence within the sensing film.

```
%Sensor parameters
A1=-3.374*10^-30;B1=9.5*10^20;C1=0.0873;D1=81.45;
R=8.314;
E1=31427.7;E2=4637.3;E3=5121.42;E12=58535.35;
T=600;
NS_steady_init=zeros(size(T));

for i=1:size(T,2)
syms NS

%Steady state function
func = exp((A1*NS^2)/T(i))*(B1*exp(-E1/(R*T(i)))+C1*exp(-E2/(R*T(i)))*NS)/
      (D1*exp(-E12/(R*T(i)))+exp((A1*NS^2)/T(i)))-C1*exp(-E2/(R*T(i)))*NS;
%Initial steady state value
NS_steady_init(i)= double(solve(func,NS));

end
```

### B. Temperature Change Calculation

The calculation of mass of the SnO<sub>2</sub> is given below.

$$\rho V_{total}(1 - \varepsilon) = m_{solid}$$

$$6950 \text{ kg/m}^3 \times 5 \times 10^{-10} \times (1 - 0.2) = 4 \times 10^{-10} \text{ kg}$$

$$m_{solid}c_p = C_{SnO_2}$$

$$4 \times 10^{-10} \text{ kg} \times \frac{48.7 \frac{\text{J}}{\text{mol}} \cdot \text{K}}{0.15 \text{ kg/mol}} = 9.02 \times 10^{-4} \text{ J/K}$$

The calculation of dissipated heat is given below.

$$P = \frac{V^2}{R} = V^2 \times G$$

Total dissipated heat can be calculated by utilizing the conductance and time relation.

$$Q = \int_0^3 V^2 G dt$$

Using Trapezoidal rule this integral can be calculated (in MATLAB “trapz(t,G\*V<sup>2</sup>)”).  $Q$  is found as 0.003 Joule.

$$Q = C_{SnO_2} \Delta T$$

hence  $\Delta T$  is found as 3.3 Kelvin.

### C. Initial Surface Potential Barrier Calculation

$$V_s = \frac{q \cdot N_s^2}{2 \epsilon_0 \epsilon_r N_d}$$

Initial surface potential barrier is calculated by considering the initial value of the ionized oxygen molecules at the operating temperature.

For 600 K, initial ionized oxygen density is  $5.03 \times 10^{16} \text{ 1/m}^2$ . By replacing the model parameters  $V_s$  initial value is found as 0.74 for the sensor operating at 600 Kelvin.